

©2018

Veerakiet Boonkanokwong

ALL RIGHTS RESERVED

DYNAMICS AND SCALE-UP OF COHESIONLESS AND COHESIVE GRANULAR
FLOWS IN A BLADED MIXER

By

VEERAKIET BOONKANOKWONG

A dissertation submitted to the

School of Graduate Studies

Rutgers, The State University of New Jersey

In partial fulfillment of the requirements

For the degree of

Doctor of Philosophy

Graduate Program in Chemical and Biochemical Engineering

Written under the direction of

Benjamin J. Glasser

And approved by

New Brunswick, New Jersey

MAY, 2018

ABSTRACT OF THE DISSERTATION

Dynamics and scale-up of cohesionless and cohesive granular flows in a bladed mixer

By VEERAKIET BOONKANOKWONG

Dissertation Director:

Benjamin J. Glasser

Manufacture of commercial products such as chemicals, cosmetics, foods, and pharmaceutical solid dosage forms often involves particle processing. Compared to fluid processing, our fundamental understanding of solids processing lags behind, and therefore problems such as attrition, segregation, and agglomeration still occur during these processing steps. Moreover, the roles of material properties, equipment configurations, and process parameters on the flow behaviors of particulate systems remain unclear. In this dissertation, cohesionless (dry) and cohesive (wet) granular flows in a bladed mixer were studied using both computational and experimental techniques to obtain better understanding of the flow behaviors and mixing performance. First, the effect of the number of impeller blades used in an agitated mixer was examined via discrete element method (DEM) numerical simulations varying from one to four blades. It was found that granular temperature, particle diffusivity, and mixing rate in the 2- and 3-bladed mixers were larger than those in the 1- and 4-bladed cases. This resulted from a larger magnitude of the tangential component of the blade-particle contact forces and a great extent of dilation of the granular bed in the 2- and 3-bladed mixers. Next, scale-up

of cohesionless and cohesive granular systems to a larger, industrially relevant scale was accomplished in the DEM simulations. Scaling-up systems composed of cohesionless monodisperse spherical particles in 2- and 4-bladed mixers when increasing the mixer diameter to particle diameter (D/d) ratio from 63 to 90 revealed that changing the system size had insignificant impact on the granular flow behaviors and mixing kinetics. Scale-up of non-cohesive granular systems based on the number of impeller blades (2 and 4 blades) used in the agitated mixer could be scaled by the diameter of the mixer and the rotational speed of the impeller blades within the range from $D/d = 63$ to 90. Although there was an impact of cohesion that caused some differences between system sizes, it was found that wet granular flows in bladed mixers could be scaled by the diameter of the mixer and the tip speed of the impeller blades within the range of D/d ratio from 75 to 100. Additionally, experimental measurements of the agitation torque exerted on a particle bed and the power draw for the motor driving the impeller blades in a mixing process were conducted to investigate the impact of particle properties and blade geometry as a function of the blade rotation rate. It was found that the torque exerted on a granular bed and the power consumption were a strong function of the impeller blade configuration, the position of the blades in a deep granular bed, the fill height of the glass beads, and the size and friction coefficient of the particles. It was observed that the time-averaged torque and power consumption for different particle sizes qualitatively scaled with particle diameter. A scale-up relationship for a deep granular bed was developed: the time-averaged torque and average adjusted power consumption scaled with the square of the material fill height.

Acknowledgement

During the course of conducting this research in a doctorate program, I have greatly received advantages from guidance, advice, assistance, and encouragement from a number of individuals. I begin by thanking my dissertation advisor, Professor Benjamin J. Glasser, for his helpful suggestions and advice regarding the direction and execution of this research work. I express special gratitude for his knowledge and technical insight, for his thorough review of my manuscripts, and for all of his guidance, support, and mentoring throughout the course of study when I was master's and doctoral student at Rutgers University.

I acknowledge my colleagues, namely, Dr. Yangyang Shen for all her help, Hao Chen who is a really great fellow and shares a very good friendship with me, Ingrid Paredes – the first person who taught me to use EDEM™ software, and all other people in Prof. Glasser's Particle Technology Research Group and in the Engineering Research Center for Structured Organic Particulate Systems (C-SOPS) at the Chemical and Biochemical Engineering (CBE) department of Rutgers University. I particularly thank Rohan P. Frank and Pavithra Valliappan for their friendship and assistance when they were master's degree students working with me in this research project. I thank Phiraphat Wichitsopha for helping me with organizing the format of this dissertation. I exclusively thank Prin Chaksmithanont for his dedication and contribution to this project, and I really appreciate his technical assistance when I encountered computer issues.

I thank our collaborators, Benedict J. S. Benque and Prof. Johannes G. Khinast from Graz University of Technology, Austria, for many helpful collaborations and discussions of research work. I thank the committee members for my dissertation defense examination – Prof. Yee C. Chiew, Dr. Nina C. Shapley, and Dr. Brenda Remy – for their time and availability and for giving me back useful feedbacks and suggestions. I would like to express my gratitude toward Dr. Brenda Remy in particular as she laid a strong foundation for particle dynamics research in our group, making it straightforward to continue from her previous work. I also thank her technical insight regarding the discrete element method modeling and the torque and power measurement experimentation. I wish to thank EDEM™, Yokogawa™, and Chemglass Life Sciences® representatives, and all Rutgers staffs for their technical supports to this research project.

I would like to gratefully thank Chulalongkorn University, Bangkok, Thailand for granting me a financial support (100th-year Celebration of Chulalongkorn University Academic Scholarship) during my educational leave of absence which allowed me to pursue master's and doctoral degrees and enabled the completion of this research. I also thank the Department of Pharmaceutics and Industrial Pharmacy, Faculty of Pharmaceutical Sciences, Chulalongkorn University for giving me a very challenging opportunity to explore a chemical and biochemical engineering world. I would like to express my gratitude to Prof. Garmpimol C. Ritthidej who is an excellent teacher and role model for my career path and always supports me since I was her student and apprentice.

Last but not least, I ultimately thank my family – my parents, sister, and niece – for their love, support, assistance, and encouragement. Thank you for raising and nurturing me and teaching me how to be a good man. Without them, I would not have succeeded so far up to this point. I particularly want to thank Thai students at Rutgers University and all Thai fellows in New Jersey and in the U.S. for their friendship and encouragement and for making my life in a graduate school and in the United States a very enjoyable experience and fun times. I would like to thank all good people and friends who have passed into my life and taught me how to be a good human and how to treat them well in return. I personally express my gratitude toward Seven Something: 42.195 and Project S: SPIKE!, Side by Side, and Shoot! for their inspirations and encouragements when I felt hopeless. Once again, I would like to specially thank PC for his love, support, morale, enthusiasm, and lifelong friendship, and for making my last semester here at Rutgers a wonderful moment. I would not have been able to accomplish this without you by my side. I would not have achieved this without all people I mentioned above.

Table of Contents

ABSTRACT OF THE DISSERTATION	ii
Acknowledgement	iv
Table of Contents	vii
List of Illustrations	xi
List of Tables	xix
Chapter 1. Introduction	1
1.1 Motivation and Significance	1
1.2 Granular Flow Regimes	4
1.3 Mixing Processes of Granular Materials	6
1.4 Impeller Torque and Power Consumption	10
1.5 Cohesive Granular Flows	13
1.6 Unanswered Questions	14
1.7 Figure for Chapter 1	16
Chapter 2. Numerical and Experimental Methods	18
2.1 Numerical Simulations	18
2.1.1 Theoretical Basis	18
2.1.2 Contact Force Model	19
2.1.3 Cohesive Force Model	21
2.1.4 Mixer Geometry and Input Parameters	24
2.1.5 Macroscopic Flow Properties	26
2.1.5.1 Granular Temperature	27

2.1.5.2 Particle Diffusivities and Péclet Number.....	28
2.1.5.3 Bulk Density, Solids Fraction, and Void Fraction.....	29
2.1.5.4 Collisional Stresses and Pressure.....	30
2.1.5.5 Relative Standard Deviation	31
2.1.5.6 Lacey Index.....	32
2.2 Experimental Method	33
2.2.1 Experimental Set-up.....	33
2.2.2 Materials Used in Experiments	34
2.2.3 Impeller Torque and Power Measurements	35
2.2.4 Particle Surface Roughness Modification.....	38
2.2.5 Water Addition for Cohesive Granular Systems.....	39
2.3 Figures for Chapter 2	41
2.4 Tables for Chapter 2	43
Chapter 3. Effect of the Number of Impeller Blades on Granular Flow in a Bladed Mixer	46
3.1 Velocity Fields and Velocity Frequency Distributions.....	47
3.2 Blade-Particle Contact Forces and Force Frequency Distributions.....	49
3.3 Normal Contact Force Network.....	51
3.4 Mixing Kinetics	53
3.5 Granular Temperature.....	54
3.6 Particle Diffusivities	55
3.7 Bulk Density, Solids Fraction, and Void Fraction.....	56
3.8 Conclusions for Chapter 3	60

3.9 Figures for Chapter 3	63
3.10 Table for Chapter 3	77
Chapter 4. Effect of Particle Properties and Process Parameters on Impeller Torque and Power Consumption: Experimental Investigations.....	78
4.1 Granular Flow in a Shallow Bed.....	78
4.1.1 Torque and Power Measurements.....	79
4.1.2 Fluctuation Analysis of Torque Data	81
4.1.3 Fast Fourier Transform (FFT) of Torque Data	82
4.2 Effect of Impeller Blade Configurations	83
4.2.1 Effect of the Number of Impeller Blades.....	83
4.2.2 Effect of the Impeller Blade Angle	84
4.2.3 Effect of the Impeller Blade Length	85
4.3 Effect of Particle Friction Coefficient	86
4.4 Effect of Impeller Blade Position in a Deep Granular Bed	87
4.5 Effect of Particle Size and Scaling Relationship	89
4.6 Effect of Material Fill Height and Scale-up.....	91
4.7 Effect of Moisture Content	95
4.8 Conclusions for Chapter 4	96
4.9 Figures for Chapter 4	100
Chapter 5. Scale-up of Cohesionless and Cohesive Granular Systems	114
5.1 Scale-up of Cohesionless Granular Systems: Effect of the Number of Blades	114
5.1.1 Normalized Velocity Fields	114
5.1.2 Mixing Kinetics	115

5.1.3 Granular Temperature	115
5.1.4 Particle Diffusivities	116
5.1.5 Void Fraction	117
5.2 Scale-up of Cohesive Granular Systems.....	117
5.2.1 Normalized Tangential Velocity Profiles	120
5.2.2 Mixing Patterns	123
5.2.3 Mixing Kinetics	124
5.2.4 Particle Diffusivities	126
5.3 Conclusions for Chapter 5	128
5.4 Figures for Chapter 5	130
5.5 Tables for Chapter 5	142
Chapter 6. Conclusions and Future Work.....	144
Appendix.....	149
Notations	151
List of Variables:	151
List of Subscripts:	154
List of Greek Letters:	154

List of Illustrations

Fig. 1.1. A schematic diagram of particulate flow map as a function of the dimensionless shear rate representing the quasi-static, intermediate, and rapid flow regimes (from Tardos et al. [33]).....	16
Fig. 1.2. Different states of cohesive granular materials depending on the level of moisture content in the system (adapted from am Ende et al. [73]).	17
Fig. 2.1. A schematic of a capillary bridge between two particles (from Remy [93]).	41
Fig. 2.2. A schematic of the 4-bladed mixer used in the DEM simulations and the experiments. Dimensions of the unit are shown in Tables 2.1, 2.4, and 2.6.....	41
Fig. 2.3. A schematic of the laboratory experimental set-up for the impeller torque and power measurements.....	42
Fig. 3.1. Schematics of the four different impeller blade configurations: (a) 1 blade, (b) 2 blades, (c) 3 blades, and (d) 4 blades.	63
Fig. 3.2. Time-averaged radial (V_r) and vertical (V_y) velocity fields in a vertical plane in front of the blade for different numbers of blades: (a) 1 blade, (b) 2 blades, (c) 3 blades, and (d) 4 blades. The color bar indicates magnitude of the tangential velocity (V_t). The schematic at the top of the figure shows the position of the vertical plane for the 4-blade configuration. Analogous vertical planes are used for the other cases. ...	64
Fig. 3.3. Normalized velocity frequency distributions for the tangential (V_t^*), radial (V_r), and vertical (V_y) velocity components for different numbers of blades: (a)–(c) 1 blade, (d)–(f) 2 blades, (g)–(i) 3 blades, and (j)–(l) 4 blades. The velocity values shown here are relative to the tip speed of the blades.	65

Fig. 3.4. Time-averaged vector fields of the radial (F_r) and vertical (F_y) components of the blade-particle contact forces in a vertical plane in front of the blade for different numbers of blades: (a) 1 blade, (b) 2 blades, (c) 3 blades, and (d) 4 blades. The color bar indicates magnitude of the tangential component of the contact force (F_t). The schematic at the top of the figure shows the position of the vertical plane for the 4-blade configuration. Analogous vertical planes are used for the other cases.	66
Fig. 3.5. Frequency distributions for the tangential (F_t), radial (F_r), and vertical (F_y) components of the blade-particle contact forces for different numbers of blades: (a)–(c) 1 blade, (d)–(f) 2 blades, (g)–(i) 3 blades, and (j)–(l) 4 blades.	67
Fig. 3.6. Effect of the number of blades on the normal contact force network near top of the blades. (a) 1 blade, (b) 2 blades, (c) 3 blades, and (d) 4 blades.	68
Fig. 3.7. Top view snapshots of the mixing process for the left-right segregated system at 20 RPM for different numbers of blades: (a) 1 blade, (b) 2 blades, (c) 3 blades, and (d) 4 blades.	69
Fig. 3.8. Effect of the number of blades on mixing performance at 20 RPM. Relative standard deviation (RSD) of the red particle concentrations vs. number of revolutions of the blades.	70
Fig. 3.9. Effect of the number of blades on degree of mixing at 20 RPM. Lacey index (M) of the red particle concentrations vs. number of revolutions of the blades.	71
Fig. 3.10. Effect of the number of blades on time-averaged granular temperature as a function of the radial position.	72
Fig. 3.11. Effect of the number of blades on (a) void fractions, ε and (b) magnitude of the blade-particle contact forces vs. dimensionless radial position (r/R) in a mixer. Both	

quantities were calculated by time-averaging using spherical sampling bins at a height $H = 0.1$ m.	73
Fig. 3.12. Solids fraction (ϕ) vs. number of blade revolutions at the position $r/R = 0.5$ and $H = 0.1$ m for different numbers of blades: (a) 1 blade, (b) 2 blades, (c) 3 blades, and (d) 4 blades.....	74
Fig. 3.13. Solids fraction (ϕ) vs. number of blade revolutions and heights at the position $r/R = 0.5$ for different numbers of blades: (a) 1 blade, (b) 2 blades, (c) 3 blades, and (d) 4 blades.....	75
Fig. 3.14. Power spectrum of solids fraction (ϕ) at the position $r/R = 0.5$ for different numbers of blades: (a) 1 blade, (b) 2 blades, (c) 3 blades, and (d) 4 blades.....	76
Fig. 4.1. Granular flow properties as a function of the dimensionless shear rate ($\dot{\gamma}^*$) for “the standard case”: (a) the time-averaged impeller torque and (b) the average adjusted power (P^*). The experiments were performed using red glass beads of 2-mm diameter loaded to a 30-mm fill height (shallow bed, $H/D = 0.30$) and the standard impeller blades (4 blades with a 135° angle and 45-mm length).....	100
Fig. 4.2. Normalized torque (T^*) fluctuation profiles at steady state for different blade rotational speeds: (a) 10 RPM, (b) 20 RPM, (c) 60 RPM, and (d) 200 RPM. The normalized torque values shown in this figure are the instantaneous torques divided by the time-averaged torque at each shear rate. Torque signal measurements were recorded every 0.125 seconds.	101
Fig. 4.3. Single-sided amplitude spectrums of the fast Fourier transform (FFT) torque signals for different blade rotational speeds: (a) 10 RPM, (b) 20 RPM, (c) 60 RPM, and (d) 200 RPM. Torque signal measurements were recorded every 0.125 s.	102

Fig. 4.4. Impeller blade configurations used in the experiments: (a) standard impeller, 4 blades, 45-mm length, 135° angle; (b) 2 blades, 45-mm length, 135° angle; (c) 1 blade, 45-mm length, 135° angle; (d) 4 blades, 45-mm length, 90° angle; (e) 4 blades, 45-mm length, 150° angle; and (f) 4 blades, 37.5-mm length, 135° angle. The black squares in this figure show an area of $1 \times 1 \text{ cm}^2$	103
Fig. 4.5. Effect of the number of impeller blades on: (a) the average torque and (b) the average adjusted power as a function of the dimensionless shear rate. Impeller blades used in these sets of experiments have 135° angle and 45-mm length.	104
Fig. 4.6. Effect of the impeller blade angle on: (a) the average torque and (b) the average adjusted power as a function of the dimensionless shear rate. Impeller blades used in these sets of experiments have 4 blades and 45-mm length.	105
Fig. 4.7. Effect of the impeller blade length on: (a) the average torque and (b) the average adjusted power as a function of the dimensionless shear rate. Impeller blades used in these sets of experiments for both cases have 4 blades and 135° angle.	106
Fig. 4.8. Effect of the macroscopic friction coefficient (μ) of particles on: (a) the average torque and (b) the average adjusted power as a function of the dimensionless shear rate. Experiments were performed using the standard impeller blades and the glass beads with a diameter of 2 mm loaded to a 30-mm fill height ($H/D = 0.30$).	107
Fig. 4.9. Effect of the impeller blade position in a deep granular bed (90-mm fill height) on: (a) the time-averaged torque and (b) the average adjusted power as a function of the dimensionless shear rate, compared to those values in a shallow bed (30-mm fill height just covering the top tip of the blades). Blade position in a deep bed: top (H/D	

= 0.30), middle ($H/D = 0.60$), and bottom ($H/D = 0.90$). Experiments were performed using the standard impeller blades and the glass beads with a diameter of 2 mm....	108
Fig. 4.10. Effect of the particle size on: (a) the average torque and (b) the average adjusted power drawn from experiments as a function of the shear rate $\dot{\gamma}$. Experiments were performed using the standard impeller blades, and the granular bed was filled up to a 30-mm height ($H/D = 0.30$) for all particle sizes.	109
Fig. 4.11. (a) The time-averaged normalized torque, T/d , and (b) the average normalized adjusted power, P^*/d , plotted as a function of the shear rate $\dot{\gamma}$. Experiments were performed using the standard impeller blades, and the granular bed was filled up to a 30-mm height ($H/D = 0.30$) for all particle sizes. Note that the y-axis in Fig. 4.11b is multiplied by a factor of 10^3	110
Fig. 4.12. Effect of the amount of materials in a bladed mixer, reported as the H/D ratio, on: (a) the time-averaged torque and (b) the average adjusted power as a function of the dimensionless shear rate. Experiments were performed using the standard impeller blades and the glass beads with a diameter of 5 mm. The effective H/D ratios indicate usage of a lead weight instead of using actual particle mass.	111
Fig. 4.13. (a) The time-averaged torque T and (b) the average adjusted power P^* values in Fig. 4.12 were normalized by square of the height (H^2) of the granular material filled in a bladed mixer plotted as a function of the dimensionless shear rate. Experiments were performed using the standard impeller blades and the glass beads with a diameter of 5 mm. The effective H/D ratios indicate usage of a lead weight instead of using actual particle mass. Note that the y-axis in Fig. 4.13b is multiplied by a factor of 10^3	112

Fig. 4.14. Effect of the moisture content in granular systems on: (a) the average torque and (b) the average adjusted power as a function of the dimensionless shear rate. Experiments were performed using the standard impeller blades and the glass beads with a diameter of 2 mm loaded to a 30-mm fill height ($H/D = 0.30$).	113
Fig. 5.1. Normalized time-averaged radial (V_r) and vertical (V_y) velocity fields in a vertical plane in front of the blade for different numbers of blades and D/d ratios: (a) 2 blades at $D/d = 63$, (b) 2 blades at $D/d = 90$, (c) 4 blades at $D/d = 63$, and (d) 4 blades at $D/d = 90$. The color bar indicates magnitude of the tangential velocity (V_t). Particle velocities are normalized relative to the tip speed of the blades (V_{tip}) for both D/d ratios. The schematic at the top of the figure shows the position of the vertical plane for the 4-blade configuration. An analogous vertical plane is used for the 2-bladed cases.	130
Fig. 5.2. Effect of different numbers of blades and D/d ratios on degree of mixing at 20 RPM. Lacey index (M) of the red particle concentrations vs. number of revolutions of the blades.	131
Fig. 5.3. Effect of different numbers of blades and D/d ratios on time-averaged granular temperature as a function of the radial position.	131
Fig. 5.4. Effect of different numbers of blades and D/d ratios on void fraction (ϵ) in front of the blade as a function of dimensionless radial position (r/R) in a mixer.	132
Fig. 5.5. Effect of D/d ratios and moisture content (ϕ_{liq}) on normalized tangential velocity (V_t/V_{tip}) profiles as a function of the number of revolutions of the impeller blade in cohesive granular systems: (a) $D/d = 50$, (b) $D/d = 75$, and (c) $D/d = 100$. Instantaneous tangential velocities (V_t) of particles at each time-step are normalized	

relative to the tip speed of the blades (V_{tip}) for all D/d ratios. Liquid volume fraction (ϕ_{liq}) in granular systems is examined at three levels: $\phi_{liq} = 0$ (dry), 0.01, and 0.045.	132
Fig. 5.6. Effect of D/d ratios on top-view snapshots of particles in cohesionless granular systems ($\phi_{liq} = 0$) showing mixing patterns as a function of the number of revolutions of the impeller blade at $V_{tip} = 0.589$ m/s.	133
Fig. 5.7. Effect of D/d ratios on top-view snapshots of particles in cohesive granular systems (at $\phi_{liq} = 0.01$) showing mixing patterns as a function of the number of revolutions of the impeller blade at $V_{tip} = 0.589$ m/s.	134
Fig. 5.8. Effect of D/d ratios on top-view snapshots of particles in cohesive granular systems (at $\phi_{liq} = 0.045$) showing mixing patterns as a function of the number of revolutions of the impeller blade at $V_{tip} = 0.589$ m/s.	135
Fig. 5.9. Effect of D/d ratio on mixing kinetics in cohesionless granular systems ($\phi_{liq} = 0$) for $V_{tip} = 0.589$ m/s: relative standard deviation (RSD) of the blue particle concentration vs. the number of revolutions of the impeller blade.	136
Fig. 5.10. Effect of D/d ratio on mixing kinetics in cohesive granular systems (at $\phi_{liq} = 0.01$) for $V_{tip} = 0.589$ m/s: relative standard deviation (RSD) of the blue particle concentration vs. the number of revolutions of the impeller blade.	137
Fig. 5.11. Effect of D/d ratio on mixing kinetics in cohesive granular systems (at $\phi_{liq} = 0.045$) for $V_{tip} = 0.589$ m/s: relative standard deviation (RSD) of the blue particle concentration vs. the number of revolutions of the impeller blade.	138
Fig. 5.12. Effect of D/d ratio on mixing performance in cohesionless granular systems ($\phi_{liq} = 0$) for $V_{tip} = 0.589$ m/s: relative standard deviation (RSD) of the blue particle	

concentration vs. dimensionless radial positions (r/R) after 15 revolutions of the impeller blade.....	139
Fig. 5.13. Effect of D/d ratio on mixing performance in cohesive granular systems (at ϕ_{liq} = 0.01) for $V_{tip} = 0.589$ m/s: relative standard deviation (RSD) of the blue particle concentration vs. dimensionless radial positions (r/R) after 15 revolutions of the impeller blade.....	
	140
Fig. 5.14. Effect of D/d ratio on mixing performance in cohesive granular systems (at ϕ_{liq} = 0.045) for $V_{tip} = 0.589$ m/s: relative standard deviation (RSD) of the blue particle concentration vs. dimensionless radial positions (r/R) after 15 revolutions of the impeller blade.....	
	141
Fig. A1. Comparisons between DEM computational results and PIV experimental data for normalized velocity fluctuations near top free surface at $r/R = 0.5$ and by the cylinder walls at $y/H = 0.5$. All results shown are for a blade rotational speed of 50 RPM. (a) and (b): top free surface normalized tangential velocity (V_t/V_{tip}); (c) and (d): cylinder wall normalized tangential velocity (V_t/V_{tip}); (e) and (f): top free surface normalized radial velocity (V_r/V_{tip}); and (g) and (h): cylinder wall normalized vertical velocity (V_y/V_{tip}).	
	150

List of Tables

Table 2.1. Mixer dimensions for the base cases.	43
Table 2.2. Input parameters in EDEM™ simulations.....	43
Table 2.3. Cohesive force model input parameters in EDEM™ simulations.....	44
Table 2.4. Dimensions of a laboratory mixer.	44
Table 2.5. Glass bead properties used in experiments.....	45
Table 2.6. Dimensions of a mixer ($D/d = 50$) used in Section 5.2 of Chapter 5.	45
Table 3.1. Effect of the number of blades on normalized particle diffusivity (D_{ij}^*) and Péclet number (Pe_{ij}). Particle diffusivities were computed with a Δt of $1/4$ of a revolution and were averaged over all the particles in the computational domain.....	77
Table 5.1. Effect of different numbers of blades and D/d ratio on normalized particle diffusivity (D_{ij}^*) and Péclet number (Pe_{ij}) in cohesionless granular systems. Particle diffusivities were computed with a Δt of $1/4$ of a revolution and were averaged over all the particles in the computational domain.	142
Table 5.2. Effect of D/d ratio and moisture content (ϕ_{liq}) on normalized particle diffusivities (D_{ij}^*) and Péclet number (Pe_{ij}) in cohesionless ($\phi_{liq} = 0$) and cohesive ($\phi_{liq} = 0.01$ and 0.045) granular systems. Particle diffusivities were computed with a Δt of $1/4$ of a revolution and were averaged over all the particles in the computational domain.....	143

Chapter 1. Introduction

1.1 Motivation and Significance

Powders and granular materials occur in everyday life in situations ranging from baking to geophysical flows to industrial processes [1, 2]. A large number of industries including catalytic, chemical, cosmetic, food, and pharmaceutical industries frequently handle powders or granular materials [3]. Compared to fluid processing, our understanding of solids processing lags behind. The lack of fundamental understanding of granular systems can lead to inefficient process development and design, poor identification of critical process parameters, and scale-up problems [4]. A cylindrical mixer mechanically agitated by an impeller blade, also known as a bladed mixer, is a common geometry in a variety of particle processing technologies. Bladed mixers are used in a number of solids processing operations including blending, agitated drying, high-shear granulation, and during the tablet compaction unit operation to encourage flow in the feed-frame assembly [5, 6]. While there has been a significant amount of research on granular flow in bladed mixers, our understanding of bladed mixer operations is still incomplete. Problems such as segregation [7], particle attrition [8-12], and agglomeration [13, 14] are known to occur in this geometry during processing, but the role of particle properties, equipment configurations, and operating parameters on the flow behaviors and mixing kinetics remains unclear. Only little have the effects of these factors on solids flow and mixing in a bladed mixer been studied in detail.

Previous researchers have experimentally investigated solids flow in a bladed mixer. Measurements of power and torque were carried out in order to understand the force needed to move the blades through a bed of particles [15, 16]. Positron emission particle tracking was used to investigate the movement of particles in a bladed mixer [17]. Particle image velocimetry (PIV) was carried out at the free surface and walls of a cylindrical mixer in order to characterize flow behavior [18, 19]. These studies found that a periodic three-dimensional (3D) recirculation pattern developed with a frequency corresponding to that of the blade rotation speed. It was also observed that the size of the recirculation zones and the rate of mixing were significantly influenced by the fill level. Additionally, velocity profiles were found to scale linearly with the rotational speed of the blades. Although these experimental studies have provided insight into the granular behavior in bladed mixers, they have been limited to the effect of a small set of process parameters and particle properties on the measured variables.

Numerical simulation techniques have the potential of bridging the knowledge gap because information can be obtained on local flow and stresses that are difficult, if not currently impossible, to obtain experimentally. Stewart et al. [20] and Zhou et al. [21, 22] performed simulations of bladed mixers with two flat blades using the discrete element method (DEM). They found that the frictional characteristics of particles had an impact on the velocity profiles and mixing kinetics. They also observed that particle size and density affected segregation patterns. Remy et al. [23] carried out DEM simulations of cohesionless spherical glass beads in a cylindrical vessel agitated by a four-bladed impeller. The effect of two different blade configurations (acute or obtuse blade pitch)

and the effect of particle friction on granular flow behaviors were investigated. It was found that the obtuse blade pitch orientation generated a strong 3D recirculation zone and promoted vertical and radial mixing. An increase in the sliding friction coefficient of particles led to a rise in granular temperature and an increase in diffusive mixing. Furthermore, Remy et al. [24] studied the effects of fill level and mixer properties (wall friction, blade position, and the ratio between mixer and particle diameters) on granular flow in a bladed mixer. The granular material behavior followed some simple scaling relations when the ratio of mixer size to particle diameter was increased above a critical ratio. They noticed that particle velocities and diffusivities scaled linearly with the mixer size and the blade speed. They also found that normal and shear stress profiles scaled linearly with the total weight of the granular bed. An additional study on the effect of blade speed was carried out by Havlica et al. [25] using DEM simulations.

Remy et al. [26] experimentally examined torque and shear stresses and found that they scaled linearly with the total weight of the bed as predicted by DEM simulations. Comparisons between experiments and simulations for granular flows in agitated mixers have been carried out by varying parameters including surface roughness of particles [27], polydispersity [28], and moisture content in wet systems [29]. Hare et al. [30], Zafar et al. [31], and Chandratilleke et al. [32] reported granular flow behaviors of cohesive particles in a bladed cylinder and found good agreement between experiments and DEM simulations. Although granular flows in agitated mixers have been experimentally and computationally investigated by a large number of researchers, little of these studies have

examined the effect of impeller blade configurations, blending equipment designs, material properties, and process parameters on granular flow and mixing behavior.

1.2 Granular Flow Regimes

The behavior of flowing powders and granular materials is complicated in nature, and it noticeably differs from that of fluids in motion. Unlike the well understood features of fluid flows that have been studied in fluid mechanics, constitutive equations that describe granular flows under particular initial and boundary conditions and that link material properties and operating conditions to the resulting flow behaviors are still required. A number of researchers have therefore put tremendous amounts of effort on investigating particulate and granular flow behaviors in various situations. From previous examinations, Tardos et al. [33] suggested a powder flow regime map as shown in Fig. 1.1. Solid particulate flow takes place in three different regimes depending on concentration of the granular system, the system's compression state, and shear that is being applied to the system [34]. The three granular flow regimes are known as the quasi-static regime (the slow, frictional or slowly deforming regime), the intermediate regime, and the rapid flow regime. The boundaries at which the flow regime transitions appear are not yet well determined. These different regimes of particulate flows are characterized based upon the dimensionless shear rate, γ^{o*} , which is defined as [33]

$$\gamma^{o*} = \gamma^o \sqrt{\frac{d_p}{g}} \quad (1.1)$$

where γ^o is the shear rate (s^{-1}), d_p is diameter of a particle (m), and g is the gravitational acceleration (m/s^2).

Displayed in Fig. 1.1, the static regime is where particles are at zero shear and the particulate system is in static equilibrium. From this point, the granular system requires an initial amount of shear to overcome the yield condition at which particles begin to deform and flow. After the onset of flow (the stick-slip regime), there occurs the quasi-static regime where interparticle frictional forces are predominant, particles encounter sustained contacts with their neighbors, and momentum transfer is governed by contacts between particles [34]. Solid particulate systems at high concentrations and low shear rates ($\gamma^{\circ*}$ less than 0.2) have a tendency to behave in this region. Examples of granular flows operated in the quasi-static regime include most geophysical flows [35], some gravity-driven flows (e.g. flow from a hopper in a tableting machine [36]), and some industrial mixing processes at low shear rates [23]. Continuum-like models for the quasi-static flows have been established in the past [37, 38], but still the developed constitutive relations were found to be difficult to apply to granular flows for a specific material in industrially relevant geometries.

The intermediate regime is located between the quasi-static and the rapid flow regimes. However, the boundary transition from the quasi-static to the intermediate flow regime has been uncertainly designated until now. In the intermediate flow regime, momentum transfer is regulated by both multiple particle-particle contacts and interparticle collisions. Shear stress is found to have a linear relationship with the shear rate in this region, which is the phenomenon similarly observed in fluid flows ($\tau \sim \gamma^{\circ}$). Generally scientists have focused on particulate flows in the quasi-static and the rapid flow regimes with less consideration of the intermediate regime. Continuum models have been

developed in recent years to explain flows in this intermediate region and to relate stress and strain rate to fluctuations [33, 39]. These fluctuating values of stresses and strain rates are naturally recognized to be varied with space and time, and the fluctuations increase as the dimensionless shear rate increases within the intermediate flow regime. Nonetheless, some aspects of flow inhomogeneity, such as shear bands and contact force chains, that are known to occur in high concentration particulate systems are not studied nor captured in these continuum models yet.

The rapid flow regime is the region in which granular systems at low concentrations and high shear rates are situated. In this region, particles are moving so quickly that interparticle friction can be negligible. The character of the flow in this regime is identified by instantaneous short-lived binary collisions of particles, and momentum transfer is controlled by interparticle collisions. One of the important examples of solid particulate processing technologies that is conducted in this region is fluidization [40]. The description of rapid flow of granular systems is appropriate only for a restricted range of conditions and concentrations, and this regime will be obtained less attention in this research.

1.3 Mixing Processes of Granular Materials

Mixing is a unit operation that is widely used in a variety of production processes ranging from catalytic to chemical, cosmetic, food, and pharmaceutical industries [3, 41]. In pharmaceutical manufacturing, mixing is one of the steps of critical importance that needs to be carefully controlled. Homogeneity of a mixture of excipients and an active

pharmaceutical ingredient (API) needs to be achieved to ensure that the drug concentration in a finished product is consistent and that all dosage units produced are of uniform potency [42]. There are several different types of mixers (also called blenders) used in the pharmaceutical industry. Examples of mixers include rotating drums [3], bladed mixers [42], high-shear mixers [43], agitated filter beds/dryers [26, 44], and fluidized beds [45, 46]. Bladed mixers and high-shear mixers have advantages that they are simple in construction and that they take a relatively short time to complete the mixing operation [47]. The degree of uniformity of dosage units and the resulting quality of finished products are functions of the material properties, the design of the mixer, and the operating conditions [19, 29, 48]. Process monitoring and control are therefore important to maintain stable product quality and improve process efficiency.

Mixing of solid particles in various types of blenders has been widely studied by means of the discrete element method. Alizadeh et al. [49] analyzed DEM simulation results for flow and mixing of granules in a rotating drum. They found that the Young's modulus and the static friction coefficient were the important particle properties that affected particle dynamics. Tahvildarian et al. [50] explored the effects of rotational speed and fill level on the circulation intensity and the axial dispersion coefficient of non-cohesive, monodisperse solid particles in a V-blender via DEM simulations. It was shown that the circulation intensity increased with an increase in the rotational speed and a decrease in the fill level. They also reported that the axial dispersion coefficient of the particles was a linear function of the rotational speed of the V-blender.

Alizadeh et al. [51] compared mixing efficiency of a V-blender to that of a tetrapodal blender utilizing discrete element simulations. Higher axial and radial mean velocity profiles were observed in the tetrapodal blender compared to the V-blender. They found that the tetrapodal blender provided better diffusive axial and convective radial mixing and showed a shorter mixing time compared to the V-blender due to more efficient mixing mechanisms. Further analysis demonstrated that the tetrapodal blender was less susceptible to segregation of granules than the V-blender.

DEM simulations of the mixing process of particles in a six-blade plough shear mixer and in a slant cone mixer with an intensifier bar were conducted by Alian et al [52], [53]. They studied the effect of operating conditions on mixing performance by computing the Lacey mixing index. In the plough shear mixer, they compared top-bottom loading to side-side loading and found that the rate of increase of the mixing index was larger for the side-side loading. They also showed that the mixing time decreased with an increase in the rotational speeds and that lower fill levels resulted in higher mixing indices. For the slant cone mixer, the side-side and top-bottom loading patterns led to faster mixing compared to the back-front loading. It was observed that increasing the rotational speed of the vessel enhanced the mixing index and that the kinetic energy of particles increased proportionally with the drum speed. In the slant cone mixer, the effect of the rotational direction of the agitator with respect to the direction of the drum was also analyzed, and it was shown that the mixing rate obtained in the co-rotating mode was higher than that in the counter-rotating mode.

With the current trend of moving from traditional batch manufacturing methods used in the pharmaceutical industry, continuous powder blending processes have been extensively studied in recent years. Gao et al. [54, 55] characterized and optimized a continuous mixing process by means of experimental residence time distribution (RTD) measurements and DEM simulations in order to develop a predictive model for the output mixture variance. Combined with the DEM model, Sen and Ramachandran [56] developed a new multi-dimensional population balance model (PBM) to quantify the dynamics of a continuous powder mixing process. Gao et al. [57] also proposed a scale-up strategy for a continuous powder blender that can be used for different types of materials. Although a number of research papers have studied the influence of various operating conditions on the mixing performance, only little have they focused on the impeller designs/configurations and/or the number of the blades used in the blender.

Bladed mixers are a relatively simple geometry – a cylinder with an impeller – and thus provide an opportunity for research on particulate flow and mixing. As discussed above, the effect of the number of blades on solids flow and mixing in a bladed mixer has not been studied in detail. In contrast to particulate systems, the effect of the number of impeller blades in liquid stirred tanks has been extensively investigated in a number of papers. Wu et al. [58] conducted experiments to determine the effect of the number of impeller blades on the turbulent velocity fields and the minimum speed required to suspend solids. Kumaresan and Joshi [59] investigated the effect of the number of blades in stirred tanks using computational fluid dynamics and found that increasing the number of blades from four to six led to an increase in the power consumption and the average

normal stress. Jirout and Rieger [60] carried out experiments to investigate the effect of the number of blades on a suspension of solids. They reported that the minimum speed necessary for particle suspension for three, four, and six blades decreased with the increasing number of blades. They also observed that the impeller with the lowest number of blades had the lowest torque value.

1.4 Impeller Torque and Power Consumption

As mentioned earlier, process monitoring and control are essential to maintain stable product quality and improve process efficiency. Monitoring of the mixing process can be carried out by various methods, such as employing the particle image velocimetry (PIV) technique [61], measuring agitation torque, and recording power consumption of the mixer [47]. While getting mixed, solid particulate matter exerts a load on agitator blades and vice versa, thus, giving rise to the agitation torque [15]. Changes in powder characteristics and flow behaviors in the mixer are reflected by changes in the value of the impeller torque, e.g., when the endpoint of granulation is reached [47]. The torque required to turn an impeller in a particle bed depends on a number of factors, including blade design, agitator rotational speed, material fill level, and mixer size [32, 62, 63]. In the case where agglomeration is being carried out in a high shear mixer, torque measurement helps in control and monitoring of the granulation process [64-66]. Since torque is sensitive to changes in operating conditions, with rapid measurement and good precision, it can be used as a parameter to probe the efficiency of mixer designs [64]. In addition, impeller torque measured from a laboratory scale mixer can be used to characterize and predict the risk for agglomeration in powder beds with varying degrees

of moisture content at industrially relevant scales. Bulk friction coefficient can also be measured for wet powder beds using torque data [59].

Impeller torque measurements can be implemented to monitor not only mixing and agglomeration/granulation processes, but also agitated drying processes. Drying of API crystals can be carried out in an agitated filter-bed dryer, which has advantages over tray dryers as it reduces operation time by improving heat and mass transfer. In an agitated dryer, torque data can provide a correlation between shear stress experienced by a powder bed and the degree of attrition of particles [26]. Impeller torque at the laboratory scale can also be used to obtain an estimate of the amount of work done per unit mass by the impeller at larger scales. This relationship can help improve scale up of the agitated drying process [26]. The ability to predict attrition and to obtain uniform size distribution of API particles results in better critical quality attributes of the finished dosage forms including content uniformity, dissolution rate, bioavailability, and stability.

Besides the impeller torque measurement, recording power consumed by the impeller motor can also be employed to monitor and control mixing processes. Previous research by Ritala et al. [67] demonstrated that power consumption during rotation of the blades was a function of intra-granular porosity and surface tension of a binder solution in wet mixing operations. Additionally, a correlation existed between power consumption and the strength of the moist agglomerates. An increase in cohesiveness or tensile strength of the moist granule mass resulted in a change in power consumption, indicating that the liquid solution characteristics, such as surface tension and contact angle, had an influence

on power consumption [67]. Jirout and Rieger [60] illustrated that, in the case of suspending solids in liquid systems, the power consumption required for off-bottom suspension of the solid particles could be used to compare the efficiency of different types/configurations of impellers for the mixing operation. Although power consumption measurement has been extensively carried out in previous research on the liquid mixing process, there has been limited work for monitoring mixing of solids systems.

With the current interest of moving from batch to continuous manufacturing in the pharmaceutical industry, continuous mixing processes have been extensively studied in recent years [56, 68, 69]. Vanarase et al. [70, 71] conducted experiments on a continuous powder mixer to examine the effects of operating conditions, design parameters, and material flow properties of pharmaceutical mixtures as a function of shear rate. Relative standard deviation (RSD), one of the most common mixing indices, was used to characterize mixer's performance and in turn the efficiency of the mixing process. RSD is a measure of blend homogeneity, and for a continuous process they found RSD depended on several factors such as blade rotation rate, material flow rate, and mixer blade configuration. They demonstrated that the number of blade passes, a measure of the strain, was a function of the blade rotational rate. Although there is interest in the pharmaceutical industry in continuous manufacturing, most products are still manufactured in batch mode. Thus there is still a need to better understand batch operations. The importance and measurements of the torque that the impeller blades exerted on particles and the power consumed by the agitator motor in a batch bladed mixer will be explained and discussed further in detail in Chapter 4.

1.5 Cohesive Granular Flows

In a number of real life situations, interparticle adhesion forces occur in granular systems [72]. Particle dynamics behaviors observed in cohesive granular systems are different from what is encountered in cohesionless particulate materials because of these adhesion forces [29]. The complicated behaviors of cohesive granular systems make the operation and the control of solid particulate processing difficult and cause issues founded in industries which are not easily resolved or avoided, such as non-uniform flows, bridging, channeling, accumulation on device walls, and broadening particle size distributions. Therefore, basic research involved with the transfer, mixing, and storage of cohesive granular materials is important.

Cohesion of granular materials is governed by intrinsic material and particle properties as well as moisture content in the system. Generally, there are three types of forces that are responsible for cohesion in granular systems: van der Waals forces, electrostatic forces [2], and capillary forces. In this research, we focus on capillary cohesive forces which result from the presence of moisture in granular systems. When moisture is present in the system, a liquid bridge forms in-between particles due to capillary action. The formation of this liquid bridge leads to the development of an interparticle attractive force due to surface tension and hydrostatic pressure inside the bridge. Particles in cohesive systems can occur in various states depending upon the level of moisture content in the systems: low moisture content (pendular state), intermediate moisture content (funicular state), and high moisture content (capillary state) (see Fig. 1.2) [73]. The amount of moisture present

in the system and the distribution of the liquid capillary bridge network throughout the particle bed control the resulting flow behaviors and mixing kinetics. Significance of cohesive forces with respect to gravitational and shearing forces can be measured by the granular Bond number (Bo_g), which is a dimensionless number comparing the cohesive force to the gravitational force. The impact of cohesion becomes significant when the granular Bond number is above one in slowly shearing systems. The granular Bond number will be described further in detail in Section 5.2 of Chapter 5.

1.6 Unanswered Questions

In this dissertation, a combination of both DEM computational modeling and experimental method will be used to study cohesionless and cohesive granular materials in a bladed mixer by varying equipment configurations, particle properties, and process parameters in order to gain a better understanding on how those factors affect flow behaviors and mixing kinetics. The discrete element method (DEM) will be employed to model particle dynamics with and without cohesive forces. DEM numerical simulations will be carried out to obtain solid particulate flow information that is difficult to measure experimentally. Experimental techniques such as impeller torque and power measurements will be conducted to acquire additional data, and they can be used to validate the accuracy of simulation results. The granular flow behaviors that will be investigated include particle velocities, mixing kinetics, granular temperature, particle diffusivities, bulk density, solids and void fractions, blade-particle contact forces, and normal contact force network. Furthermore, scaling-up the size of dry and wet mixing systems will be accomplished by incorporating the factors that have been studied so far,

and the influence of scale-up on the aforementioned flow behaviors and mixing performance will be also examined. The knowledge obtained from investigating granular flows in a bladed mixer at a laboratory scale can be applied to larger, more industrially relevant agitated mixing systems. An overview of previous work reported in literatures will be provided in this dissertation as well as comprehensive computational and experimental investigational plans.

This dissertation addresses some unanswered questions that still remain regarding behaviors of particulate flows in a bladed mixer. In Chapter 2, numerical and experimental methods that were employed in this research to investigate the effect of particle properties, equipment configurations, and process parameters on cohesionless and cohesive granular systems will be described. The effect of the number of impeller blades on granular flow behaviors and mixing kinetics in computational simulations will be studied in Chapter 3. Chapter 4 will emphasize experimental results on the impeller torque and power consumption measurements of granular material flows in a bladed mixer. Scale-up of cohesionless and cohesive particulate systems will be examined in Chapter 5. Overall conclusions of this dissertation will be presented in Chapter 6 along with suggestions for the direction of future research work.

1.7 Figure for Chapter 1

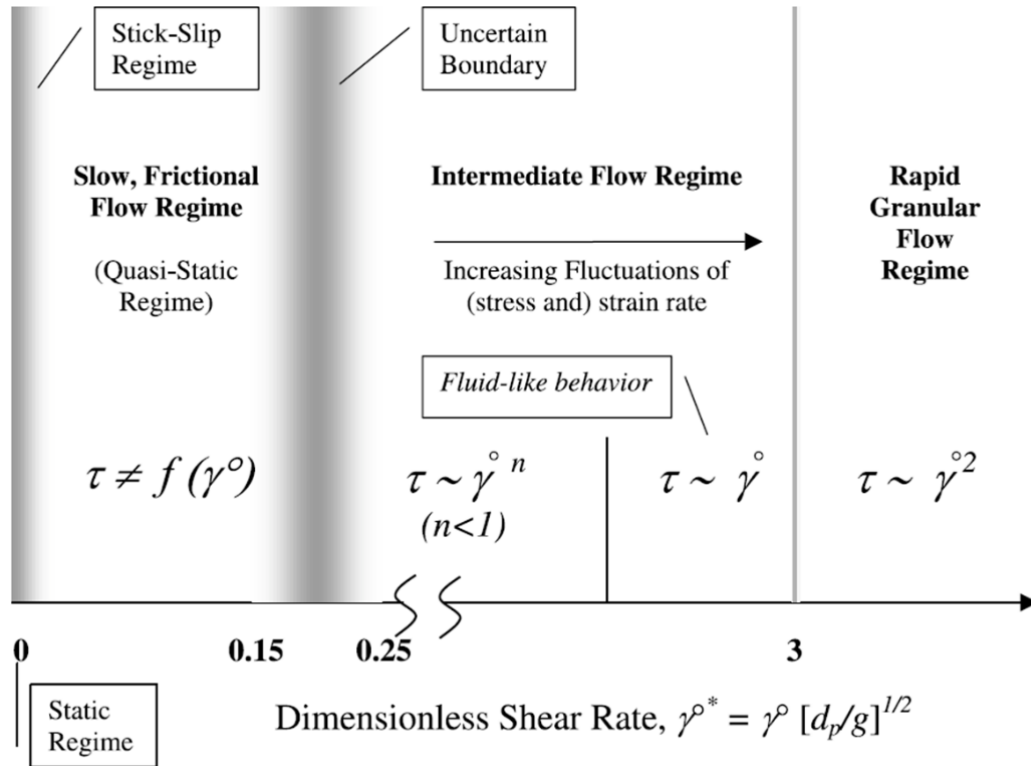


Fig. 1.1. A schematic diagram of particulate flow map as a function of the dimensionless shear rate representing the quasi-static, intermediate, and rapid flow regimes (from Tardos et al. [33]).

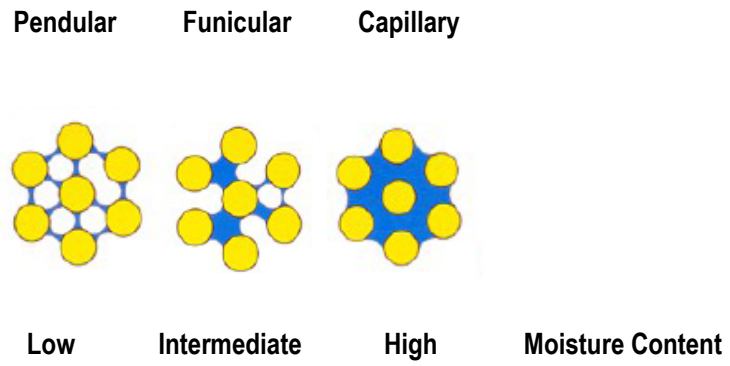


Fig. 1.2. Different states of cohesive granular materials depending on the level of moisture content in the system (adapted from am Ende et al. [73]).

Chapter 2. Numerical and Experimental Methods

2.1 Numerical Simulations

Although experimental work can provide insight into granular flow behaviors, these studies are often limited by the capabilities of current analytical techniques. Numerical simulation techniques have the potential of bridging the knowledge gap because information can be obtained on local flow and stresses that are difficult, if not currently impossible, to obtain experimentally. A discrete element method (DEM) is one of the numerical tools that has been widely used in recent years to investigate particulate flows in various systems ranging from simple shear flows to more complicated geometries [74, 75]. This computational technique has granted understanding with regard to a granular system's dynamics and transient behavior. The DEM models used in this dissertation as well as theories behind these models will be described in the following sections of this chapter. Analytical methods for calculating important macroscopic quantities from the discrete simulation data will be also explained.

2.1.1 Theoretical Basis

Macroscopic flows of granular systems are dictated by particle interactions that happen at the microscopic level. DEM describes behaviors of particulate systems by taking into account interparticle or particle-boundary contacts. DEM models are commonly categorized into two classifications: hard-sphere models and soft-sphere models [74]. In this work, the soft-sphere approach was adopted as it can simulate granular systems in which particles encounter sustained contacts and as it is more proper for solids particulate

processing in quasi-static and intermediate flow regimes. For soft-sphere DEM model simulations (also called time-stepping simulations), Newton's equations of motion are numerically integrated with time for each particle starting from an initial system configuration. If the time-step for integration is sufficiently small, it can be assumed that the state of a particle is only affected by contact with its neighbors (and the gravitational force). Therefore, at any given time-step, the discrete element method considers only pair-wise interactions of neighboring particles or between a particle and a boundary.

2.1.2 Contact Force Model

The DEM method provides information regarding the particle's position, velocity, and resultant forces. The motion of each particle is described by the following equations, i.e.,

$$m_i \frac{dv_i}{dt} = \sum_j (F_{ij}^N + F_{ij}^T) + m_i g \quad (2.1)$$

$$I_i \frac{d\omega_i}{dt} = \sum_j (R_i \times F_{ij}^T) + \tau_{rij}. \quad (2.2)$$

Both, Eqs. (2.1) and (2.2), are written for all three coordinate directions. Here m_i , v_i , I_i , ω_i , and R_i are the mass, linear velocity, moment of inertia, angular velocity, and radius of particle i , respectively, and g is the acceleration due to gravity. F_{ij}^N and F_{ij}^T are the normal and tangential forces, respectively, resulting from the contact of particle i with particle j . The effect of rolling friction μ_r is included in the stress term τ_{rij} , which is given by $\tau_{rij} = -\mu_r |F_{ij}^N| R_i \omega_i$. In this work, the model developed by Tsuji et al. [76] was adopted to compute contact forces. This model provides a nonlinear force based on Hertzian contact theory. The normal contact force is given by

$$F^N = -\tilde{k}_n \delta_n^{3/2} - \tilde{\gamma}_n \dot{\delta}_n \delta_n^{1/4} \quad (2.3)$$

where \tilde{k}_n is the normal stiffness coefficient, δ_n is the normal displacement, and $\tilde{\gamma}_n$ is the normal damping coefficient. The normal stiffness coefficient is obtained from

$$\tilde{k}_n = \frac{E\sqrt{2R^*}}{3(1-\sigma^2)}. \quad (2.4)$$

with E being the particle's Young's modulus and σ the particle's Poisson ratio. R^* is defined as the effective radius of the contacting particles and is obtained by

$$R^* = \frac{R_i R_j}{R_i + R_j}. \quad (2.5)$$

The normal damping coefficient is given by

$$\tilde{\gamma}_n = -\ln e \frac{\sqrt{m\tilde{k}_n}}{\sqrt{(\ln e)^2 + \pi^2}} \quad (2.6)$$

where e is the coefficient of restitution. This model assumes a constant coefficient of restitution and results in a velocity-dependent collision time. Although experimental data suggests an impact-velocity dependent coefficient of restitution, this model has been shown to produce DEM results in good agreement with experimental data [76-79] and comparable with other commonly used contact models [80, 81].

The tangential force is calculated from

$$F^T = -\tilde{k}_t \delta_t - \tilde{\gamma}_t \dot{\delta}_t \delta_n^{1/4} \quad (2.7)$$

where \tilde{k}_t is the tangential stiffness coefficient, δ_t is the tangential displacement, and $\tilde{\gamma}_t$ is the tangential damping coefficient. The tangential stiffness coefficient is based on the work from Mindlin [82] and is given by

$$\tilde{k}_t = \frac{2\sqrt{2R^*}G}{2-\sigma} \delta_n^{1/2} \quad (2.8)$$

where G is the particle's shear modulus. The tangential displacement is calculated by

$$\delta_t = \int v_{rel}^t dt \quad (2.9)$$

where v_{rel}^t is the relative tangential velocity of the colliding particles and is defined as

$$v_{rel}^t = (v_i - v_j) \cdot s + \omega_i R_i + \omega_j R_j. \quad (2.10)$$

In Eq. (2.10), s is the tangential decomposition of the unit vector connecting the center of the particle. The tangential force is limited by the Coulomb condition, $F^T < \mu_s |F^N|$. When the tangential force obtained from Eq. (2.7) exceeds the Coulomb limit, the tangential displacement is set to $\delta_t = F^T / \tilde{k}_t$ in order to account for slip during a contact. It is interesting to note that, as a consequence of setting δ_t equal to F^T / \tilde{k}_t , δ_t is always less than F^N / \tilde{k}_t . In this work, the tangential damping coefficient is assumed to be the same as the normal damping coefficient. In the Appendix attached at the end of dissertation, we present a comparison between the PIV experimental data and the DEM simulation results for normalized velocity fluctuations of non-cohesive granular flows in a 4-bladed mixer in order to validate the computational model used in this work.

2.1.3 Cohesive Force Model

Once the flow of dry monodisperse spherical granular materials has been characterized, the particle dynamics code will be modified in computational modeling to include cohesion forces due to capillary liquid bridges in order to study a system of cohesive particles. Therefore, the equation of translational motion of particles (Eq. (2.1)) will become

$$m_i \frac{dv_i}{dt} = \sum_j (F_{ij}^N + F_{ij}^T) + F_{ij}^C + m_i g \quad (2.11)$$

where F_{ij}^C is the cohesive force experienced by particle i due to the formation of a liquid bridge between it and particle j . The same equation of rotational motion of particles (Eq. (2.2)) will be employed in the cohesive particle dynamics model.

In this section, the computational model for cohesive granular flows in numerical simulations will be set up. For the case of low moisture contents, also known as the pendular regime (see Fig. 1.2 in Chapter 1), it can be assumed that discrete liquid bridges form only when particles come into contact. This assumption makes the inclusion of a capillary force into a particle dynamics algorithm straight forward. A schematic representation of the liquid bridges in the pendular regime is shown in Fig. 2.1. The capillary force (F^C) resulting from the surface tension and the pressure difference inside the liquid bridge can be expressed as

$$F^C = 2\pi\gamma \sin\beta \sin(\beta + \theta) + \pi R^2 \Delta P \sin^2\beta \quad (2.12)$$

where, as denoted in Fig. 2.1, β is the half filling angle, θ is the contact angle of the liquid bridge, γ is the surface tension of the liquid, R is radius of the particle, and ΔP is the pressure difference across the air-fluid interface.

In order to obtain the exact value of the cohesive force, due to the curvature of the liquid bridge, the Laplace-Young equation must be solved. Several solutions to this equation are available in the literature [83-85]. The cohesion force model proposed by Mikami et al. [84] will be used for this work. This model is based on an empirical fit of regression expressions acquired from the numerical solutions of the Laplace-Young equation. In the Mikami model, the cohesion force can be calculated from

$$\hat{F}^C = e^{A\hat{h} + B} + C \quad (2.13)$$

$$A = -1.1\hat{V}^{-0.53} \quad (2.14)$$

$$B = (-0.34 \ln \hat{V} - 0.96)\theta^2 - 0.019 \ln \hat{V} + 0.48 \quad (2.15)$$

$$C = 0.0042 \ln \hat{V} + 0.0078 \quad (2.16)$$

where \hat{F}^C is the normalized capillary force which is defined as $\hat{F}^C = F^C/2\pi R\gamma$, \hat{V} is the dimensionless liquid bridge volume which is defined as $\hat{V} = V/R^3$ where V is volume of the liquid bridge, and \hat{h} is the dimensionless separation distance between the particle-particle or particle-wall surfaces which is defined as $\hat{h} = h/R$ where h is the separation distance between two surfaces. The constants A , B , and C can be computed from Eqs. (2.14) to (2.16) and are fitted from the solution to the Laplace-Young equation. When the pendular bridges are stretched, the thickness of the liquid layer decreases eventually leading to the rupture of the liquid bridge. The distance at which these pendular bridges break is called the dimensionless critical rupture distance ($\hat{h}_c = h_c/R$, where h_c is the critical rupture distance) and is given by the following equation proposed by Lian et al. [83]:

$$\hat{h}_c = (0.62\theta + 0.99)\hat{V}^{0.34} \quad (2.17)$$

The presence of moisture also leads to the development of viscous forces between particles. The capillary number (Ca) relates the magnitude of the viscous force to the capillary forces in a liquid bridge, and it is calculated by

$$Ca = \frac{\eta U}{\gamma} \quad (2.18)$$

where η is the dynamic viscosity of the liquid and U is the characteristic velocity. For a water wet granular materials flowing at a velocity of 0.2 m/s (a typical velocity in a bladed mixer), the value of the capillary number is $Ca < 0.01$. This indicates the effect of the viscous forces is negligible compared to the effect of the capillary forces. The effect of dynamic viscous forces will not be considered in this work.

There were few assumptions that should be made to implement the liquid bridge model along with the cohesive contact force model into the DEM simulation protocol [29]:

1. The total amount of liquid in the system is uniformly distributed throughout the entire granular bed such that each capillary bridge has the same volume of liquid.
2. There is no condensation nor evaporation of the liquid occurred in the systems.
3. A pendular liquid bridge is formed at the point of contact when two particles come in contact. The liquid bridge continues to act between the two particles until the distance between the two particles exceeds the critical rupture distance, h_c .
4. A pendular liquid bridge is formed at the point of contact when a particle comes in contact with the mixer wall. The liquid bridge continues to act until the distance between the particle and the wall exceeds the critical rupture distance, h_c .
5. Liquid bridges move tangentially and slip over the surfaces of the particles and the walls, i.e., the capillary force acts only in the normal direction.
6. The roughness of particle surfaces is completely covered by the liquid layer making the particles appear smooth and completely wettable [86].

2.1.4 Mixer Geometry and Input Parameters

A schematic of the mixer geometry used in our studies is shown in Fig. 2.2. In the coordinate system we have adopted, the origin is located at the center of the cylindrical mixer's bottom plate. Table 2.1 shows dimensions of the mixer that will be used in our base case simulations in Chapter 3. D_0 denotes the diameter of the top and bottom plates of the cylindrical mixer. D_1 is the diameter of the cylindrical impeller shaft, and L is the

distance from the center of the mixer to the edge of the blades. H_0 is the height of the granular bed above the blades. H_1 is the blade height or vertical span of the blades. The height from the bottom of a mixer to the bottom of the blades is denoted by H_2 .

The input parameters used in our base case simulations are listed in Table 2.2. These values correspond to the physical properties of glass beads, except for the value of Young's modulus which is decreased to reduce computational time [20, 22]. The values of the input parameters have been shown to afford DEM results comparable to those obtained experimentally with glass beads [20, 22]. The physical properties listed in Table 2.2 were used for the particles, the blades, and the mixer walls in all simulations. The particle bed consisted of monodisperse, cohesionless or cohesive spherical glass beads. Particles were created in the simulation software and allowed to settle under gravity while the blades remained stationary. A sufficient number of particles were created so that the final fill level of particles in the mixer just covered the top of the blades.

For cohesive granular systems (Section 5.2 in Chapter 5), the input parameters used for the capillary liquid bridge model are listed in Table 2.3. Most of the liquid properties, except for the surface tension (which will be explained later in Chapter 5), are those of water. A contact angle of $\theta = 0^\circ$ was used since this simulates the formation of liquid bridges in hydrophilic materials [87]. The amount of liquid in granular systems is represented by the liquid volume fraction (ϕ_{liq}) which is defined as the ratio of the total volume of liquid in the system to the total volume of particles. In this dissertation, granular systems with ϕ_{liq} equal to 0, 0.01, and 0.045 were studied. By assuming a

uniform distribution of liquid within the granular bed, the values of \hat{V} can be computed. For an average particle coordination number of 5 (typical in the cohesionless particle flows in an agitated mixer at the blade rotational speed used in this work), the ϕ_{liq} values listed above are equivalent to the \hat{V} values of 0, 0.021, and 0.094, respectively. The amount of liquid in each capillary bridge is assumed to be constant in all simulations, i.e., the \hat{V} value is the same for each particle-particle and particle-wall contact.

Blade movement was started once deposition of particles had finished. After the total kinetic energy of the system reached a constant value, the system was considered to be at a statistically steady state and measurements were commenced. Under these conditions, the steady state was reached within 2 seconds of the blade movement. Base case simulations in Chapter 3 were performed using a blade rotational speed of 20 revolutions per minute (RPM). At this rotational speed, granular flow in the bladed mixer occurred in the quasi-static granular flow regime where previous work has shown that stresses are independent of the blade speed as long as the blades are moving [23]. The blades were rotating counter-clockwise, which led to an obtuse-angle blade orientation, a commonly used configuration in industries. A counter-clockwise rotation is denoted by a positive tangential velocity.

2.1.5 Macroscopic Flow Properties

In this dissertation, a numbers of granular flow properties and measures of mixing kinetics were computed and employed to characterize particle dynamics simulations. Spatial and temporal averaging of the discrete particle data were implemented to

determine such macroscopic variables. In this section, important macroscopic quantities, including granular temperature, particle diffusivities, Péclet number, bulk density, solids and void fractions, collisional stresses and pressure within a particle bed, relative standard deviation, and Lacey index, will be explained.

2.1.5.1 Granular Temperature

Granular temperature is one of the important macroscopic properties of interest of a granular assembly since it provides a measurement for the degree of random movement of particles in the system. Knowledge of granular temperature profiles can assist in the development of continuum models. Granular temperature profiles can be used to gauge the diffusive behavior of particles and the tendency of the system to segregate as temperature gradients have been shown to produce segregation. The granular temperature (T) is defined as [19]

$$T = \frac{1}{2} \langle u'u' \rangle \quad (2.19)$$

where u' is the fluctuation velocity of each particle, which is the instantaneous deviation from the mean velocity in a control volume around the point being examined. The mean velocity is the averaged velocity for a group of particles within the control volume at each particular time-step. $\langle \rangle$ denotes the temporal averaging of the quantity $u'u'$ (the square of the fluctuation velocity of each particle within the control volume). Temporal averaging is done after the particulate system reaches the quasi-steady state. In our previous computational work [23, 24, 29], we were able to find a range of control volume sizes and time intervals where the values of granular temperatures did not change. The time interval used for temporal averaging of the square of the fluctuation velocity $\langle u'u' \rangle$

for computing granular temperatures is 0.1 s. Changing the time interval within the range of 0.1 to 1 second did not affect the granular temperature values. The control volume chosen for calculation of the mean velocity and the granular temperature in this section is defined by a cube with a size of six particle diameters and centered at the specified coordinates of vertical position y and of radial position r . The coordinates are selected so that the control volumes are located in the positions between the impeller shaft and the cylinder wall, and that the control volumes include particles just above and within the span of the blades.

2.1.5.2 Particle Diffusivities and Péclet Number

Particle motion at the microscopic level was also gauged by calculating particle diffusivities which describe the mass flux rate due to particles' random walk. The diffusive tensor calculation was taken from Campbell [88] and is given by

$$D_{ij} = \langle (\Delta x_i - \overline{\Delta x_i})(\Delta x_j - \overline{\Delta x_j}) \rangle / 2\Delta t \quad (2.20)$$

where Δx_i represents the particle displacement in the i direction relative to the particle's initial position, $\overline{\Delta x_i}$ is the mean particle displacement, and D_{ij} is the corresponding diffusion coefficient in the i direction due to a gradient in the j direction. Particle diffusivities were computed with a Δt of $1/4$ of a revolution and were averaged over all the particles within the span of the blades. However, particle diffusion has been previously shown to depend on system geometry and size in dense granular flows [89]. Therefore, particle diffusivities were normalized by the tip speed of the blades (V_{tip}) and the mixer diameter (D). For example, the normalized diffusion coefficient in the tangential direction ($D_{\theta\theta}^*$) can be computed by

$$D_{\theta\theta}^* = D_{\theta\theta} / DV_{tip}. \quad (2.21)$$

The convective and diffusive contributions to particle motion were compared by calculating the Péclet number (Pe_{ij}), which is defined as

$$Pe_{ij} = \frac{U_i R_{cyl}}{D_{ij}} \quad (2.22)$$

where U_i is the average particle speed in the i direction, R_{cyl} is the mixer radius, and D_{ij} is the corresponding diffusion coefficient.

2.1.5.3 Bulk Density, Solids Fraction, and Void Fraction

Bulk density of a system is another important macroscopic property of a granular assembly. Measuring the bulk density of a granular system can provide insight into the system's compression and dilation states and can help to determine other macroscopic properties such as pressure. The time-averaged solids fraction (ϕ) of the granular bed is defined as

$$\phi = \frac{\rho_{bulk}}{\rho_p} \quad (2.23)$$

where ρ_{bulk} is the bed bulk density during flow and ρ_p is the density of the particles.

Void fraction (ε) is a measure of the empty spaces available in the granular bed that are not occupied by the solid particles where

$$\varepsilon = 1 - \phi. \quad (2.24)$$

In particle dynamics simulations, the local voidage within the particle bed is calculated using the method of overlapping spheres. Spherical control volumes are created throughout the computational domain, and the number of particles which overlap each

spherical control volume is determined. The local void fraction is calculated by subtracting the overlapping volume of each particle from the control volume size as the following equation:

$$\varepsilon = 1 - \frac{\sum_k (\pi(R_C + R_k - a)^2 [a^2 + 2a(R_k + R_C) - 3(R_k^2 + R_C^2) + 6R_k R_C])}{12aV_C} \quad (2.25)$$

where R_C is the radius of the spherical control volume, R_k is the radius of particle k , a is the distance between the center of the particle and the center of the control volume, and V_C is the size (volume) of the control volume.

2.1.5.4 Collisional Stresses and Pressure

According to previous research [23], collisional stresses were found to be three orders of magnitude larger than kinetic stresses. Therefore, it is assumed in this dissertation that only the contribution of collisional stresses due to particle collisions is considered and responsible for calculation of stresses. Following the methodology outlined by Campbell [34], collisional stresses (τ_{ij}) within a granular bed are obtained and computed from

$$\tau_{ij} = \frac{d}{V_C} \langle F_i k_j \rangle \quad (2.26)$$

where d is particle diameter, V_C is the size (volume) of a control volume, F_i is the total contact force, and k_j is the unit vector pointing along the line connecting the centers of the two colliding particles. As before, $\langle \rangle$ represents the temporal averaging within the control volume. Stresses in a bladed mixer were known to be dependent upon the scale of particulate systems [90]; therefore, the computed stress values are affected by the size of the control volume. The size of the control volume used in this work was determined by varying this parameter until the stress values obtained are independent of the control volume size (~ 5 particle diameters).

The collisional stress tensor is computed in a 3-dimensional cylindrical coordinate system. Analysis from previous work [23] revealed that following the aforementioned methodology a symmetric stress tensor was acquired, for example $\tau_{\theta r} = \tau_{r\theta}$. The stress tensor components on which this research's attention is primarily focused are the average normal stress (τ_{ii}) and the shear stress in the plane of the impeller blade rotation ($\tau_{\theta r}$). Knowing the normal stress values, the pressure (P) inside a granular bed can be calculated by

$$P = \frac{1}{3}(\tau_{\theta\theta} + \tau_{rr} + \tau_{yy}) \quad (2.27)$$

where $\tau_{\theta\theta}$, τ_{rr} , and τ_{yy} are the normal stresses in the tangential, radial, and vertical directions, respectively.

2.1.5.5 Relative Standard Deviation

Relative standard deviation (RSD) is one of the most common mixing indices that can be used to characterize mixer's performance and in turn the efficiency of the mixing process. RSD is a measure of blend homogeneity, and the RSD values depend on several factors such as blade rotation rate, material flow rate, and mixer blade configuration. Mixing performance of granular flows in bladed mixers can be measured by performing statistical analysis on particle concentration for a particular type of particles and calculating the systems' relative standard deviation values in the computational domain. At a specific time step, we calculate the RSD of a particular type of particle concentration for the whole system. The RSD is computed from the following formula:

$$\text{RSD} = \frac{\sigma_{conc}}{M_{conc}} \quad (2.28)$$

where σ_{conc} is the standard deviation of the specified particle concentration over all samples taken and M_{conc} is the overall mean particle concentration. The RSD value obtained can be highly sensitive to a sample size and the sample number. The sample grid size for the RSD calculation is determined by varying the sample number and size until the RSD value obtained is independent of sampling grid (approximately 5-particle diameters). While a fully segregated system yields an RSD value of 1, a perfectly mixed system results in an RSD value of zero.

2.1.5.6 Lacey Index

Besides relative standard deviation, discrepancies in the degree of mixing (or mixing kinetics) for different cases of numerical simulations can be also measured by computing the Lacey's mixing index of the granular system. The Lacey index can be used to analyze spatial distribution of one component in a binary mixture and quantify the global mixing state in the mixer and the mixing performance. The Lacey index (M) is given by [21, 42]

$$M = \frac{\sigma_0^2 - \sigma^2}{\sigma_0^2 - \sigma_r^2} \quad (2.29)$$

where σ_0^2 is the variance of an initial, typically completely segregated state, σ_r^2 is the variance of a fully random or perfectly mixed state, and σ^2 is the actual variance obtained from the mixing process. σ_0^2 and σ_r^2 are given by the following equations:

$$\sigma_0^2 = p \cdot q \quad (2.30)$$

$$\sigma_r^2 = \frac{p \cdot q}{N} \quad (2.31)$$

where p and q are the proportions of the two components in the binary mixture, and N is the total number of particles in the mixture. The actual variance σ^2 of a mixture is analyzed using the equation below:

$$\sigma^2 = \frac{1}{N} \sum_{i=1}^{m_s} [(p_i - p)^2] \quad (2.32)$$

where p_i is the proportion of one component in the i th sample and m_s is the number of samples.

2.2 Experimental Method

2.2.1 Experimental Set-up

The laboratory equipment used in this work is shown in Fig. 2.3. The unit was composed of a bladed mixer, a signal transducer with a load cell, a data recorder with a monitor, and a power meter. The unit is similar to what was used in previous work [26]. A cylindrical glass vessel and Teflon® impeller blades were purchased from Chemglass Life Sciences®. The glass chamber was mounted on a rotating table with a metal lever arm which applied force on a load cell when the blades moved through the particle bed. In the experiments, the impeller blades were attached to one end of a cylindrical stainless steel agitator shaft which was connected to a motor at the other end. The motor was firmly held on a Chemglass® benchtop support stand and wired to a digital motor controller which was used to adjust the direction and the speed of rotation of the impeller blades. The data acquisition device used in this research was a Yokogawa™ DX1006-1. It was employed to record voltage signals to monitor the blade rotation speed and the force applied on the load cell (from which torque can be calculated). The power meter used was a Vernier Software & Technology® Watts Up PRO; it was connected to the motor controller to measure power consumed by the impeller blades when rotated through a granular bed.

A schematic of the mixer geometry used in this work is depicted in Fig. 2.2, and the dimensions of the bladed mixer are reported in Table 2.4. The cylindrical vessel has an inner diameter (D_0) of 100 mm and a total internal height of 155 mm, which can hold a volume of approximately 1.2 liters. The mixer is mechanically agitated by impeller blades, and the agitator shaft is placed at the center of the cylindrical mixer. The diameter of the cylindrical impeller shaft (D_1) is 10 mm, and H_0 is the height above the blades which is 128 mm for our standard setup. The vertical span of the impeller blades (H_1) is 25 mm, and the length (L) of each blade measured from the center of the impeller shaft to the edge of the blade is 45 mm for the initial impeller blades used in this work. The clearance between the bottom of the blades and the base of the mixer (H_2) is set to approximately 2 mm in all experiments.

2.2.2 Materials Used in Experiments

The granular material used in this research was Dragonite® composite glass beads (Jaygo Incorporated, Randolph, NJ) with a density of $2,500 - 2,550 \text{ kg/m}^3$. Physical properties of the cohesionless spherical glass beads used in the experiments are listed in Table 2.5. Three different diameter sizes of the beads were utilized in the experiments: 1 mm (0.60 – 1.40 mm), 2 mm (1.70 – 2.36 mm), and 5 mm (4.71 – 5.01 mm). Particle size distribution analysis of the glass beads was conducted using sieve analysis, and the ranges for the three different particle diameters were reported in the parentheses above. The glass beads of the 1-mm diameter were colorless, and the 5-mm particles were surface-colored purple. Two types of 2-mm glass beads were used in the experiments: surface-colored red beads and clear beads. The 2-mm red glass beads were used for our

initial experiments while the 2-mm colorless glass beads were used for subsequent particle surface roughness modification experiments which will be described later in Section 2.2.4. It was noticed that after running the experiment for some time, particles started to stick to the walls of the vessel. An anti-static ionization blower and anti-static spray were therefore used to reduce static charges [2] and to produce reliable and repeatable results.

2.2.3 Impeller Torque and Power Measurements

Before performing each experiment, the impeller shaft was first placed at the center of the bladed mixer, and then glass beads were gently loaded into the mixer and allowed to settle while the blades remained stationary. Blade movement was then started, and the signal measurement and recording were commenced. The impeller blades were rotated in the counter-clockwise direction leading to an obtuse-angle blade orientation which is a commonly used configuration in industry. Experiments were carried out at various blade rotational speeds ranging from 10 to 200 revolutions per minute (RPM). At these shear rates, granular flows in the bladed mixer occurred in the quasi-static and intermediate regimes according to the flow regime map proposed by Tardos et al. [33]. When starting the blade movement, the rotational speed of the impeller was gradually increased from 0 RPM to a desired rotation rate for each experiment. In this research, the signal data was measured and recorded once every second for the time-averaged torque and every 0.125 seconds for the torque fluctuation analysis. The total time duration for recording signals for each individual experiment was 3 minutes and 30 seconds, and for each blade rotational speed the experiment was repeated three times. Mean and standard deviation of

instantaneous data at each time step were calculated from the three separate data sets. In general, the steady state was usually reached within 30 – 45 seconds of the blade movement for all experiments. Once the steady state was reached, the time averaging procedure for the mean torque and power readings was performed throughout the measurement period.

The torque was measured by measuring a force and multiplying this by the lever arm length. In this set-up, force was measured by using a load cell attached to a metal arm that pivots around a rotating table in which the glass vessel assembly sits, as shown in Fig. 2.3. As the impeller moves through the granular bed, the blades transmit force to the particle bed causing the material to rotate relative to the mixer wall. The rotation of the glass vessel causes the pivot arm to apply force on the load cell which measures the force. With this set-up, torque can be calculated from cross-multiplying the length of the lever arm and the measured force:

$$\vec{T} = \ell \times \vec{F} \quad (2.33)$$

where \vec{T} is the torque acting on the load cell, ℓ is the lever arm length (whose value is 17.9 cm in this set-up), and \vec{F} is the measured force that the lever arm acts on the load cell.

It can be shown that the torque exerted on the impeller at the shaft equals the torque exerted on the mixer (walls) due to the moving granular bed [91]. In addition, the average shear stress experienced by the granular bed can be related to the impeller torque [26, 92]:

$$\langle \tau_{\theta r} \rangle = \frac{\vec{T}}{2\pi R_{\text{cyl}}^2 H} \quad (2.34)$$

where $\langle \tau_{\theta r} \rangle$ is the average shear stress, \vec{T} is the measured impeller torque, R_{cyl} is the radius of the cylindrical glass mixer, and H is the height of the particle bed when the blades are rotating. Moreover, work done by the impeller can be calculated from the impeller torque by using the following expression:

$$W = \int_0^t \vec{T} \cdot \omega dt \quad (2.35)$$

where W is the work done by the impeller blades over time t , \vec{T} is the impeller torque, and ω is the angular velocity of the impeller blades.

As described above, the torque measured in our experiments is the torque needed to move the granular bed. However, for power consumption measurement, the power is made up of two components. One component is the power needed to run the motor, and the other is the power needed to move the particle bed. The power needed to run the motor is therefore subtracted from the actual power reading measured by the power meter when a mixer is loaded with particles:

$$P^* = P - P_{\text{emp}} \quad (2.36)$$

where P^* is an adjusted power for the charged cylinder for a given RPM, P is the actual power measured by the power meter for the charged cylinder for a given RPM, and P_{emp} is the power measured for an empty mixer at that same RPM. All powers are measured in watt (W).

2.2.4 Particle Surface Roughness Modification

A method for modifying the surface of glass beads is described by Remy et al. [27], and this protocol was adopted in this study in order to investigate the effect of particle surface friction on the impeller torque and power. In this procedure, a rotating drum was employed to coat the surface of 2-mm colorless glass beads with magnesium stearate (MgSt). Magnesium stearate was chosen as a coating material due to the increased asperity and the irregular shape of its primary particles. The adhesive interaction between MgSt and the surface of the glass beads occurred to physically coat the glass beads with MgSt. The magnesium stearate was purchased from Sigma-Aldrich® (CAS No. 557-04-0) and was composed of irregular plates with a mean diameter of 15 μm . The rotating drum used as a coater was made out of glass with an outer diameter of 20.5 cm and a length of 8 cm. The rotating drum contained 4 Teflon® baffles equally spaced along the side wall of the drum. The baffles were 3 cm deep and 7 cm in height. The protocol for particle surface roughening is briefly mentioned as follows: In total 200 – 400 g of the beads were added into the rotating drum, followed by 50 – 100 g of MgSt to achieve a 25% w/w MgSt concentration. The drum was rotated at 30 RPM under atmospheric pressure for 15 minutes. Some small MgSt agglomerates were created during the coating procedure. The resulting mixture was sifted through No. 8 and No. 12 sieves in order to separate the coated beads from the MgSt agglomerates. The resulting MgSt-coated glass beads had a particle diameter ranging from 1.7 mm to 2.4 mm, a size range similar to that of the uncoated glass beads (see Section 2.2.2). Using a Freeman Technologies FT4 rheometer, a macroscopic/bulk friction coefficient (μ) was measured. For the 2-mm MgSt-coated glass beads the macroscopic friction is 0.38 ± 0.008 compared to 0.32 ± 0.009 for the

uncoated beads [27]. Results for the effect of particle surface roughness on measured impeller torque and power consumption will be discussed in Section 4.3 of Chapter 4.

2.2.5 Water Addition for Cohesive Granular Systems

In order to study the effect of moisture content on the experimentally measured impeller torque and power draw, water as a liquid binder was incorporated into a particle bed to add cohesive forces to the granular system. Three levels of moisture content were chosen in this work – 1%, 2.4%, and 4.5% v/v – according to the research previously done by Remy et al. [29]. The experimental set-up (see Section 2.2.1) for the wet granular systems was similar to that in the dry cases with 300 g of 2-mm glass beads, except for the fact that water was added and moisture content was varied in the wet systems. To start the wet particle experiments, colorless beads were gently loaded into the cylindrical mixer after the blades were initially placed in a position. The impeller blades were then set into motion by rotating in the counterclockwise direction at 25 RPM, and water was added dropwise from the top at different locations in a container with the use of a small dropper. A sheet of aluminum foil was taken to cover the top opening of the mixer in order to minimize water loss due to evaporation. The wet glass bead bed was allowed to mix for 5 min prior to taking the torque measurements. After the total amount of water was uniformly mixed throughout the whole particle bed, experiments were carried out using a rotational speed of the blades within the range from 10 to 200 RPM. The impeller shaft was driven by a motor with a speed controller with an accuracy of ± 0.1 RPM under load. Torque data in a wet granular system was recorded for 210 s for each experiment. This water addition protocol was found to yield reproducible results in the laboratory [29] and

was consistent with the procedure used by Lekhal et al. [19]. After a set of experiments was done, wet beads were removed out of a mixer and then the inner surface of the mixer as well as the surface of the blades were let to be dry. A new set of glass beads was loaded followed by addition of the desired volume of water into a mixer before beginning to perform a new set of experiments.

2.3 Figures for Chapter 2

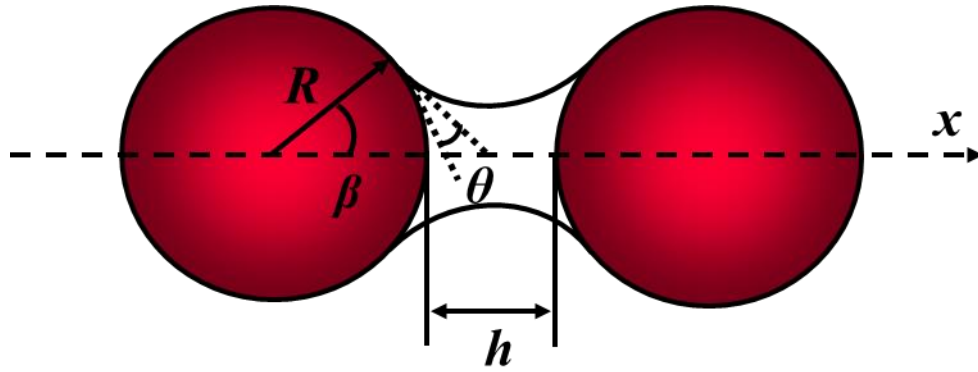


Fig. 2.1. A schematic of a capillary bridge between two particles (from Remy [93]).

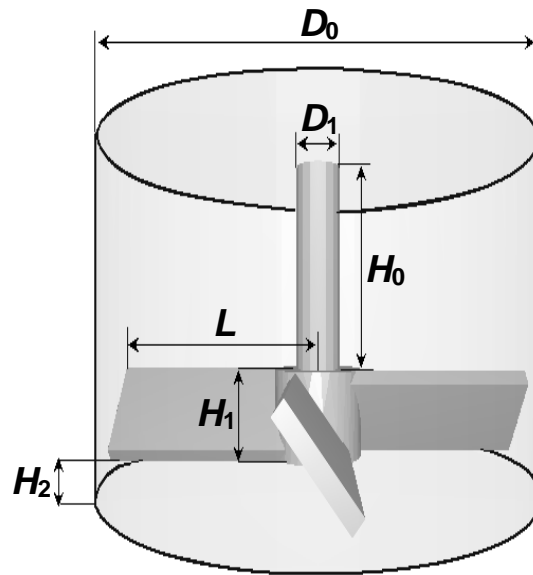


Fig. 2.2. A schematic of the 4-bladed mixer used in the DEM simulations and the experiments. Dimensions of the unit are shown in Tables 2.1, 2.4, and 2.6.

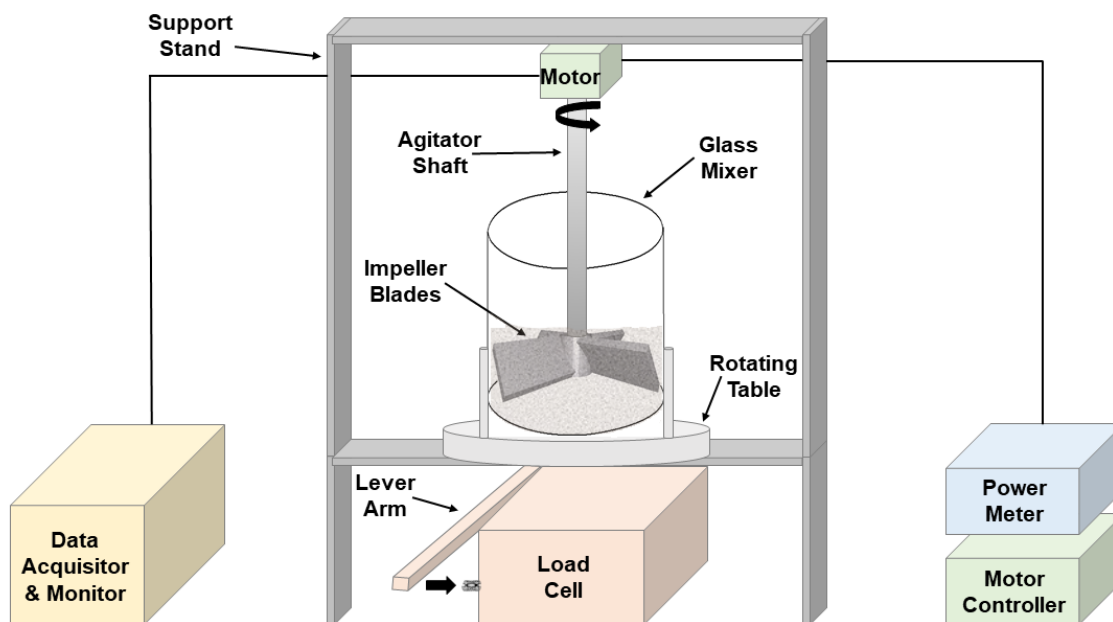


Fig. 2.3. A schematic of the laboratory experimental set-up for the impeller torque and power measurements.

2.4 Tables for Chapter 2

Table 2.1. Mixer dimensions for the base cases.

Dimension	Value (mm)
D_0	315
D_1	32.5
L	152.5
H_0	105
H_1	45
H_2	5

Table 2.2. Input parameters in EDEM™ simulations.

Variable	Symbol	Value
Particle diameter	d	3.5, 5, 10 mm
Number of particles	N	5,000 – 216,000
Poisson's ratio	σ	0.25
Shear modulus	G	2.6×10^6 Pa
Particle density	ρ	2.2 g/ml
Coefficient of restitution	e	0.6
Sliding friction coefficient	μ_s	0.5
Rolling friction coefficient	μ_r	0.005
Time step		$< 1 \times 10^{-5}$ s
Save interval		0.1 – 0.01 s
Simulator grid cell size		2 R min

Table 2.3. Cohesive force model input parameters in EDEM™ simulations.

Variable	Symbol	Value
Liquid surface tension	γ	1.825 N/m
Contact angle	θ	0°
Liquid density	ρ_{liq}	1.0 g/ml
Liquid volume fraction	ϕ_{liq}	0 – 0.045
Dimensionless liquid bridge volume	\hat{V}	0 – 0.094
Granular Bond number	Bo_g	5

Table 2.4. Dimensions of a laboratory mixer.

Dimension	Value (mm)
D_0	100
D_1	10
L	45
H_0	128
H_1	25
H_2	2

Table 2.5. Glass bead properties used in experiments.

Variable	Symbol	Value
Particle diameter	d	1, 2, and 5 mm
Particle density	ρ_p	2.50 – 2.55 g/ml
Macroscopic friction coefficient (uncoated beads)	μ	0.32
Mass of granular bed	m	300 – 900 g

Table 2.6. Dimensions of a mixer ($D/d = 50$) used in Section 5.2 of Chapter 5.

Dimension	Value (mm)
D_0	500
D_1	50
L	225
H_0	640
H_1	125
H_2	10

Chapter 3. Effect of the Number of Impeller Blades on Granular Flow in a Bladed Mixer

A cylindrical mixer agitated by an impeller blade is commonly used for liquid mixing, and it has been observed that the number of blades on the impeller can significantly affect mixing efficiency [58]. The effect of the number of blades on solids flow and mixing in a cylindrical mixer has not been studied in detail. We begin with studying the effect of impeller blade geometries/configurations on cohesionless granular flow behaviors and mixing kinetics by varying the number of the blades used in an agitated mixer via discrete element method. The particle bed in a bladed mixer consists of monodisperse, cohesionless spherical glass beads. A schematic of the four impeller blade configurations (1 blade, 2 blades, 3 blades, and 4 blades) used in our simulations is presented in Fig. 3.1. All of the blades are pitched at a 45-degree angle and have the same length (L) and, except for the 1 blade case, the blades are symmetrically placed about the vertical axis. In the simulations, the impeller blades were attached to a cylindrical shaft, and the shaft was placed at the center of the mixer. To study the effect of the number of impeller blades, we carried out DEM simulations using mixer dimensions and input parameters in Tables 2.1 and 2.2 of Chapter 2, respectively, and the blade configurations in Fig. 3.1. Velocity components of particles, kinetics of mixing, granular temperature, bulk density, blade-particle contact forces, and the normal contact force network in the systems were examined.

3.1 Velocity Fields and Velocity Frequency Distributions

Fig. 3.2 depicts time-averaged radial and vertical velocity fields in a vertical plane in front of a blade. The vertical plane goes from the wall to the center of the mixer and from the bottom of the container to the top of the granular bed. The length of vectors represents magnitude of the radial and vertical velocity components. The length of the marker arrow on the top left of each panel indicates the velocity magnitude equal to 0.02 m/s. The magnitude of the tangential velocity is represented by the colors of the vectors which point out of the plane of the graph for the obtuse blade pitch.

In a 1-bladed mixer (Fig. 3.2a), a strong three-dimensional (3D) recirculation pattern develops as particles close to the cylinder wall flow vertically upward forming heaps. Particles above the heap move radially inward to the impeller shaft, and particles by the shaft flow vertically downward and radially outward creating a pronounced 3D recirculation zone. A velocity field similar to that seen in the 1-blade system is also observed in the 2-blade case (Fig. 3.2b). In the 3-bladed (Fig. 3.2c) and 4-bladed (Fig. 3.2d) systems, the recirculation zones are still present but with smaller values of radial and vertical velocities, and thus the recirculation shows less prominent flow patterns compared to those in the 1-blade or 2-blade cases. A quantitative comparison of the radial and vertical velocity fields shows that these velocity components in front of the blades for the 1- and 2-bladed systems can at some points be as much as a factor of 2 times larger than the corresponding velocities for the 3- and 4-bladed systems. However, magnitudes of the tangential velocities of particles in the 3- and 4-bladed systems are higher than

those seen in the 1- and 2-bladed systems, which means that for 3 and 4 blades the particles are pushed in the tangential direction by the blades more strongly.

Frequency distributions of the instantaneous velocities of the particles within the whole particle bed were also analyzed. Fig. 3.3 shows the velocity frequency distributions for the tangential, radial, and vertical velocity components from simulations using different numbers of blades. The velocities presented in Fig. 3.3 have been normalized by the tip speed of the blades (V_{tip}). The tangential velocities shown are relative to the angular movement of the blades, i.e., $V_t^* = (V_{tip} - V_t)/V_{tip}$. As can be seen from Fig. 3.3, the tangential velocities (Figs. 3.3a, d, g, and j) have left-skewed distributions with all particles possessing velocities below the tip speed of the blades ($V_t^* > 0$). On one hand, the frequency distributions of particle tangential velocities for the 1- and 2-bladed mixers are non-symmetric with modes at zero. On the other hand, the frequency distributions of tangential velocities for 3- and 4-bladed systems are more symmetric, much closer to normal distributions, and have higher frequencies of the large tangential velocity magnitudes. These results are consistent with the interpretation from the velocity fields (Fig. 3.2). The shapes of the frequency distributions of radial velocities for different numbers of blades (Figs. 3.3b, e, h, and k) show distributions centered at zero, and their general shapes are similar with the highest frequency in a 1-bladed mixer. The vertical velocities for the 1-blade (Fig. 3.3c) and the 2-blade (Fig. 3.3f) cases have slightly right-skewed distributions with the mode values at zero; while, the vertical velocities for the 3-blade (Fig. 3.3i) and the 4-blade (Fig. 3.3l) cases show a more symmetric distribution centered at zero. The differences in the probability distribution functions of the velocity

components suggest that the number of impeller blades used in the mixing system has a strong effect on the granular flow velocities and the characteristics of the mixing behavior.

3.2 Blade-Particle Contact Forces and Force Frequency Distributions

Interparticle forces and the forces that the blades exert on particles play an important role in mixing and segregation of granular materials in an agitated mixer [94]. In addition to the investigation of particle velocities, we also analyzed the contact normal forces that the blades exerted on particles in the system. Similar to the velocity fields in Fig. 3.2, the time-averaged vector fields of the contact forces that the blades exert on particles are visualized in Fig. 3.4 for the four different blade configurations. The force fields are plotted in the vertical plane (Fig. 3.4) in an analogous way to the velocity fields (Fig. 3.2). The length of vectors represents magnitude of the radial (F_r) and vertical (F_y) components of the contact forces. The length of the marker arrow on the top left of each panel indicates the force magnitude equal to 0.05 N. The magnitude of the tangential component of the contact forces (F_t) is represented by the colors of the force vectors. In general, the force vector fields in Fig. 3.4 are similar to the flow patterns of the velocity vectors in Fig. 3.2 for all cases. We find that particle velocities in each direction correlates with each component of the contact forces that the blades exert on particles. The blade-particle radial and vertical forces in the 1-bladed (Fig. 3.4a) and 2-bladed (Fig. 3.4b) systems are larger than those in the 3-bladed (Fig. 3.4c) and 4-bladed (Fig. 3.4d) systems. However, the magnitudes of the tangential components of the blade-particle forces in the 3- and 4-bladed mixers are larger than those in the 1- and 2-bladed cases.

We propose a mechanistic explanation for this phenomenon that, due to the greater number of blades in the 3- and 4-bladed cases, the blades transfer more energy to the particles via the blade-particle forces leading to particles moving in the tangential direction more quickly than in the other cases. The larger blade-particle forces in the tangential direction lead to higher tangential velocities in the 3- and 4-bladed systems.

In addition to the probability distribution functions of the particle velocity components in Fig. 3.3, we analyzed the instantaneous contact forces that the blades exert on particles within the granular bed. Frequency distributions of the tangential (F_t), radial (F_r), and vertical (F_y) components of the contact forces for the four configurations of bladed mixers are presented in Fig. 3.5. In general, the shapes of frequency distributions of the contact force components are similar to the ones we observed for the velocity distributions (Fig. 3.3), except that the distributions of the forces are much narrower. For all blade configurations, distributions of the contact forces show high frequencies in only a few bins around the mode values and thus display narrow distribution curves.

Distributions of the tangential component of the contact forces have left-skewed shapes and are most frequent at approximately zero Newtons in the 1-bladed (Fig. 3.5a) and the 2-bladed (Fig. 3.5d) mixers. In contrast, the distributions in the 3-bladed (Fig. 3.5g) and 4-bladed (Fig. 3.5j) cases are closer to normal distributions, and the magnitudes of the tangential component of the force in the 3- and 4-bladed mixers are larger than those in the 1- and 2- bladed cases, which is consistent with the tangential velocity distributions (see Fig. 3.3). In the 2-bladed mixer (Fig. 3.5d), a larger magnitude of the tangential

component of the contact force can be seen compared to that in the 1-bladed mixer (Fig. 3.5a).

For the blade-particle radial and vertical forces, the force distributions are particularly narrow and centered around zero Newtons for all blade configurations (Figs. 3.5b–c for 1 blade, Figs. 3.5e–f for 2 blades, Figs. 3.5h–i for 3 blades, and Figs. 3.5k–l for 4 blades, respectively). A comparison of the frequency distributions of the blade-particle force components (Fig. 3.5) with the particle velocities (Fig. 3.3) shows that the velocities are related to the forces that the blades exert on particles in the granular bed. The tangential component of the blade-particle force is larger than the other components, and this is consistent with the larger tangential component for the particle velocities.

3.3 Normal Contact Force Network

In quasi-static flows, the main mechanism for momentum transfer comes from the formation of contact force chains [34]. A force chain is a network of interparticle contacts in which force is transmitted along the contact path. It has been shown that in static granular systems contact chains possess a characteristic length of a few particle diameters [95]. Fig. 3.6 depicts instantaneous normal contact force networks in the horizontal plane near top of the blades for our four simulation cases; the blades are moving in the counter-clockwise direction. In this figure, each line represents the contact vector connecting the center of the particles, and the thickness of the line represents the magnitude of the normal force associated with that contact. Higher forces are represented by thicker lines and vice versa. Two distinct regions in the normal contact force network obtained from

the 1-bladed mixing process are observed in Fig. 3.6a. The region in front of the blade is characterized by a number of thick lines showing high normal force magnitudes and high loads that particles in front of the blade carry. In contrast, there are very small contact forces presented in the region far away from the blades, which is represented by the large white area in Fig. 3.6a where there is almost no momentum transfer occurring in this region.

In the 2-blade case, two symmetrical sections of the normal contact force network can be seen in Fig. 3.6b. The regions in front of the blades are described by a higher number of interparticle contacts but lower magnitude forces than those in the 1-bladed case. Regions far away from the front of the leading blades still display some blank areas where there are very few contact force networks. For the 3-bladed system (Fig. 3.6c), the network is comprised of three symmetrical sections of contact chains, which is characterized by a large number of interparticle contacts. There are only small regions of white space associated with relatively small contact forces in the 3-bladed case. The normal contact force networks developed in the 4-bladed mixer (Fig. 3.6d) resemble the pattern found in the 3-bladed system, except for the fact that four symmetrical sections of the networks are observed and that there are even smaller regions of white space. Normal contact force network data shows that using different numbers of the impeller blades leads to significant differences in the force distribution within the particle bed.

3.4 Mixing Kinetics

We investigated the effect of the number of impeller blades on the degree of mixing by coloring particles on the left side (red) of a horizontal plane differently from the particles on the right side (yellow) prior to the blade movement. The particles have identical properties except for their color. We then observed the mixing pattern after the blade motion had begun. Fig. 3.7 displays snapshots of the top horizontal plane view for the four simulation cases using different numbers of impeller blades (1 blade through 4 blades, respectively) at different numbers of revolutions. In general, well-mixed zones are first observed by the wall of the cylindrical vessel while the areas around the impeller shaft remain unmixed for longer periods of time [23]. Enhanced mixing is obtained for the 2- and 3-bladed mixers when compared to the 1-blade or 4-blade cases at the same revolution of the blades. This mixing difference is observed as early as after 1 revolution. After 4 revolutions, the 2- and 3-bladed systems (Figs. 3.7b and c, respectively) are well mixed, and mixing is down to the particle-particle level. On the contrary, large unmixed regions still remain in the 1 blade case (Fig. 3.7a), and some unmixed areas near the shaft are still present in the 4-bladed system (Fig. 3.7d).

Furthermore, we performed statistical analysis on particle concentration for a particular color of particles. The differences in mixing performance between the four simulation cases are confirmed by calculation of the systems' relative standard deviation (RSD) values. At a specific time step, we calculated the RSD of the red particle concentration for the whole system. The RSD was computed from the Eq. (2.28) in Chapter 2. Fig. 3.8 displays RSD curves of the red particle concentrations as a function of the number of

blade revolutions for the four different numbers of blades cases. After 5 revolutions, the RSD value of the 1-bladed system is approximately 0.45 and the 4-bladed system is 0.37; whereas, the RSD value for the 3-bladed case is approximately 0.31 and the 2-bladed case is 0.29. The differences in the degree of mixing are still present after 10 revolutions.

The discrepancies in mixing kinetics for the different numbers of impeller blades are also observed by computing the Lacey index (M) of the granular system (see Eq. (2.29) in Chapter 2). The effect of using different numbers of impeller blades on the computed Lacey mixing index M of the granular systems is shown in Fig. 3.9. In Fig. 3.9, we plot the Lacey index of the red particle concentration as a function of the number of blade revolutions. After 1 revolution, little difference in the M values for each case is observed, except for the 1-blade case that has the lowest Lacey index indicating the poorest homogeneity of the mixture. As blades move, the Lacey indices in all cases increase with blade revolutions and start to flatten out after 6 revolutions. From these Lacey index curves, it is confirmed that 2- and 3-bladed mixers result in better mixing performance than 1- and 4-bladed systems. We will come back to the differences in mixing performance after we have investigated a number of other quantities of interest.

3.5 Granular Temperature

We next computed granular temperature, according to Eq. (2.19) in Chapter 2, for each simulation case that has a different number of the impeller blades in an agitated mixer. The control volume chosen for calculation of the granular temperature in this section is defined by a cube with a size of six particle diameters and centered at the coordinates of

height $H = 0.10$ m and of various radial positions r (0.05 to 0.15 m, as specified in Fig. 3.10). Fig. 3.10 shows the time-averaged granular temperature as a function of the radial position. In this figure, granular temperature curves obtained from the 2- and 3-bladed cases are generally higher than those from the 1- and 4-bladed systems, which suggests higher particle velocity fluctuations and less uniform particle flows in the 2- and 3-bladed cases. These results imply that using 2 or 3 impeller blades in a mixing process is able to provide better diffusive behavior of particles. Furthermore, granular temperatures for the 3- and 4-bladed mixers are gradually increasing with the radial position, which follows the trend observed by Remy et al. [23] studying DEM simulations of free flowing grains in a four-bladed mixer. They found that lower granular temperature existed near the impeller shaft at the center of a mixer and that granular temperature maximum was observed near the cylinder wall. However, for the 1- and 2-bladed systems, granular temperatures rapidly increase in the region near the shaft, then decrease slightly after $r > 0.067$ m, and remain steady until $r = 0.15$ m, which indicates that there is little temperature gradient in the region near the mixer wall.

3.6 Particle Diffusivities

We also gauged particle motion at the microscopic level by calculating particle diffusivities which describe the mass flux rate due to particles' random walk. Quantitative measurements of particle diffusion and convection for all four simulation cases varying the impeller blade number were followed by using Eqs. (2.20) to (2.22) in Chapter 2. Table 3.1 lists the normalized diffusion coefficients and the Péclet numbers in the tangential, radial, and vertical directions obtained from the different numbers of

blades cases. Particle diffusivities are the lowest for the 1-bladed system while these values are the highest for the 2- and 3-bladed cases as granular temperature and bed dilation are highest for these cases. $D_{\theta\theta}^*$, D_{rr}^* , and D_{yy}^* values for the 4-bladed mixer are lower than those values obtained from the 2- and 3-bladed cases but are higher than those from the 1-bladed system. Little difference in values of the normalized diffusion coefficients in all directions is observed between the 2-bladed case and the 3-bladed case. The Péclet numbers obtained from all cases studied using different numbers of blades are significantly higher than unity, which indicates that convection is the dominating mechanism for particle transfer. The convective process is most significant in the vertical direction (Pe_{yy}) since these values are larger than $Pe_{\theta\theta}$ and Pe_{rr} , except for the 4-bladed system where the Péclet number in the tangential direction ($Pe_{\theta\theta}$) is the largest one. This is probably due to the fact that the 4-bladed mixer has the greatest number of impeller blades resulting in the highest tangential velocity magnitude.

3.7 Bulk Density, Solids Fraction, and Void Fraction

In this section, we now look at the effect of the number of impeller blades used in a mixing process on the system's bulk density and compression/dilation states by evaluating the solids fraction and the void fraction of the granular beds (see Eqs. (2.23) to (2.25) in Chapter 2). Values of void fraction as a function of dimensionless radial position (r/R) for different numbers of blades are shown in Fig. 3.11a. Void fractions were computed within the particle bed by setting up spherical sampling bins at a height $H = 0.1$ m and various radial positions. The sampling bins had a diameter equal to 20 particle diameters, and averaging was carried out for 27 seconds. Void fractions in all

cases are generally increasing with the radial distance from the center to the wall of the mixer, except for the 3- and 4-bladed cases where the values of void fractions are decreasing in the regions near the mixer impeller shaft ($r/R < 0.5$). Additionally, void fraction values decrease with an increase in the number of impeller blades in the system at a particular dimensionless radial position, which suggests that spherical glass beads are densely packed in the cases of higher numbers of impeller blades. We hypothesize that, with an increase in the number of blades, the magnitudes of the forces transferred from the blades to the particles increase, which results in a more compressed granular beds and less void spaces.

To prove this hypothesis, the same sampling procedure as the one we used while calculating void fractions was adopted to determine contact forces between the blades and particles within spherical sampling bins. Fig. 3.11b shows the magnitude of the blade-particle forces as a function of dimensionless radial position (r/R) for the different numbers of blades. For the 1- and 2-bladed mixers, the magnitudes of the blade-particle forces decrease with an increase in radial position. For the 3- and 4-bladed mixers, the magnitudes of the blade-particle forces initially increase with r/R , go through a maximum and then decrease. All of the bladed mixers have a similar magnitude of the blade-particle force at $r/R = 0.35$ and $r/R = 0.93$. For a dimensionless radial distance between 0.5 and 0.9, the magnitudes of the blade-particle forces increase when increasing the number of impeller blades, which correlates inversely with the void fraction data in Fig. 3.11a. In general, there is very good agreement between the trends observed for the void fractions and the blade-particle forces although the trends are in the opposite direction. It is

therefore verified that the greater the number of the blades used in the mixing system, the larger is the magnitude of the blade-particle forces, which leads to greater compression of the granular bed.

One of the characteristics of dense granular materials is that dilation must occur to disrupt interlocking particle structures before particles can flow past one another. Moreover, it has been observed that a less densely packed state enhances mobility [7]. For our systems, we have observed that the blade-particle contact forces increase as the number of blades increases. The larger blade-particle contact forces correspond to lower voidage and higher tangential velocities and lower radial and vertical velocities. Thus, there are a number of competing factors that occur as the number of blades increases. The increased voidage means that the probability of a particle finding a void increases, and this has been shown to increase diffusion and convection [7]. At the same time, one would expect that larger tangential velocities would also increase convection. In terms of the mixing process, the optimal number of blades is two or three blades. We also observe that for the granular temperature and diffusion coefficients the optimal number of blades is two or three blades. Our results suggest that this optimum is due to a competition between increasing tangential velocities and decreasing voidage as the number of blades increases.

To further investigate the effect of the number of blades on compression of the bed, we have examined periodic variations of the packing state of the particles. Fig. 3.12 depicts the periodic behavior of the average solids fraction (ϕ) of the particle bed at a dimensionless radial position $r/R = 0.5$ and height $H = 0.1$ m when plotted as a function

of the number of blade revolutions for the four different numbers of impeller blades cases. Solids fractions were computed within the particle bed by setting up a spherical sampling bin with a diameter equal to 20 particle diameters at $H = 0.1$ m and $r/R = 0.5$. In this figure, the number of solids fraction oscillations per revolution correlates with the number of impeller blades. It can be seen that the solids fraction fluctuations for the different cases vary in amplitude. For the 1-bladed system (Fig. 3.12a), the main broad peak shows a range of solids fraction values between a minimum of approximately 0.3 and a maximum of ~ 0.6 . For the 2-bladed mixer (Fig. 3.12b), the solids fraction fluctuations exhibit the largest amplitude with a maximum value of ~ 0.6 and the lowest minimum value of ~ 0.2 . For the case using 3 blades (Fig. 3.12c), the maximum solids fraction value stays the same as that in the 1- or 2-bladed cases; however, the minimum value is slightly higher than that in the 2-bladed case. In the 4-bladed system (Fig. 3.12d), the solids fraction fluctuations display the smallest amplitude ranging from ~ 0.4 to ~ 0.6 . It is important to note that the maximum values of the solids fraction in all cases are almost the same and equal to ~ 0.6 while the minimum values are altered depending on how many impeller blades are used. This implies that changing the number of impeller blades in the system has no impact on the compressed state but influences the dilated state of the granular bed. It has been seen that the particle bed is dilated to the greatest extent for 2 impeller blades and to the least extent for 4 impeller blades. In order to achieve good mixing performance, not only does one need to effectively agitate the bed, but the bed also needs to be dilated to allow some available space for random movement of particles. It has been demonstrated that increasing the number of impeller blades beyond 2 blades does not provide better mixing performance to any appreciable extent.

In Fig. 3.13, the average solids fraction at a dimensionless radial position $r/R = 0.5$ is plotted as a function of the number of blade revolutions for different bed heights. In general, the solids fraction values in all cases at the bottom of the blender are close to 0.64 because the particles at the bottom carry the whole granular bed's weight and thus are densely packed. The solids fraction fluctuations above the top of the blades ($H > 0.05$ m) are similar to those shown in Fig. 3.12. For $H > 0.05$ m, the values of solids fraction and the amplitude of fluctuations decrease with an increase in bed height. The power spectrums corresponding to the results in Fig. 3.13 are shown in Fig. 3.14. The main peak height in the power spectrums shows that the amplitude of the fluctuations remains fairly constant within the region that spans the height of the blades. Above the blades, the mean values and amplitudes of solids fraction fluctuations change significantly. For the regions $H > 0.05$ m, the heights of the main peaks in the power spectrums in all cases decrease with an increase in bed height. The data on void fraction and solids fraction suggests that using different numbers of the impeller blades in a blender causes significant differences in the dilation state of a granular assembly and the efficiency of a mixing process.

3.8 Conclusions for Chapter 3

In this chapter, numerical simulations using the discrete element method were carried out to investigate the effect of the number of impeller blades on cohesionless granular flow in an industrially relevant geometry. It was found that particle velocities and movements in an agitated mixer were impacted by the number of the blades used in the mixing system. Although higher radial and vertical velocities of particles and more pronounced three-

dimensional recirculation patterns were observed in velocity fields obtained for the 1- and 2-bladed mixers, the tangential velocity components were larger in the 3- and 4-bladed cases. Differences in the frequency distributions of particle velocity components in an agitated mixer were also observed, which confirmed that the number of the impeller blades had a significant effect on the granular flow velocities. It was also found that the particle velocities in each direction correlated with each component of the blade-particle contact forces. The larger blade-particle forces in the tangential direction led to higher tangential velocities in the 3- and 4-bladed systems due to the greater number of impeller blades.

The number of impeller blades used in a blender was shown to significantly affect mixing kinetics of a granular system. It was demonstrated that using two or three blades in a blending process provided better mixing performance for a binary mixture of particles than using one blade or four blades, as evaluated by calculation of the relative standard deviation (RSD) and the Lacey index of the systems. Granular temperature and particle diffusivities in the 2- and 3-bladed mixers were also larger than those in the 1- and 4-bladed cases. Using different numbers of impeller blades in an agitated mixer influenced the extent of dilation of the particle bed, which yielded different degrees of mixing of the final mixture. Results for the void fraction and the solids fraction showed that dilation of the particle bed occurred to the greatest extent in the 2-bladed mixer. Normal contact force network data showed that using different numbers of the impeller blades led to significant differences in the force distribution within the particle bed. It was concluded that higher particle diffusivities and better mixing performances in the 2- and 3-bladed

mixers were resulted from the optimal balance between a large magnitude of the tangential component of the blade-particle contact forces and a great extent of dilation of the granular bed.

The results found in this chapter provide an insight into how the number of impeller blades affects granular flow in bladed mixers. These findings complement our preceding knowledge and grant better understanding with regard to the processing of particulate systems. At the same time these results are for a limited number of parameters, and further work is needed to confirm that the results of this study hold for other parameter values. Additional experimental data is also needed to confirm the results of this work. Further research is also needed to study the effect of other material properties and process parameters on flow and mixing operations in bladed mixers.

3.9 Figures for Chapter 3

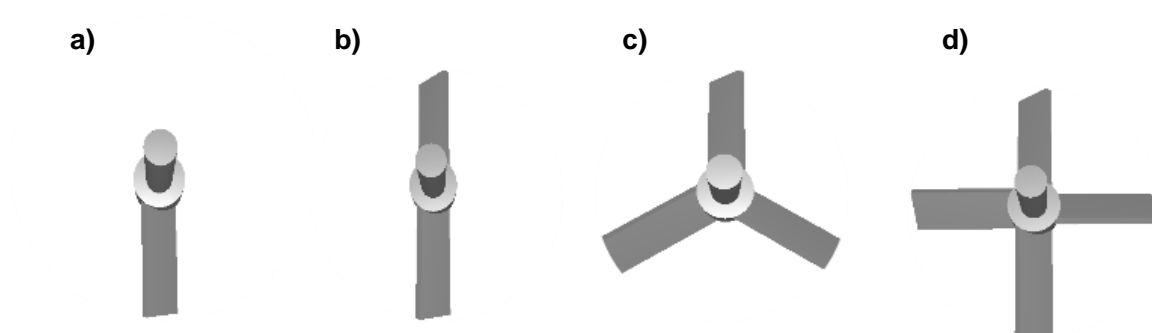


Fig. 3.1. Schematics of the four different impeller blade configurations: (a) 1 blade, (b) 2 blades, (c) 3 blades, and (d) 4 blades.

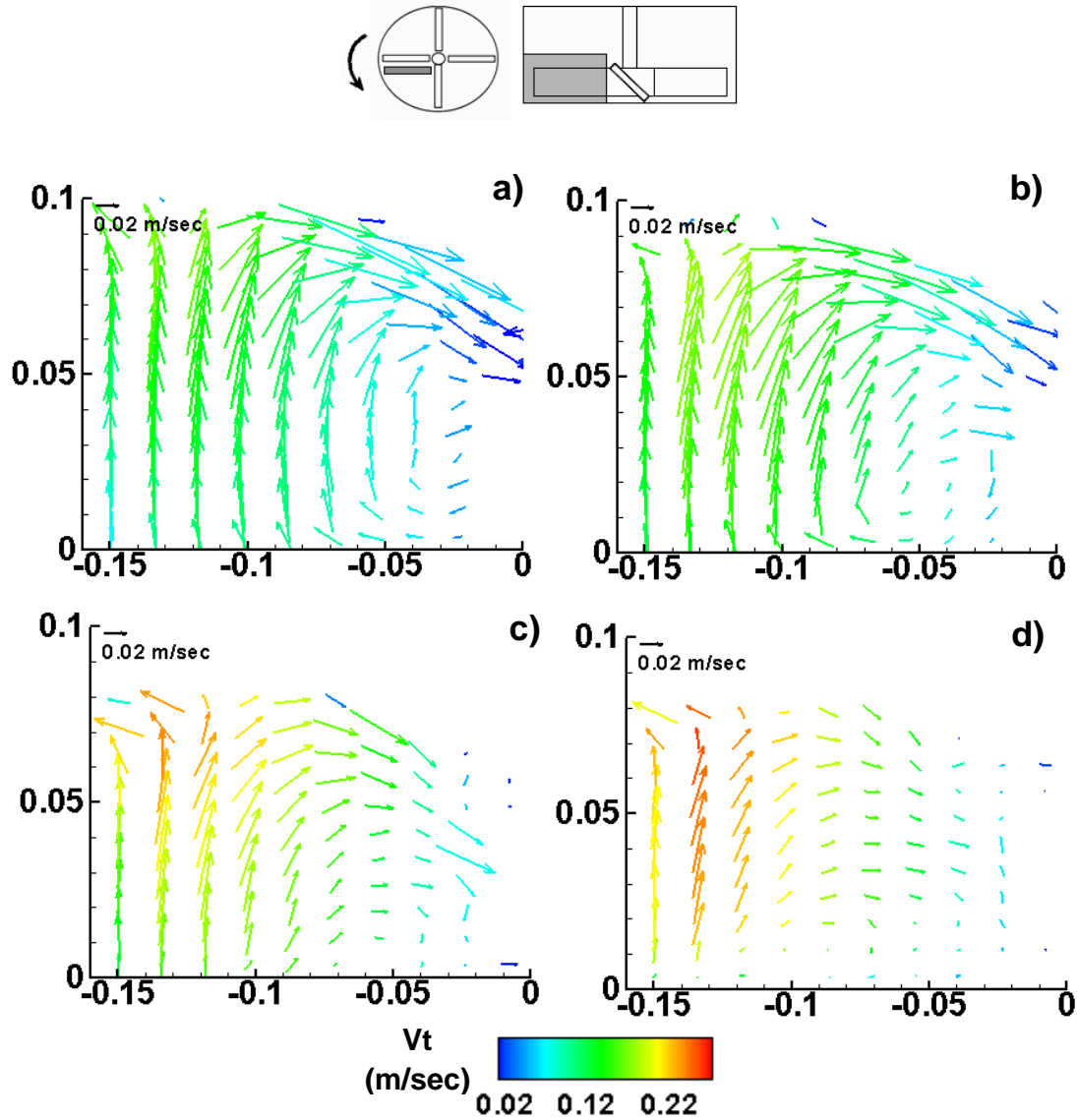


Fig. 3.2. Time-averaged radial (V_r) and vertical (V_y) velocity fields in a vertical plane in front of the blade for different numbers of blades: (a) 1 blade, (b) 2 blades, (c) 3 blades, and (d) 4 blades. The color bar indicates magnitude of the tangential velocity (V_t). The schematic at the top of the figure shows the position of the vertical plane for the 4-blade configuration. Analogous vertical planes are used for the other cases.

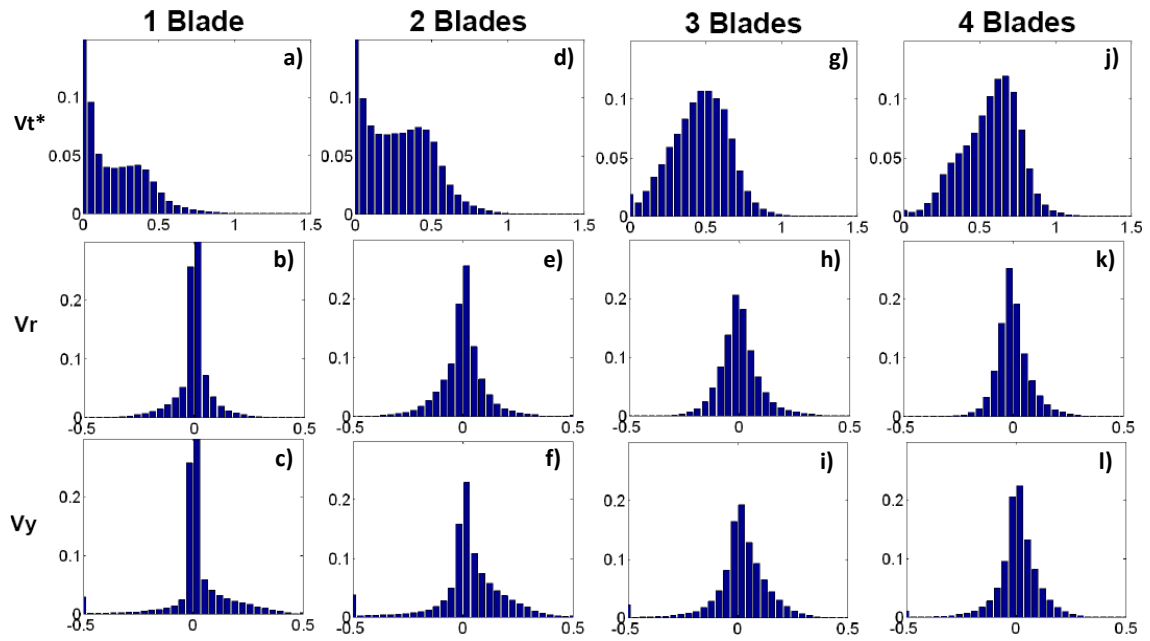


Fig. 3.3. Normalized velocity frequency distributions for the tangential (V_t^*), radial (V_r), and vertical (V_y) velocity components for different numbers of blades: (a)–(c) 1 blade, (d)–(f) 2 blades, (g)–(i) 3 blades, and (j)–(l) 4 blades. The velocity values shown here are relative to the tip speed of the blades.

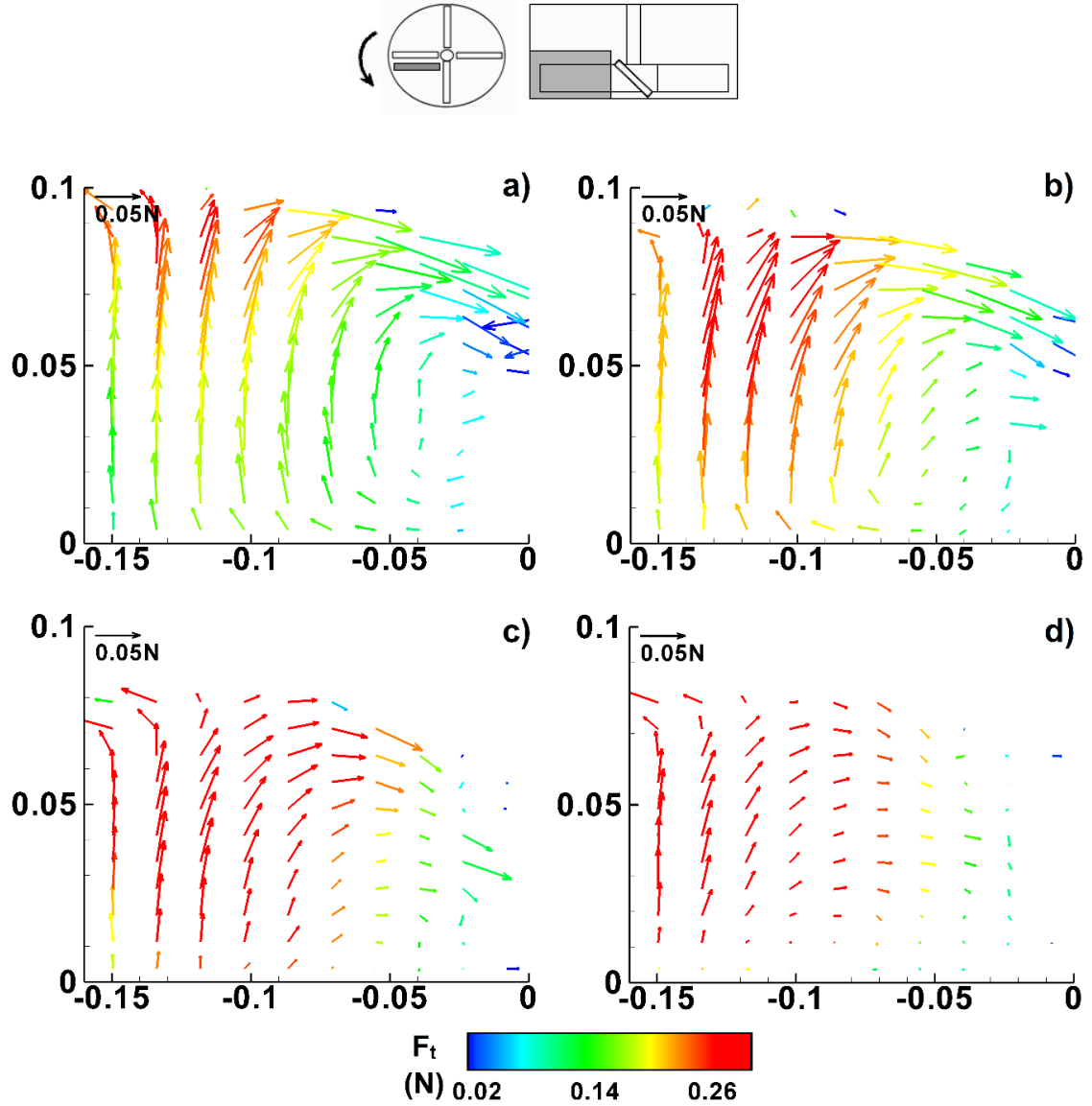


Fig. 3.4. Time-averaged vector fields of the radial (F_r) and vertical (F_y) components of the blade-particle contact forces in a vertical plane in front of the blade for different numbers of blades: (a) 1 blade, (b) 2 blades, (c) 3 blades, and (d) 4 blades. The color bar indicates magnitude of the tangential component of the contact force (F_t). The schematic at the top of the figure shows the position of the vertical plane for the 4-blade configuration. Analogous vertical planes are used for the other cases.

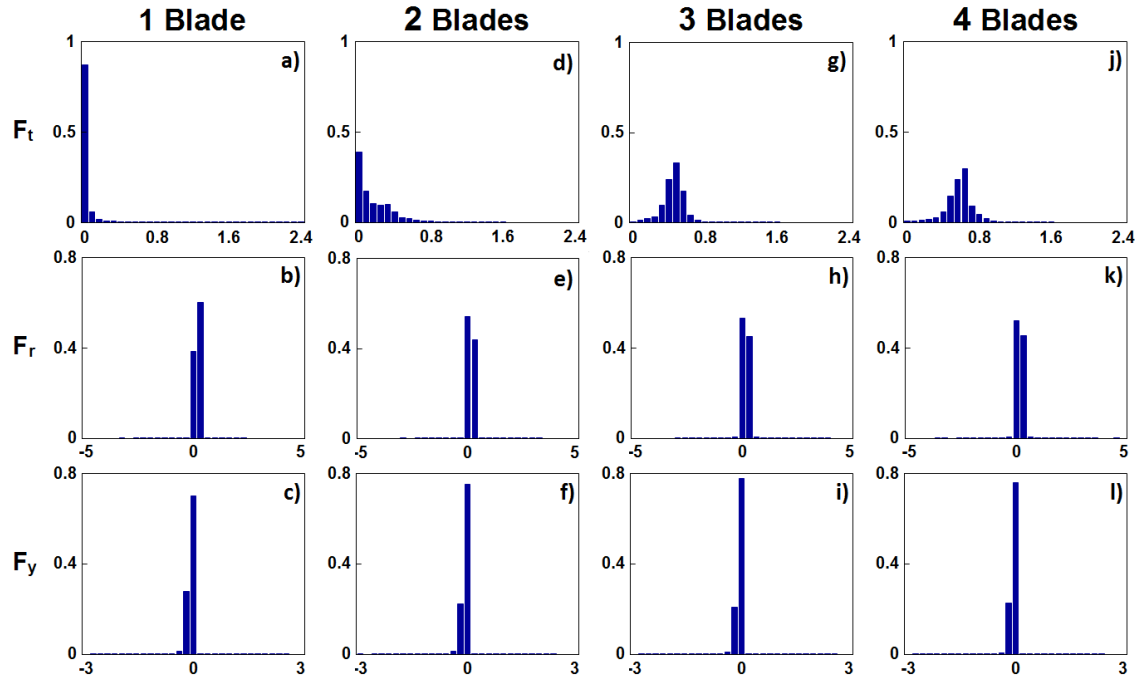


Fig. 3.5. Frequency distributions for the tangential (F_t), radial (F_r), and vertical (F_y) components of the blade-particle contact forces for different numbers of blades: (a)–(c) 1 blade, (d)–(f) 2 blades, (g)–(i) 3 blades, and (j)–(l) 4 blades.

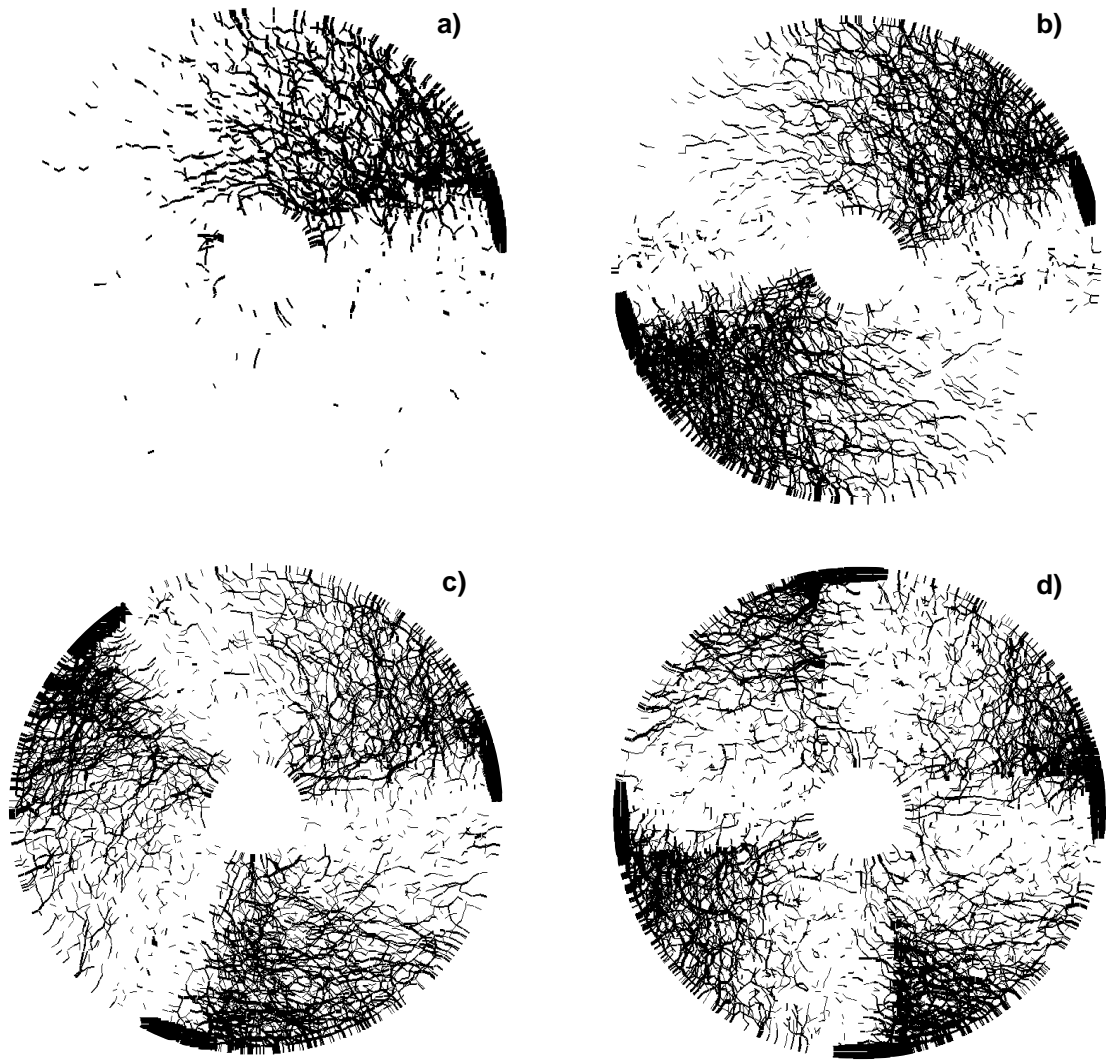


Fig. 3.6. Effect of the number of blades on the normal contact force network near top of the blades. (a) 1 blade, (b) 2 blades, (c) 3 blades, and (d) 4 blades.

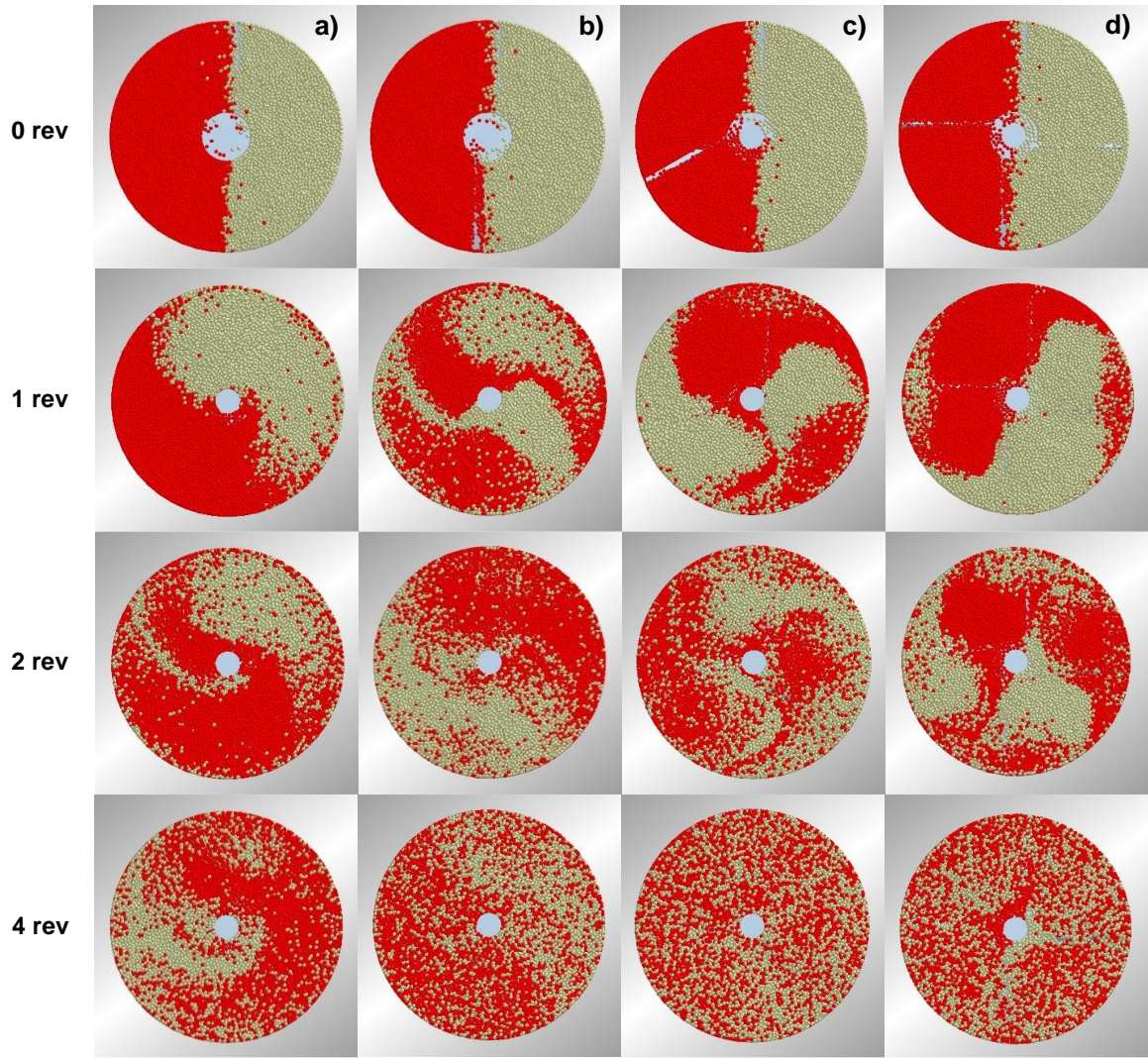


Fig. 3.7. Top view snapshots of the mixing process for the left-right segregated system at 20 RPM for different numbers of blades: (a) 1 blade, (b) 2 blades, (c) 3 blades, and (d) 4 blades.

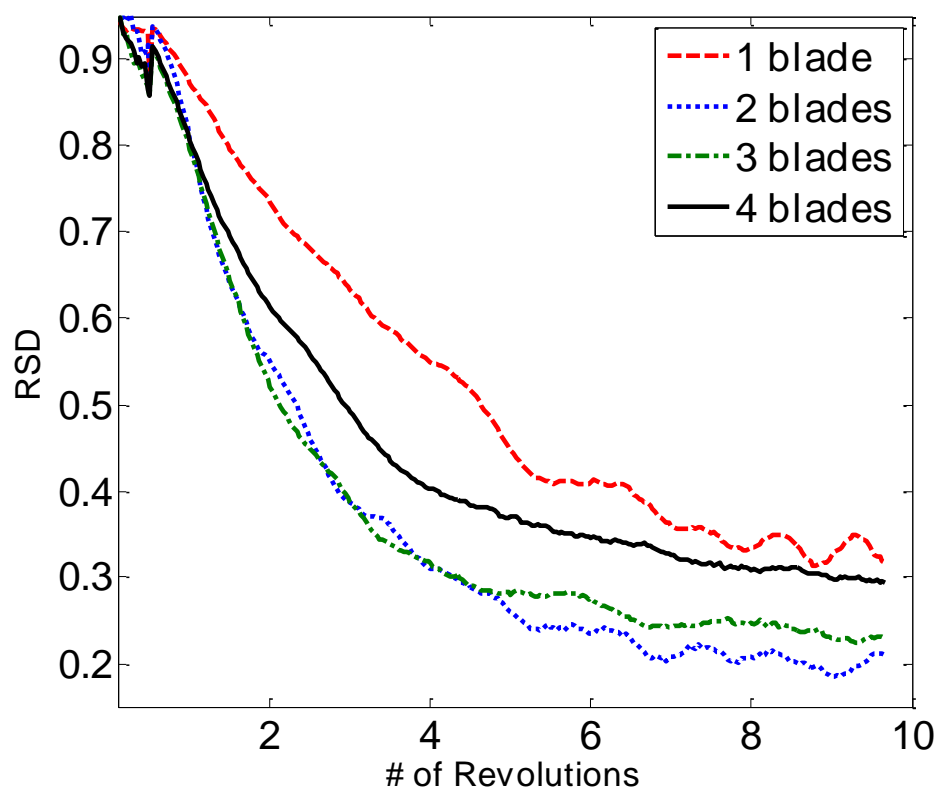


Fig. 3.8. Effect of the number of blades on mixing performance at 20 RPM. Relative standard deviation (RSD) of the red particle concentrations vs. number of revolutions of the blades.

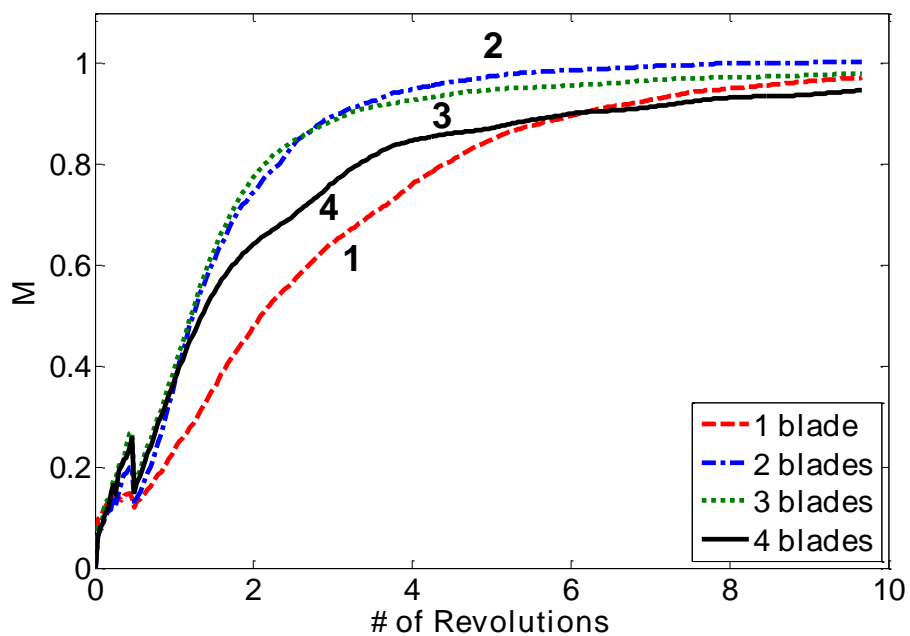


Fig. 3.9. Effect of the number of blades on degree of mixing at 20 RPM. Lacey index (M) of the red particle concentrations vs. number of revolutions of the blades.

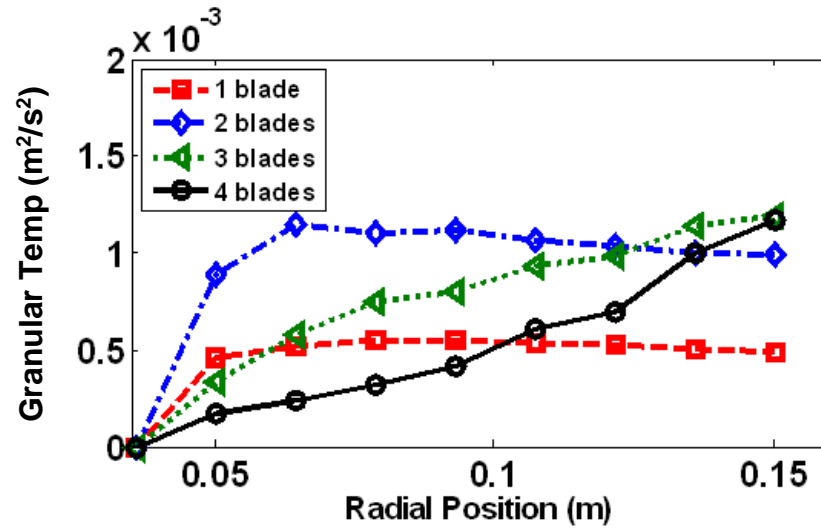


Fig. 3.10. Effect of the number of blades on time-averaged granular temperature as a function of the radial position.

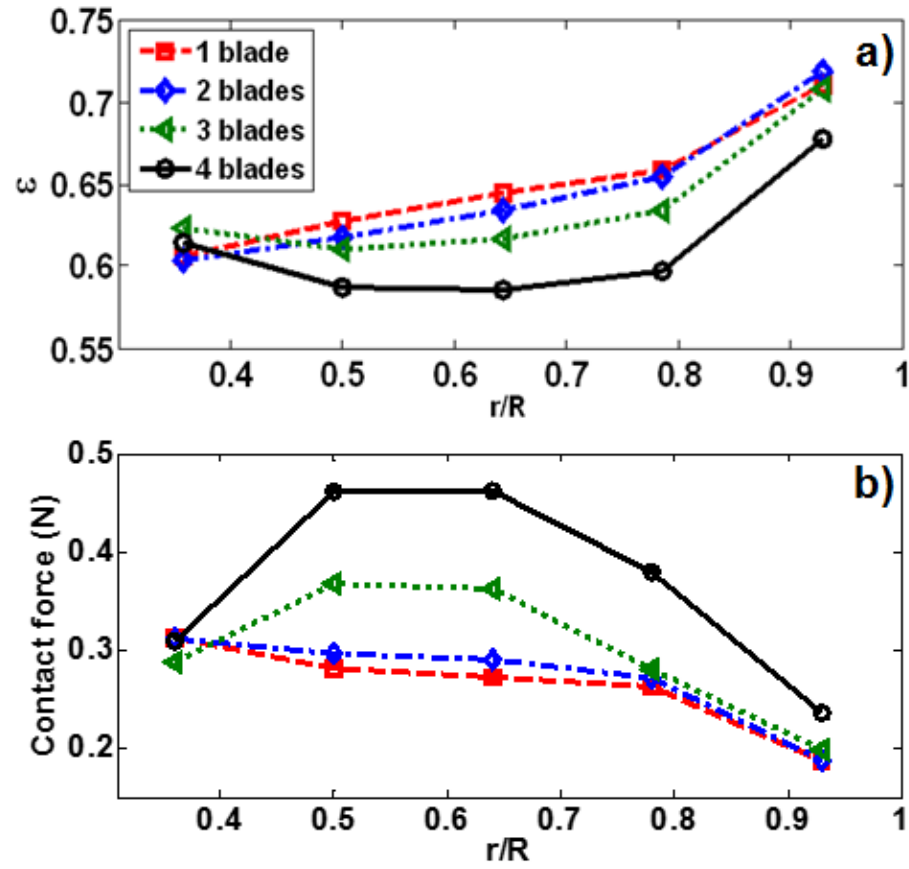


Fig. 3.11. Effect of the number of blades on (a) void fractions, ϵ and (b) magnitude of the blade-particle contact forces vs. dimensionless radial position (r/R) in a mixer. Both quantities were calculated by time-averaging using spherical sampling bins at a height $H = 0.1$ m.

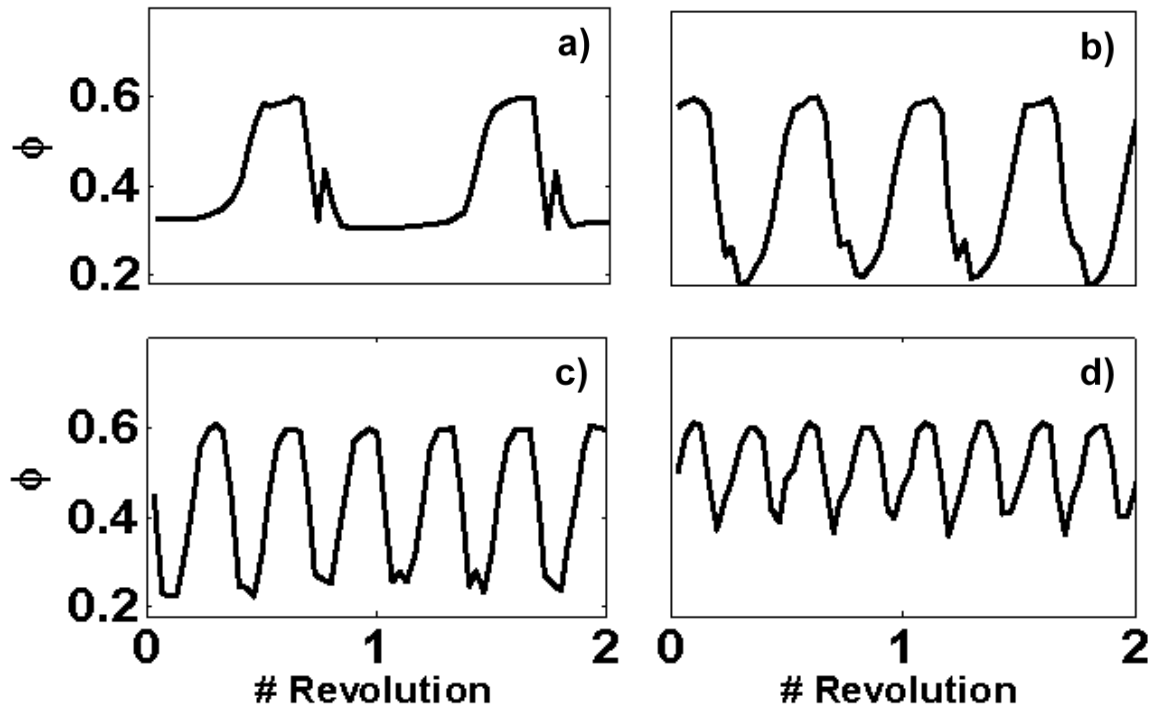


Fig. 3.12. Solids fraction (ϕ) vs. number of blade revolutions at the position $r/R = 0.5$ and $H = 0.1$ m for different numbers of blades: (a) 1 blade, (b) 2 blades, (c) 3 blades, and (d) 4 blades.

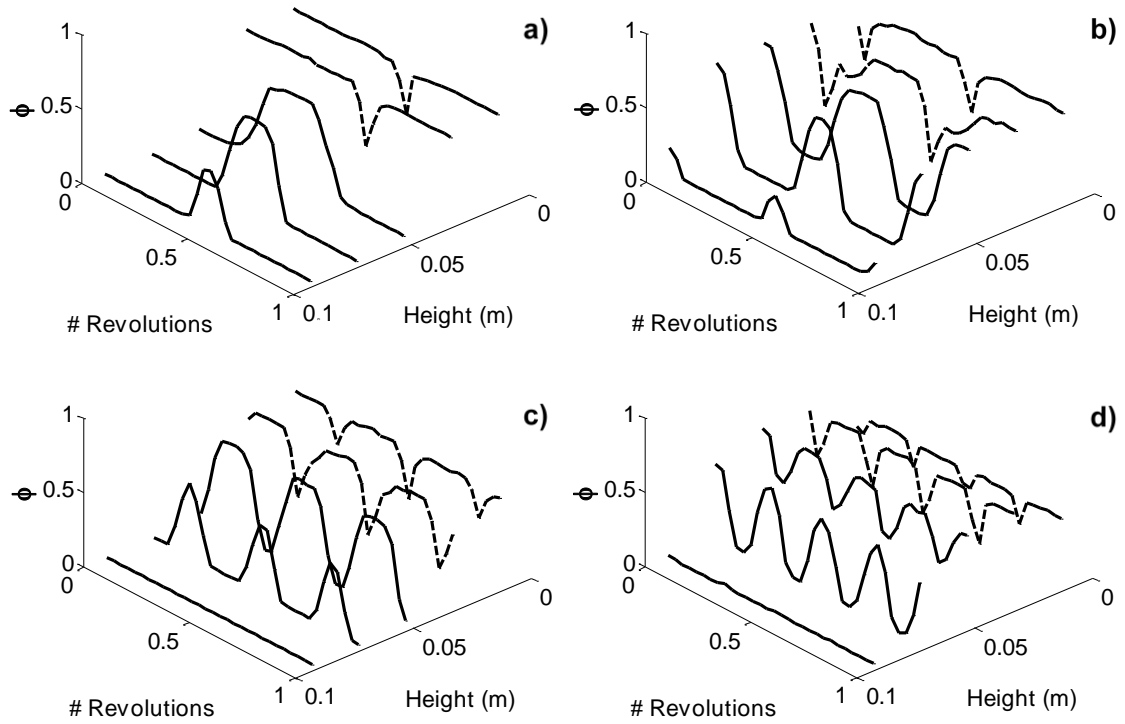


Fig. 3.13. Solids fraction (ϕ) vs. number of blade revolutions and heights at the position $r/R = 0.5$ for different numbers of blades: (a) 1 blade, (b) 2 blades, (c) 3 blades, and (d) 4 blades.

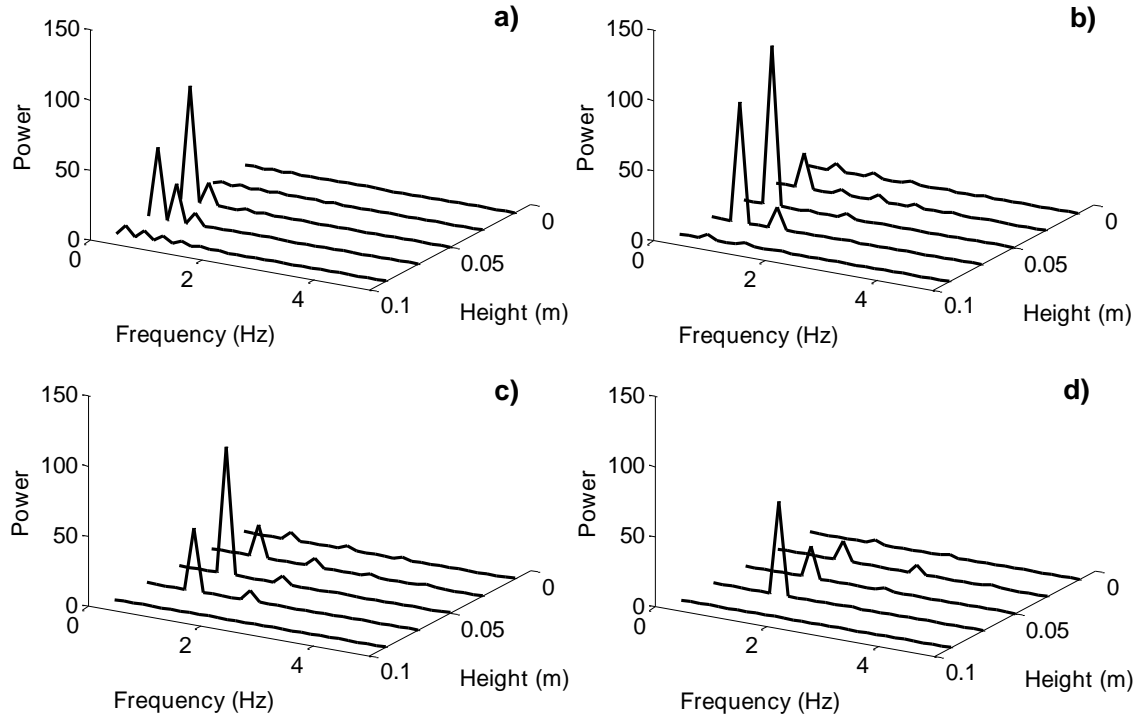


Fig. 3.14. Power spectrum of solids fraction (ϕ) at the position $r/R = 0.5$ for different numbers of blades: (a) 1 blade, (b) 2 blades, (c) 3 blades, and (d) 4 blades.

3.10 Table for Chapter 3

Table 3.1. Effect of the number of blades on normalized particle diffusivity (D_{ij}^*) and Péclet number (Pe_{ij}). Particle diffusivities were computed with a Δt of $\frac{1}{4}$ of a revolution and were averaged over all the particles in the computational domain.

Blade #	$D_{\theta\theta}^*$	D_{rr}^*	D_{yy}^*	$Pe_{\theta\theta}$	Pe_{rr}	Pe_{yy}
1	4.7×10^{-3}	1.1×10^{-3}	1.1×10^{-3}	29	39	85
2	1.2×10^{-2}	2.1×10^{-3}	2.5×10^{-3}	24	33	50
3	1.3×10^{-2}	2.1×10^{-3}	2.3×10^{-3}	35	32	44
4	1.0×10^{-2}	1.9×10^{-3}	1.7×10^{-3}	57	31	43

Chapter 4. Effect of Particle Properties and Process Parameters on Impeller Torque and Power Consumption: Experimental Investigations

In spite of some previous research in this area, the roles of material properties, blade and equipment configurations, and operating parameters on the impeller torque and power consumption in a batch mixer are still poorly understood. In this chapter, we studied a bed of particles in a batch bladed mixer consisting of a cylindrical glass vessel and a vertical impeller blade. Particle properties and impeller blade configurations of the mixing system were varied to investigate their effects on the experimentally measured torque that the impeller exerted on particles and on the power consumption that the motor drew to move the blades through the granular bed. The methodologies we used for the experimental measurements of torque and power were explained in detail in Section 2.2 Experimental Method of Chapter 2. This chapter is arranged in the following format. We will first present results for a base case, which is the flow of a shallow particle bed. This will be then followed by results for altering various material properties and equipment configurations for several impeller blade rotational rates. Also, a relationship for scaling torque and power measured in a deep granular bed will be proposed. We eventually conclude our study and suggest future work for this chapter.

4.1 Granular Flow in a Shallow Bed

In this section, we first consider granular flows in a shallow bed, which we will refer to as “the base case”. In our base case the 2-mm monodisperse, cohesionless, spherical, uncoated red glass beads were used. The amount of a granular material loaded in the

mixer was approximately 300 g, which was sufficient to cover just the top tip of the impeller blades, and the initial fill height of the stationary particle bed, H , was measured as 30 mm ($H/D = 0.30$). Experiments were performed in the bladed mixer with dimensions given in Table 2.4 of Chapter 2. The impeller (Fig. 2.2 in Chapter 2) used in experiments in this part consisted of 4 blades pitched at 135° angle with respect to a horizontal plane, and each blade had a length of 45 mm, which we will consider as “the standard impeller blades”.

4.1.1 Torque and Power Measurements

The protocol described in Section 2.2.3 of Chapter 2 was followed, and the torque signals were measured and recorded every second for experiments in this section. The time-averaged torque and the average adjusted power are plotted as a function of the dimensionless shear rate (γ^*) as shown in Fig. 4.1. The dimensionless shear rate (γ^*) is defined by the following equation according to Tardos et al. [33]:

$$\gamma^* = \gamma^\circ \sqrt{\frac{d}{g}} \quad (4.1)$$

where γ° is the shear rate (s^{-1}), d is the diameter of particles (m), and g is the gravitational acceleration (m/s^2). The shear rate (γ°) can be computed from the blade rotational speed (in RPM) by using the formula:

$$\gamma^\circ = \frac{2\pi \times \text{Rotational Speed}}{60} \quad (4.2)$$

In Fig. 4.1a, it can be seen that the average torque increases linearly with the blade rotational speed. One may expect that there would be two granular flow regimes as described by Tardos et al. [33]. The first one is the quasi-static or slow regime (γ^* is

smaller than ~ 0.1). The second regime is called the intermediate regime ($\gamma^* > \sim 0.1$). In the quasi-static regime one would expect the torque to be independent of rotation rate. We do not observe such a regime for a shallow particle bed ($H/D = 0.30$). We will come back to this point when we examine deep beds as in that case we do observe a quasi-static regime where torque is independent of shear rate. The trend of the linear increase in torque as a function of shear rate in the intermediate regime observed from experimental results in this section are qualitatively similar to numerical results from previous research studies using a discrete element method (DEM) computational technique done by Chandratilleke et al. [32] and Sato et al. [47].

Fig. 4.1b displays a graph of the average adjusted power plotted as a function of the dimensionless shear rate. The adjusted power (P^*) was obtained by subtracting the power consumed at a specific RPM with an empty cylinder from the power consumed by the impeller in the mixer loaded with particles. Similar to the torque graph in Fig. 3a, the average adjusted power linearly increases for the entire range of the dimensionless shear rate. In this research, it is assumed that the power needed to run the motor under load can easily be separated from the power needed to move the impeller by subtracting the power needed to run the motor when the mixer is not under load (i.e., when the mixer is empty and has no particles charged). However, this assumption might not be always true for all settings. Nevertheless, the power consumption measurement still provides useful information for pharmaceutical and other industries dealing with mixing processes, but care needs to be taken since recording power data is not as easily interpreted as measuring torque.

4.1.2 Fluctuation Analysis of Torque Data

The torque signals were measured and recorded every 0.125 seconds for all the experiments in this part. The instantaneous torque values (\vec{T}) measured at each time step were normalized by the time-averaged torque, $\langle \vec{T} \rangle$, at each blade rotational speed:

$$\vec{T}^* = \frac{\vec{T}}{\langle \vec{T} \rangle} \quad (4.3)$$

where \vec{T}^* is the dimensionless normalized torque at each time step. Fig. 4.2a – d display the normalized torque (\vec{T}^*) fluctuation profiles after the particulate systems have reached a steady state for different blade rotational speeds: 10 RPM, 20 RPM, 60 RPM, and 200 RPM, respectively. The time span shown in these graphs is 25 seconds and was sampled from the middle period of the experiments at steady state. The smallest fluctuation amplitudes can be seen in the case where the impeller blades rotate at 10 RPM (Fig. 4.2a). The torque fluctuation profiles for 10 RPM (Fig. 4.2a) are comparable in amplitude to those for 20 RPM and 60 RPM (Figs. 4.2b – c, respectively). As the shear rate increases in the intermediate regime of granular flow, i.e., increasing the blade rotational rate from 60 RPM (Fig. 4.2c) to 200 RPM (Fig. 4.2d), the fluctuation amplitudes increase. At 200 RPM (Fig. 4.2d), there is a noticeable recurrence of a periodic burst behavior of the torque fluctuations, indicating low and high values of torque which we conjecture are due to the expansion and compression states of the granular bed in the highest shear rate case of our experiments.

4.1.3 Fast Fourier Transform (FFT) of Torque Data

We also computed the discrete Fourier transform of the torque signals using the fast Fourier transform (FFT) algorithm in MATLAB® for the same blade rotation rates mentioned in Section 4.1.2. Torque data input for the FFT was measured and recorded every 0.125 seconds. Single-sided amplitude spectrums of the FFT torque data are depicted in Fig. 4.3 for various rotational speeds of the impeller blades corresponding to Fig. 4.2. As a check of the algorithm, we confirmed that the values of the 0-Hz components (the peaks at 0 Hz) always corresponded to the time-averaged torques for each blade rotation speed. Peaks corresponding to the impeller blade rotational rates (in RPM) can be observed (as circled for each RPM in Fig. 4.3), and the frequency (f) of each peak in Hz can be calculated by the following formula where the rotational speed is in RPM:

$$f = \frac{\text{Rotational Speed}}{60} \quad (4.4)$$

For example, the peak at frequency of 0.167 Hz can be seen in Fig. 4.3a for the impeller blades rotating with 10 RPM. The height of the blade frequency peaks increases with an increase in the rotational speed of the impeller blades. It is interesting to note that there are several overlapping peaks occurring between 2 – 3 Hz for all shear rates. We hypothesize that these peaks between 2 – 3 Hz are associated with natural frequencies of the moving granular material itself. It is also important to state that in all cases these peaks are higher in amplitude than the rotating blade frequency peaks.

4.2 Effect of Impeller Blade Configurations

A photo of the different types of the impeller blades used in our experiments is presented in Fig. 4.4. The black squares in this figure show an area of $1 \times 1 \text{ cm}^2$. Fig. 4.4a is what we referred to as “the standard impeller blades”, which was described in Section 2.2.1 of Chapter 2. In this part we explore the effects of the impeller configurations on the measured torque and power by changing the number, the angle, and the length of the blades using the impellers in Figs. 4.4b – f.

4.2.1 Effect of the Number of Impeller Blades

DEM simulations have been used by Boonkanokwong et al. [96] to study the effect of the number of impeller blades on granular flow behaviors and mixing kinetics in an agitated mixer. Different numbers of the blades in a mixer resulted in different impeller contact forces and particle velocity profiles, and thus, different mixing performance. The number of the blades used in a mixing system can also affect the impeller torque exerted on granular materials in a mixer and the equipment power consumption. This will be experimentally investigated further in this section. Experiments were carried out with different sets of impeller blades used in a mixer: 4 blades, 2 blades, and 1 blade as shown in Figs. 4.4a – c, respectively. All of these impeller blades are pitched at a 135° angle and have the same length (L) of 45 mm. The 2 and 4 blades are symmetrically placed about the vertical axis of the impeller shaft. All other particle parameters and operating conditions were the same as in the base case discussed in Section 4.1.

In Fig. 4.5a, the time-averaged torque for different blade numbers is plotted as a function of the dimensionless shear rate. The trends of how torque behaves as a function of the impeller blade rotational rate for the 1- and 2-bladed mixers are similar to that for the 4-bladed mixer (see Section 4.1.1). Interestingly, the average torque measured in the 2-bladed mixer is larger than that in the 4-bladed mixing system at all blade rotational speeds, and the value measured from the single-bladed mixer is significantly less than those of the 2 and 4 blades cases. The average adjusted power is presented in Fig. 4.5b, and it can be seen that the 1-bladed mixer has lower values than that of the 2- and 4-bladed mixers. In addition, the average adjusted power for the 2-bladed case is higher than the 4-bladed case which is in agreement with the torque measurements (see Fig. 4.5a). The trend of a linear increase of the adjusted power with an increase in the shear rate is observed for all numbers of blades used in this section. The fluctuations of both torque and power values (not shown) at each rotation rate in the 1-bladed mixer are generally higher than those in the 2- and 4-bladed cases because of asymmetry of the single blade when rotating through a granular bed.

4.2.2 Effect of the Impeller Blade Angle

We next explore the effect of varying the impeller blade angle on granular flow properties. For the standard impeller (Fig. 4.4a), blades are pitched at a 135° angle with respect to the horizontal plane. The angles of the blades used for the experiments in this section were altered to 90° (Fig. 4.4d) and 150° (Fig. 4.4e). The impellers were set to rotate in the counter-clockwise direction to provide obtuse blade angle configurations, which are commonly used in industries and considered to result in better mixing

performance than the acute angles [23]. All other particle parameters and operating conditions were the same as in the base case. Time-averaged torque and average adjusted power plotted as a function of the dimensionless shear rate are displayed in Fig. 4.6. From Fig. 4.6a, it can be seen that the blades with 90° angle have the highest average torque values, followed by 135° and 150° angles, respectively. In general, the torque values for the 135° and 150° cases are quite similar. In Fig. 4.6b, it is seen that the average adjusted power readings for the three different blade angle configurations are closer to one another than the torque values (see Fig. 4.6a). In general, the average torque and the adjusted power decrease with an increase in the impeller blade angle. Our experimental data is in good agreement with the DEM simulation results accomplished by Chandratilleke et al. [32], examining the effect of rake angle of the impeller on the shaft torque for cohesive particles in a vertical bladed mixer.

4.2.3 Effect of the Impeller Blade Length

We next investigate the effect of the length (L) of blades by using two different types of impeller configurations in our experiments: the 45-mm standard blades (Fig. 4.4a) and the 37.5-mm blades (Fig. 4.4f). Both impellers have four blades with a 135° angle. All other particle parameters and operating conditions were the same as in the base case. In Fig. 4.7a, it is noticed that when the time-averaged torque is plotted as a function of the dimensionless shear rate, torque values for both blade lengths increase fairly linearly with shear rate. In addition, the time-averaged torque of the 45-mm blades is significantly higher than that of the 37.5-mm blades for the entire range of impeller rotational rates. It can be observed in Fig. 4.7b that the average adjusted powers at low shear rates are not

obviously different for the two blade lengths. However, as the dimensionless shear rate increases, the average adjusted power is higher for the 45-mm standard blades than the 37.5-mm blades.

4.3 Effect of Particle Friction Coefficient

Remy et al. [27] experimentally and computationally studied the effect of varying roughness of particle surface on granular flow behaviors and mixing kinetics. They found that particle friction had a tremendous impact on particle velocity profiles and mixing patterns of granular materials in a bladed mixer. In this section, the effect of particle surface roughness on impeller torque and power will be investigated. The experiments were conducted for two sets of 2-mm glass beads; one was the standard uncoated red beads, and the other was the magnesium stearate (MgSt)-coated colorless beads fabricated according to a protocol in Section 2.2.4 of Chapter 2. The fill height of the particle bed for both cases was 30 mm ($H/D = 0.30$). The standard impeller blades (Fig. 4.4a) were used, and all other operating conditions were as in the base case. The results for the effect of roughness of the particles on the measured torque and adjusted power are shown in Fig. 4.8. It is observed in Fig. 4.8a that the MgSt-coated beads ($\mu = 0.38$, see Section 2.2.4) exhibit a distinctively higher average torque than the uncoated beads ($\mu = 0.32$, see Section 2.2.4). The reason for this is that the coated beads have a higher friction than the uncoated beads, and thus the impeller blades require more force to move through the particle bed. Also, the standard deviations of the torque values at each rotational rate are more for the MgSt-coated beads than those in the regular bead case as shown by the magnitude of the error bars in Fig. 4.8a. As shown in Fig. 4.8b, the average adjusted

power for the uncoated beads is noticeably less than that of the MgSt-coated beads for the entire range of the impeller blade rotational speed. These trends of torque and power consumption as a function of shear rate are similar to results for an experimental study performed by Remy [93] and DEM simulations carried out by Benque [97].

4.4 Effect of Impeller Blade Position in a Deep Granular Bed

Remy et al. [23, 24] demonstrated via DEM computational studies that granular flows in a shallow bed behaved differently from those in a deep particle bed. In this part, we will experimentally compare the measured agitation torque and the power consumption for shallow and deep beds. The granular material used in this section's experiments was 2-mm red colored glass beads, and the amount of material loaded into the laboratory mixer was increased from an initial bed height of 30 mm (as in the base case) to 90 mm. It should be noted that we observed in our experiments that when the blades are rotating the total height of the granular bed is approximately the same as the granular bed initial height at a stationary state. The particle bed with a 30-mm fill height ($H/D = 0.30$), i.e., the amount of glass beads just covering the top tip of the blades, was considered to be the shallow bed, and the particle bed with a 90-mm fill height was considered to be the deep bed. The H/D ratios in the deep bed are calculated from the height of the glass beads that cover and are above the span of the impeller blades, i.e., H is defined as the height from the bottom of the blades to the top of the granular bed. This was done as it had been shown previously that the material above the blades affected torque measurements [23, 24]. In order to investigate this impact, the blade position in a deep granular bed was changed from the bottom ($H/D = 0.90$) to the middle (where the blades are at 30-mm

height from bottom, $H/D = 0.60$) and to the top (where the blades are at 60-mm height from bottom, $H/D = 0.30$) in the mixer, compared to results in the shallow bed (30-mm fill height, $H/D = 0.30$). The standard impeller blades (Fig. 4.4a) were used, and all other process parameters in the experimental set-up were the same as those in the base case.

Comparison between the shallow and the deep granular beds for the measured torque and power plotted as a function of a dimensionless shear rate is shown in Fig. 4.9. From Fig. 4.9a, one can see that the time-averaged torque for the deep bed cases for $H/D = 0.60$ and 0.90 are considerably larger than that for $H/D = 0.30$. In addition, the deep and shallow bed cases for $H/D = 0.30$ agree fairly well. For the deep bed cases of $H/D = 0.60$ and 0.90 , we now see that for low shear rates there is a quasi-static region (for γ^* less than approximately 0.05) where the torque does not vary with shear rate. For the intermediate regime (γ^* larger than approximately 0.05), the torque values linearly increase as the blade rotational speed increases for all cases in the deep bed. Depicted in Fig. 4.9b, the average adjusted power for the deep bed increases with a relatively large slope as the impeller rotation rate increases; whereas, the power for the shallow bed increases with a relatively smaller slope as the blade rotational speed increases.

From Figs. 4.9a – b, it can be seen that the time-averaged torque as well as the average adjusted power for the blades at the bottom case ($H/D = 0.90$) are significantly larger than those for the cases in which the blades are at the middle position ($H/D = 0.60$) and at the top position ($H/D = 0.30$) in the deep granular bed, respectively. This is because as the amount of materials on top of the blades increases, the hydrostatic pressure applied on the

impeller increases, and thus, the resulting shear stress also increases correspondingly (see Eq. (4.6)). It can be observed that the average torque and the adjusted power results for the blades at the top position ($H/D = 0.30$) in the deep bed case are not significantly different from those for the shallow bed case (30-mm fill height in which particles are just covering the top tip of the blades with the impeller at the bottom of a mixer, $H/D = 0.30$). As was discussed, it has been shown in previous work [23, 24] that the materials underneath the impeller blades do not have any substantial influence on flow of grains in a mixing system since the only portion of a granular bed that moves is material within the span of the blades or close to the blades. The $H/D = 0.30$ case for the shallow and deep beds (see Fig. 4.9) are not identical; the small differences may be due to the fact that while the impeller at the top of a deep bed is rotating, the blades push some portion of the glass beads downward and cause some particles below to move which affects the agitation torque and power values.

4.5 Effect of Particle Size and Scaling Relationship

Particle size is one of the important material properties that plays a crucial role in granular flow and mixing. To understand the effect of particle size on power and torque exerted by an impeller blade on a granular material, three different particle sizes were examined in our experiments: 1-mm, 2-mm, and 5-mm diameter glass beads. All experiments in this section were performed using the standard impeller blades (Fig. 4.4a), and the fill height of the particle bed was kept constant to be 30 mm ($H/D = 0.30$) for all particle size cases. In addition, all other parameters and processing conditions were set to those in the base case.

In previous sections, the average torque and power values were plotted as a function of the dimensionless shear rate (γ^*). However, when plotting in this manner, the data points for different bead sizes do not lie on the same x -axis scale, making it more difficult to interpret the results. This is because the dimensionless shear rate (γ^*) is a function of particle size itself (see Eq. (4.1)). Therefore, in order to fit data points on the same x -axis scale, for this section only the time-averaged torque, as well as the average adjusted power, are plotted as a function of the shear rate (γ°), as shown in Fig. 4.10. In Fig. 4.10a, the average torque measured for the 5-mm diameter particles is the highest, followed by the values for 2-mm and 1-mm beads, respectively. A trend of linearly increasing torque values as the blade rotational rate increases can be observed for the 1-mm particles, similar to the 2-mm case (the base case in Fig. 4.1). At low shear rates ($\gamma^\circ < 4 \text{ s}^{-1}$) fairly constant torques are observed for the 5-mm beads indicating a quasi-static regime, and for higher shear rates there are linearly increasing torque values (indicating an intermediate regime) as the shear rate (or the blade rotational rate) increases. Similar trends are generally observed for the adjusted power graph in Fig. 4.10b, but the values linearly increase with shear rate for all particle sizes.

Jop et al. [98] and Andreotti et al. [99] have observed that granular flows can be characterized by a dimensionless inertial number which is proportional to the particle diameter, d , so it is possible that we may be able to scale the agitation torque by the particle diameter and have the results collapse on top of another. In addition, the power consumption of the motor can also be related to the torque, and thus, we expect that we

may also be able to scale the power consumption by the diameter of particles. In Fig. 4.11, we normalize the time-averaged torque and the average adjusted power values in Fig. 4.10 by the particle diameter for the three different cases of 1-mm, 2-mm, and 5-mm glass beads. It can be observed from Fig. 4.11a that the 1-mm particles have the highest normalized torque, $\langle T \rangle / d$. It is interesting to note that, although the actual time-averaged torque increases with an increase in a particle diameter (see Fig. 4.10a), the normalized torque values, $\langle T \rangle / d$, for the 2-mm and 5-mm particles are lower than that of the 1-mm particles. Moreover, the normalized torque $\langle T \rangle / d$ values for the 2-mm and 5-mm particles are fairly similar, implying that the torque exerted by the impeller on the granular material flowing in our bladed mixer complies with this theoretical scaling. Discrepancy of the normalized torque values, $\langle T \rangle / d$, for the 1-mm particles from the other cases might be due to the relatively wide particle size distribution of the 1-mm glass beads (see Section 2.2.2 in Chapter 2) and electrostatic charges that could extensively affect flow behaviors of the 1-mm beads. Similar trends are observed in Fig. 4.11b for the average adjusted power normalized by the particle diameter, (P^*/d) , as a function of the shear rate.

4.6 Effect of Material Fill Height and Scale-up

Barczi et al. [100] studied the effect of the granular bed depth on particle flow and homogenization in a vertical bladed mixer with two flat blades using the DEM technique. They observed that both macroscopic and microscopic flow patterns were affected by the packed-bed depth and the blade rotational rate. Remy et al. [24] carried out DEM simulations of bladed mixers at different scales and found that the total weight of the

particle bed in a bladed mixer was an important parameter affecting stress profiles and granular flow behaviors. In this part, we will examine the effect of the amount of granular material, reported as the fill height in the mixer, on measured torque and power. To do so, 5-mm glass beads and a lead weight were used in the experiments in this section to imitate the hydrostatic pressure experienced by the impeller blades. A circular lead weight was placed on a circular-cut piece of cardboard which was inserted through the impeller shaft assembly. The lead weight and the cardboard sat on top of the glass beads and distributed the normal load onto the particle bed during agitation to mimic the hydrostatic pressure experienced in the mixer. The experiments were carried out for the following different initial fill heights of beads: 30 mm ($H/D = 0.30$), 60 mm ($H/D = 0.60$), and 85 mm ($H/D = 0.85$). It was determined that mass of the lead weight (530 g) was equivalent to the mass of a particle bed fill height of 44 mm. This information was used to increase the fill height without actually using glass beads. For the 85-mm fill height, we performed two different sets of experiments. One scenario was using the beads actually filled up to 85 mm ($H/D = 0.85$), and the other setting was using the glass beads filled up to 41 mm plus the lead weight (equivalent to 44 mm) on top (which we referred to as “Effective $H/D = 0.85$ ”). For the “Effective $H/D = 1.04$ ”, we placed the lead weight on top of the 60-mm fill height of the beads. It should be noted that the particle size of the beads used in these experiments was 5 mm. This was different from the other cases because the 2-mm particles were smaller than the hole through which the lead weight was inserted onto the impeller shaft. Because of this, the 2-mm beads would escape upward through this hole and get on top of the lead weight, making the lead weight sink into the particle bed. Therefore, in order to overcome this problem, glass beads with a 5-mm

particle size were used instead in the experiments in this section. All experiments in this part were performed using the standard impeller blades (Fig. 4.4a). Additionally, all other process parameters were the same as those in the base case.

Fig. 4.12 shows the time-averaged torque and the average adjusted power results for cases with different fill heights of the glass beads as a function of the dimensionless shear rate. It can be observed from Fig. 4.12a that the shallow bed ($H/D = 0.30$) of 5-mm beads exerts the lowest normal load on the impeller blades, and thus the lowest values of torque are measured. As the amount of material in the bladed mixer increases, the experimentally measured torque generally increases with the fill height of the beads. The glass beads filled up to the 85-mm fill height ($H/D = 0.85$) yields comparable results to the case where the lead weight was placed on top of the material (Effective $H/D = 0.85$), implying that the lead weight can be a good representative of the normal load applied on the granular bed. In general, for the 104-mm fill height (Effective $H/D = 1.04$), the largest torque values are measured due to the largest amount of hydrostatic pressure experienced by the impeller blades during agitation. Similar trends for the average adjusted power in the shallow bed granular system ($H/D = 0.30$) plotted as a function of the dimensionless shear rate can be seen in Fig. 4.12b.

A scale-up relationship for deep granular beds varying the material fill height in a bladed mixer can be then developed from the average torque and adjusted power information. From Eq. (2.34) in Chapter 2, it can be rearranged to the following expression:

$$\vec{T} = 2\pi R_{\text{cyl}}^2 H \langle \tau_{\theta r} \rangle \quad (4.5)$$

Note that the impeller torque (\vec{T}) is proportional to the average shear stress $\langle\tau_{\theta r}\rangle$ multiplied by the height (H) of the particle bed when the blades are rotating. In addition, Remy et al. [24, 26] found that, for non-cohesive materials, Coulomb's law of friction was observed and the shear stress was proportional to the normal stress. Thus in a bladed mixer the average shear stress $\langle\tau_{\theta r}\rangle$ could be related to the hydrostatic pressure acting on the material:

$$\langle\tau_{\theta r}\rangle = \mu\rho_{\text{bulk}}gH \quad (4.6)$$

where μ is the bulk friction coefficient, ρ_{bulk} is the bulk density of the granular bed, g is the acceleration due to gravity, and H is the fill height of the bed. It will be assumed that changes in the granular bed bulk density ρ_{bulk} during agitation are negligible, i.e., ρ_{bulk} is approximately constant within the flow regimes we are investigating. This implies that the height, H of the granular bed does not change with rotation rate. We indeed observed in our experiments that when the blades are rotating the total height of the granular bed is approximately the same as the granular bed initial height at a stationary state. Substituting Eq. (4.6) into Eq. (4.5), the following relationship is derived subsequently:

$$\vec{T} = 2\pi\mu\rho_{\text{bulk}}gR_{\text{cyl}}^2H^2 \quad (4.7)$$

Expression (4.7) implies that the measured impeller torque scales by the square of the material fill height ($\vec{T} \propto H^2$) in a bladed mixer when all other parameters are constant.

In Fig. 4.13, we normalize the experimentally measured time-averaged torque $\langle\vec{T}\rangle$ and the average adjusted power P^* values in Fig. 4.12 by the square of the granular bed fill height (H^2) for each case. The normalized torque $\langle T \rangle / H^2$ results shown in Fig. 4.13a illustrate that all of the normalized torque data points for the deep particle beds ($H/D \geq 0.60$)

essentially collapse into one single curve. It is interesting to note that, even though the actual time-averaged torque increases with an increase in the material fill height (see Fig. 4.12a), the normalized torque $\langle T \rangle / H^2$ for all deep granular bed cases ($H/D \geq 0.60$) is lower than that of the shallow bed case ($H/D = 0.30$). Moreover, the fact that the normalized torque $\langle T \rangle / H^2$ values for the deep particle beds ($H/D \geq 0.60$) collapse into one single curve, with the exclusion of the shallow bed case ($H/D = 0.30$), implies that the impeller torque exerted on deep granular beds behaves differently from that in a shallow bed. We hypothesize this difference in the shallow bed case is because particles on the surface of the shallow bed can form heaps and valleys freely when the impeller blades are rotating, resulting in significant changes in the bed height and the bulk density especially at high shear rates which can in turn affect the torque scaling relationship in Eq. (4.7). An analogous principle can be applied to the impeller blade power consumption, and the normalized adjusted power P^* / H^2 results are depicted in Fig. 4.13b. Similar trends are observed for the normalized adjusted power P^* / H^2 both in the shallow and deep particle bed cases for the entire range of the granular flow regime.

4.7 Effect of Moisture Content

Last but not least, we examined the effect of cohesion due to moisture in granular systems on the agitation torque and power consumption. Remy et al. [29] computationally and experimentally demonstrated that particle flows and mixing performance in cohesionless system differed from those in cohesive granular systems and that different levels of moisture content in the systems resulted in different behaviors. In our experiments, water was incorporated into the particle bed according to the protocol

described in Section 2.2.5 of Chapter 2. Wet experiments were performed using the standard impeller blades and the colorless glass beads with a diameter of 2 mm loaded to a 30-mm fill height ($H/D = 0.30$). Moisture content added in cohesive granular systems was varied from 1% to 2.4% and 4.5% v/v, and the measured torque and power in cohesive systems were compared to those in non-cohesive system.

Fig. 4.14 shows the effect of the moisture content in granular systems on the impeller torque and power draw as a function of the dimensionless shear rate. In Fig. 4.14a, the averaged torque values measured in wet granular materials are qualitatively greater than that in cohesionless system. However, the torque values in the three different levels of moisture content cannot be obviously distinguished from each other due to high variations of the data. High deviation and less reproducibility of the torque results in cohesive granular systems are because of formation of agglomerates and sticking of particles to the mixer wall and impeller blades. Similar trends for the average adjusted power in cohesive granular systems varying moisture content levels can be observed in Fig. 4.14b but lot less deviations of the results compared to the torque variations. Further work on the measurements of the agitation torque and power consumption for cohesive granular materials in deep beds (higher H/D ratios) is needed to reduce variations and to obtain more reproducible results.

4.8 Conclusions for Chapter 4

Experiments were performed on monodisperse spherical glass beads flowing in a cylindrical bladed mixer agitated by an impeller. Experimental measurements of the

torque exerted by the impeller blades on the granular bed were achieved by using a torque table and a data acquisition system. Power consumed by the motor to move an agitator through the particle bed was also experimentally measured using a power meter. The effects of various impeller blade design configurations and material properties on the agitation torque and power were examined as a function of the impeller blade rotational speed. For “the base case”, which was composed of 2-mm diameter glass beads filled up to a 30-mm height ($H/D = 0.30$) that just covered the span of the blades and considered as a shallow bed using “the standard impeller blades”, the time-averaged torque values at low shear rates were slightly increasing within the quasi-static regime of granular flow behaviors. This was then followed by a linear increase in the torque in the intermediate region as the shear rate increased. This trend for the impeller torque was similar to what was observed for the adjusted power consumption. Data analysis in “the base case” revealed that fluctuation of torque values was fairly constant in the quasi-static region and increased with an increasing blade rotational speed in the intermediate flow regime. FFT spectrums for “the base case” showed peaks at frequencies corresponding to the impeller blade rotational rates.

This research demonstrates that the torque values and the power readings measured from the mixing system were sensitive to several factors including the impeller blade configurations (number, angle, and length of blades), the particle size and friction coefficient, the blade position in a deep granular bed, and the fill height of the glass beads. The time-averaged torque was dependent on the number of impeller blades used in the mixer; the 2- and 4-bladed mixers exerted greater torque than the 1-bladed mixer on

the particle bed due to the larger blade-particle tangential forces. The torque values also increased with an increase in the blade length and with a decrease in the blade pitch angle. Furthermore, at higher fill heights of the granular material, greater torque values and power readings could be measured. The highest torque and power measurements were recorded for the case where the impeller blades were placed at the most bottom position ($H/D = 0.90$) of the deep particle bed. This was because of the hydrostatic pressure from the material on top of the blades. Moreover, the average torque and adjusted power were a strong function of material properties including particle diameter and surface roughness. Larger particle sizes and a greater friction coefficient resulted in higher magnitudes of the torque and power. In addition, the time-averaged torque and power consumption for the 2- and 5-mm bead cases qualitatively scaled with particle diameter.

It was demonstrated that granular flow behaviors in a shallow bed were different from those in the deep bed. As the amount of material in the bladed mixer increased, the experimentally measured torque also increased. In the deep particle bed, the measured torque was independent of the shear rate in a quasi-static regime and then linearly increased as the blade rotational speed increased in the intermediate regime. Moreover, the clear distinction between these two regions could be observed in the deep granular bed, which could not be obviously differentiated in the shallow bed case. A scale-up relationship for deep granular beds varying the material fill height in a bladed mixer was then developed from the average torque and adjusted power information. The time-

averaged torque and average adjusted power consumption qualitatively scaled with square of the material fill height in a deep granular bed.

The results from research work in this chapter provide an insight on how the impeller blade configurations and material properties affect the agitation torque and power measured as a function of a process parameter in granular systems flowing in a bladed mixer. These findings complement our preceding knowledge and provide better understanding with regard to processing of solid particulate systems. At the same time these results are for a limited number of parameters, and future work is needed to validate that the results of this study hold for other parameter values. Further research should be conducted to study the effect of other material properties (e.g. cohesive particles), equipment configurations (e.g. different types of mixers), and other process parameters on particulate flow and mixing in a bladed mixer. Experiments can be done by adding and varying the amount of water in a granular bed to investigate the effect of cohesion on measured torque and power consumed by the impeller blades. In addition, results of the parametric sensitivity analysis for the impeller blade torque and power consumption found in this research can be extended further by performing experiments in larger scale mixers. DEM simulations in a similar geometry can also be carried out by varying the aforementioned factors to provide information about torque and power.

4.9 Figures for Chapter 4

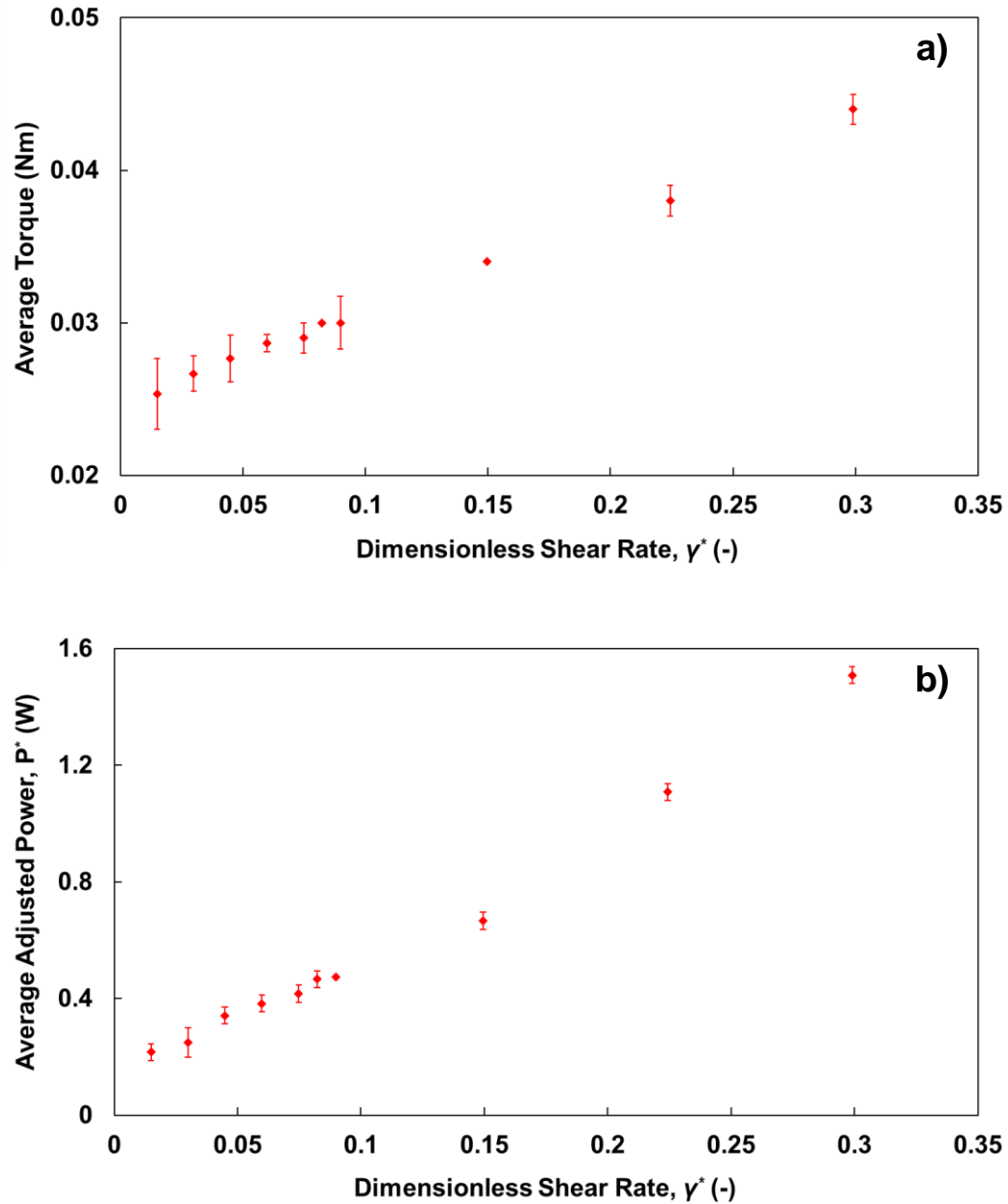


Fig. 4.1. Granular flow properties as a function of the dimensionless shear rate (γ^*) for “the standard case”: (a) the time-averaged impeller torque and (b) the average adjusted power (P^*). The experiments were performed using red glass beads of 2-mm diameter loaded to a 30-mm fill height (shallow bed, $H/D = 0.30$) and the standard impeller blades (4 blades with a 135° angle and 45-mm length).

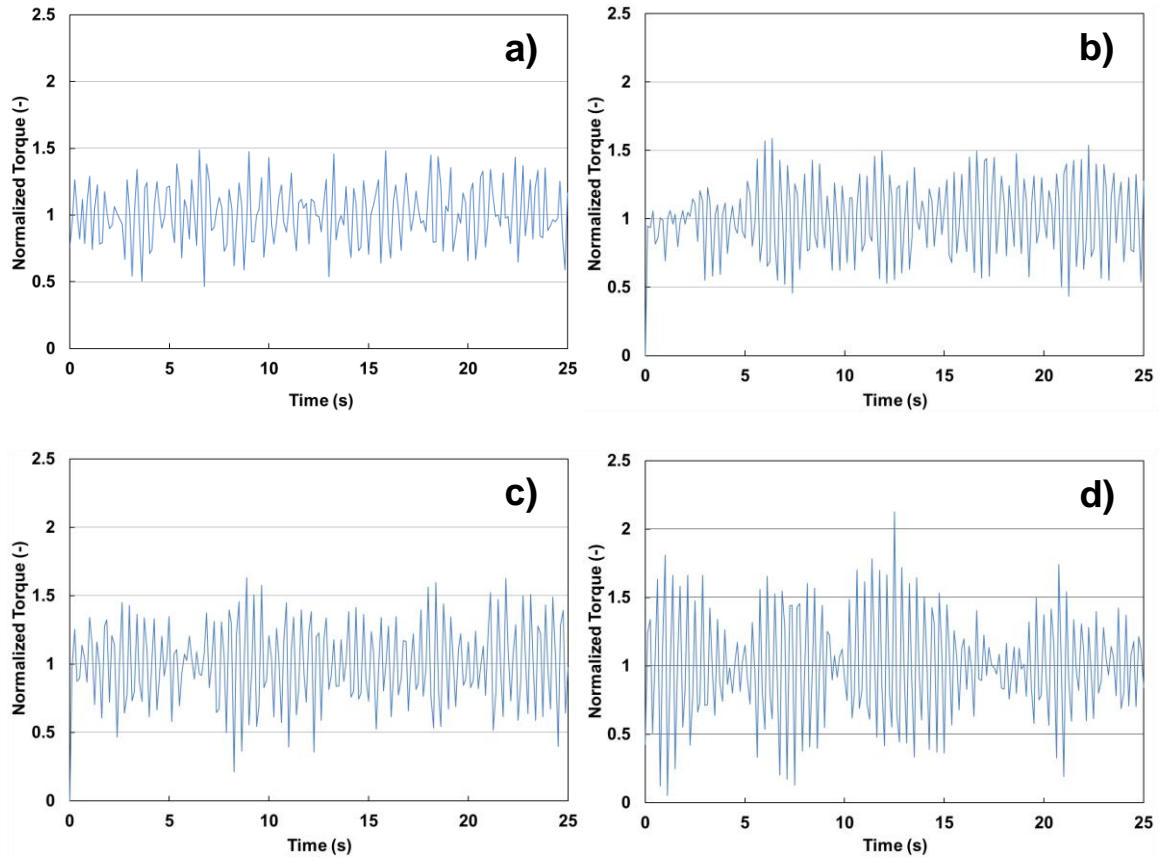


Fig. 4.2. Normalized torque (\vec{T}^*) fluctuation profiles at steady state for different blade rotational speeds: (a) 10 RPM, (b) 20 RPM, (c) 60 RPM, and (d) 200 RPM. The normalized torque values shown in this figure are the instantaneous torques divided by the time-averaged torque at each shear rate. Torque signal measurements were recorded every 0.125 seconds.

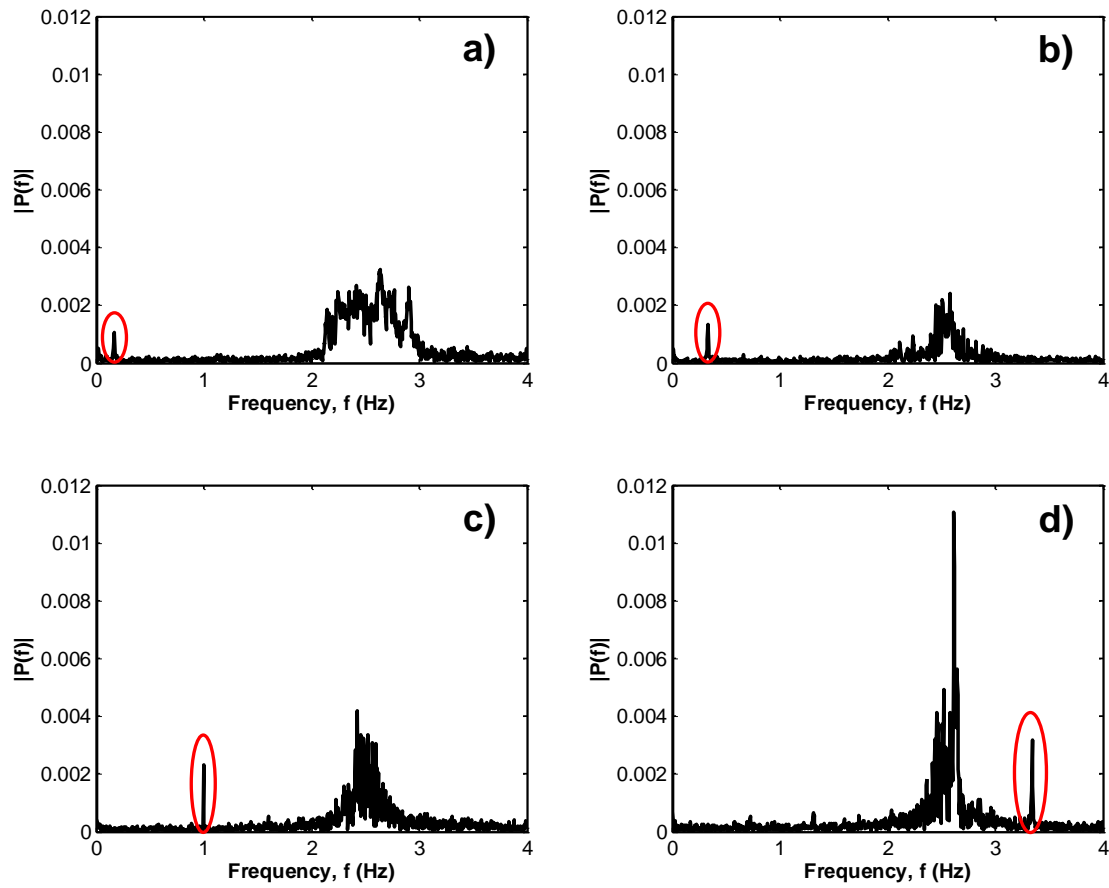


Fig. 4.3. Single-sided amplitude spectrums of the fast Fourier transform (FFT) torque signals for different blade rotational speeds: (a) 10 RPM, (b) 20 RPM, (c) 60 RPM, and (d) 200 RPM. Torque signal measurements were recorded every 0.125 s.

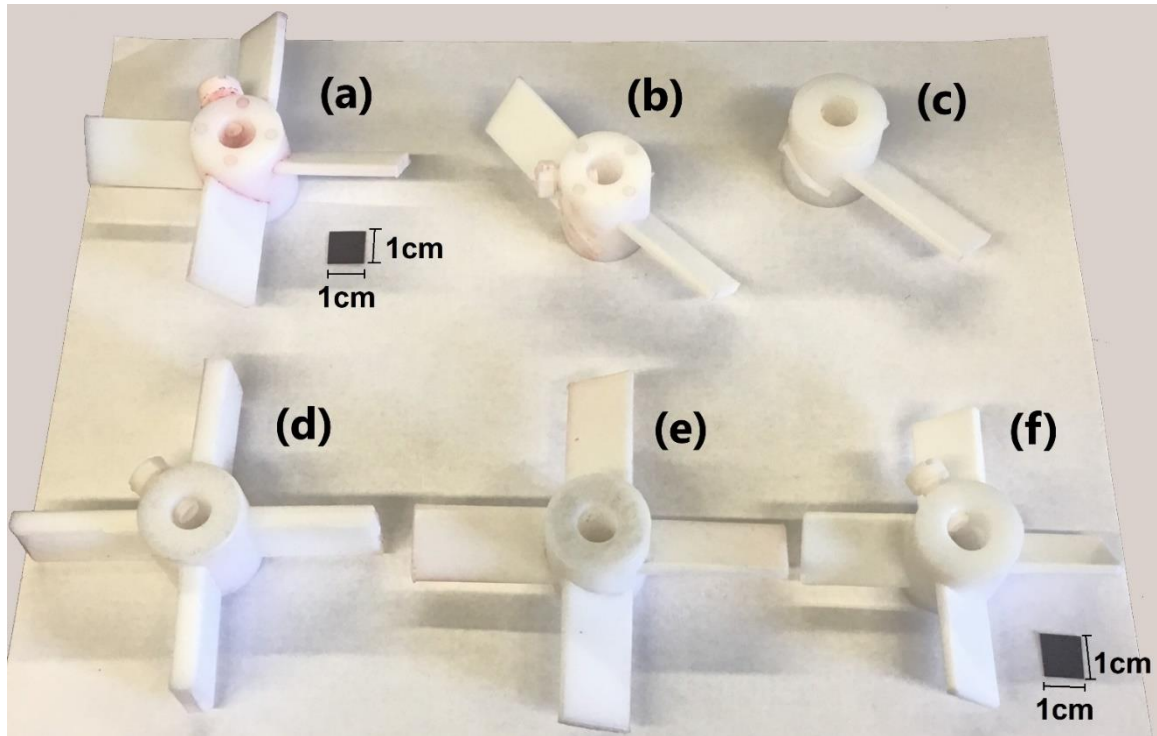


Fig. 4.4. Impeller blade configurations used in the experiments: (a) standard impeller, 4 blades, 45-mm length, 135° angle; (b) 2 blades, 45-mm length, 135° angle; (c) 1 blade, 45-mm length, 135° angle; (d) 4 blades, 45-mm length, 90° angle; (e) 4 blades, 45-mm length, 150° angle; and (f) 4 blades, 37.5-mm length, 135° angle. The black squares in this figure show an area of $1 \times 1 \text{ cm}^2$.

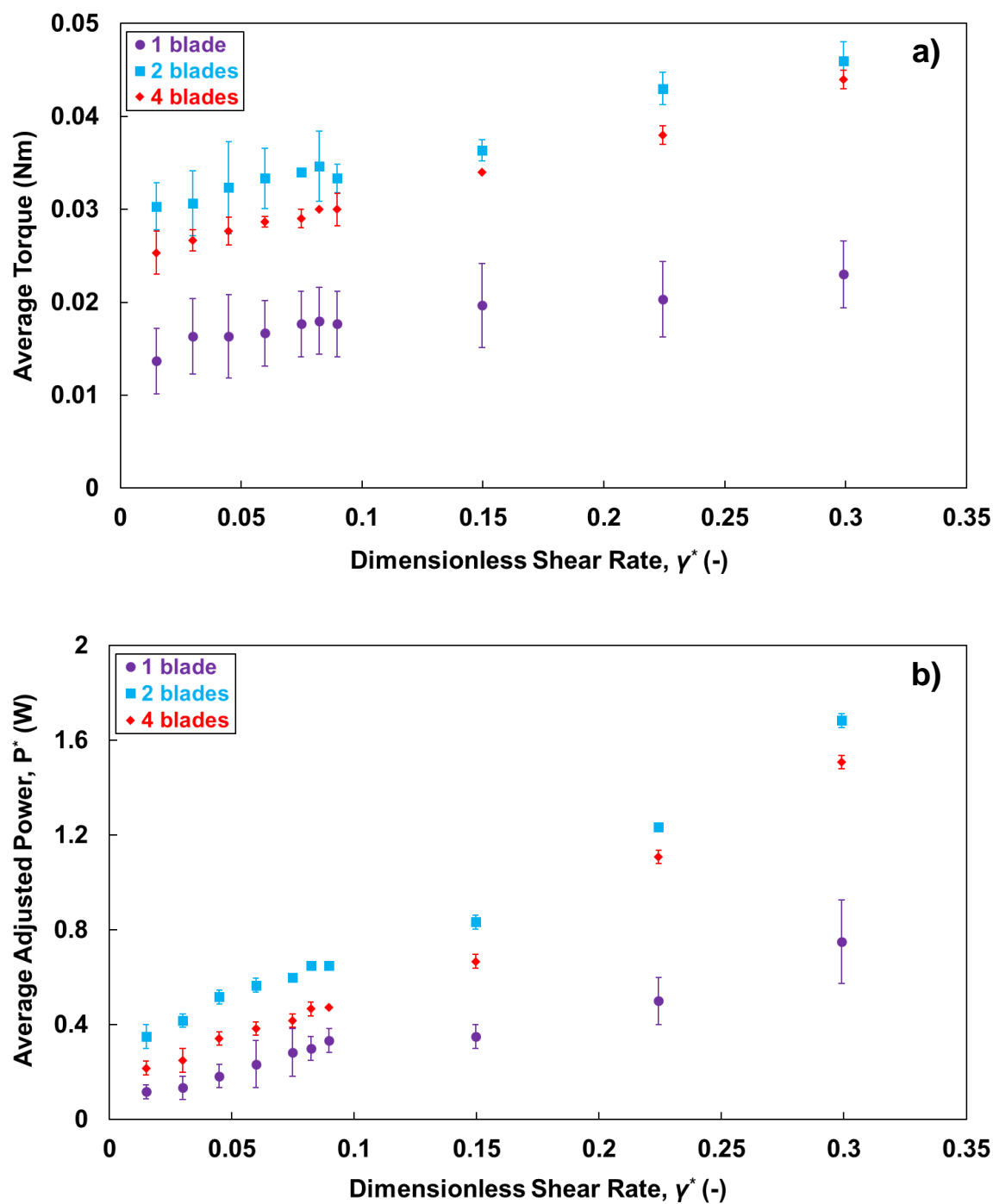


Fig. 4.5. Effect of the number of impeller blades on: (a) the average torque and (b) the average adjusted power as a function of the dimensionless shear rate. Impeller blades used in these sets of experiments have 135° angle and 45-mm length.

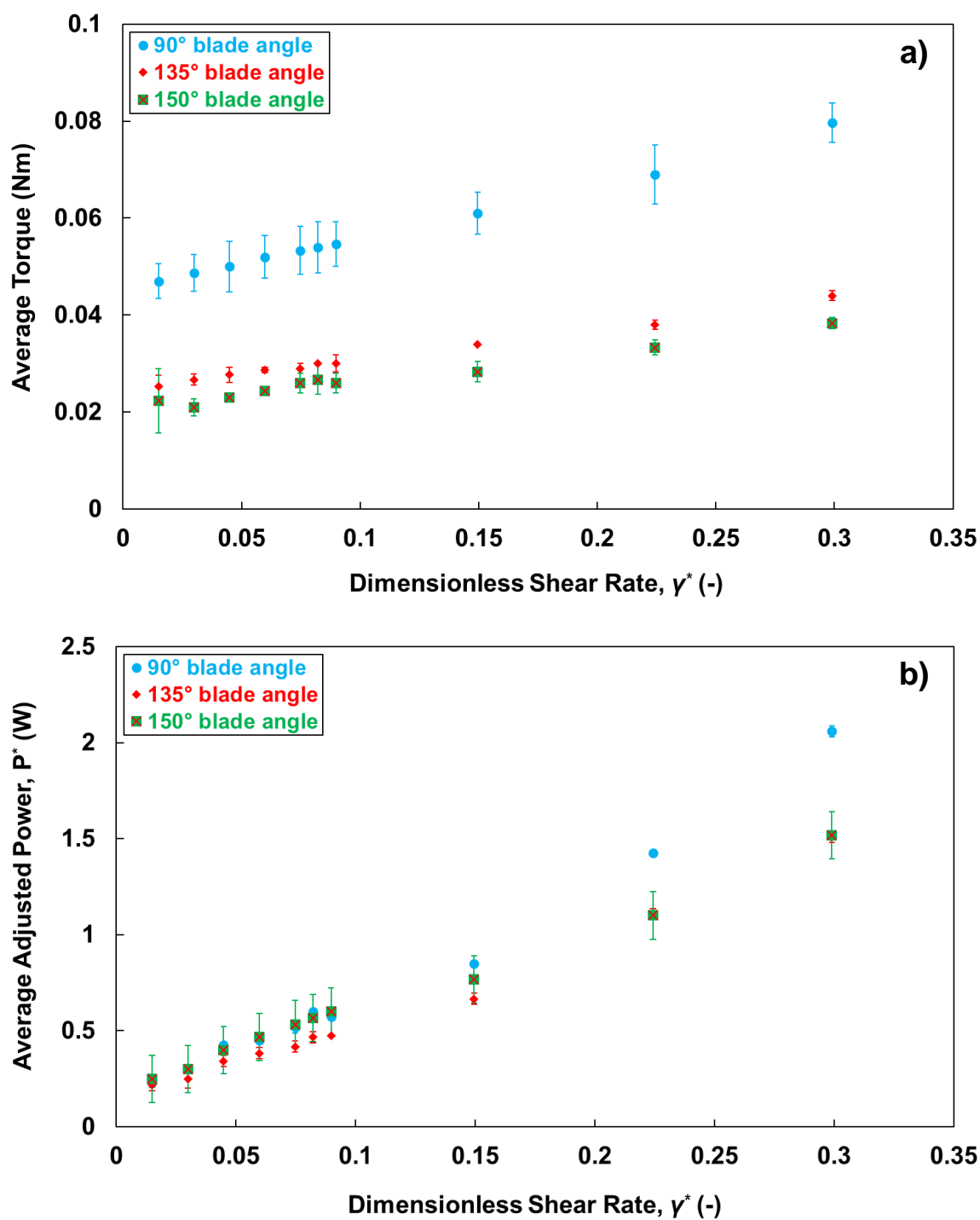


Fig. 4.6. Effect of the impeller blade angle on: (a) the average torque and (b) the average adjusted power as a function of the dimensionless shear rate. Impeller blades used in these sets of experiments have 4 blades and 45-mm length.

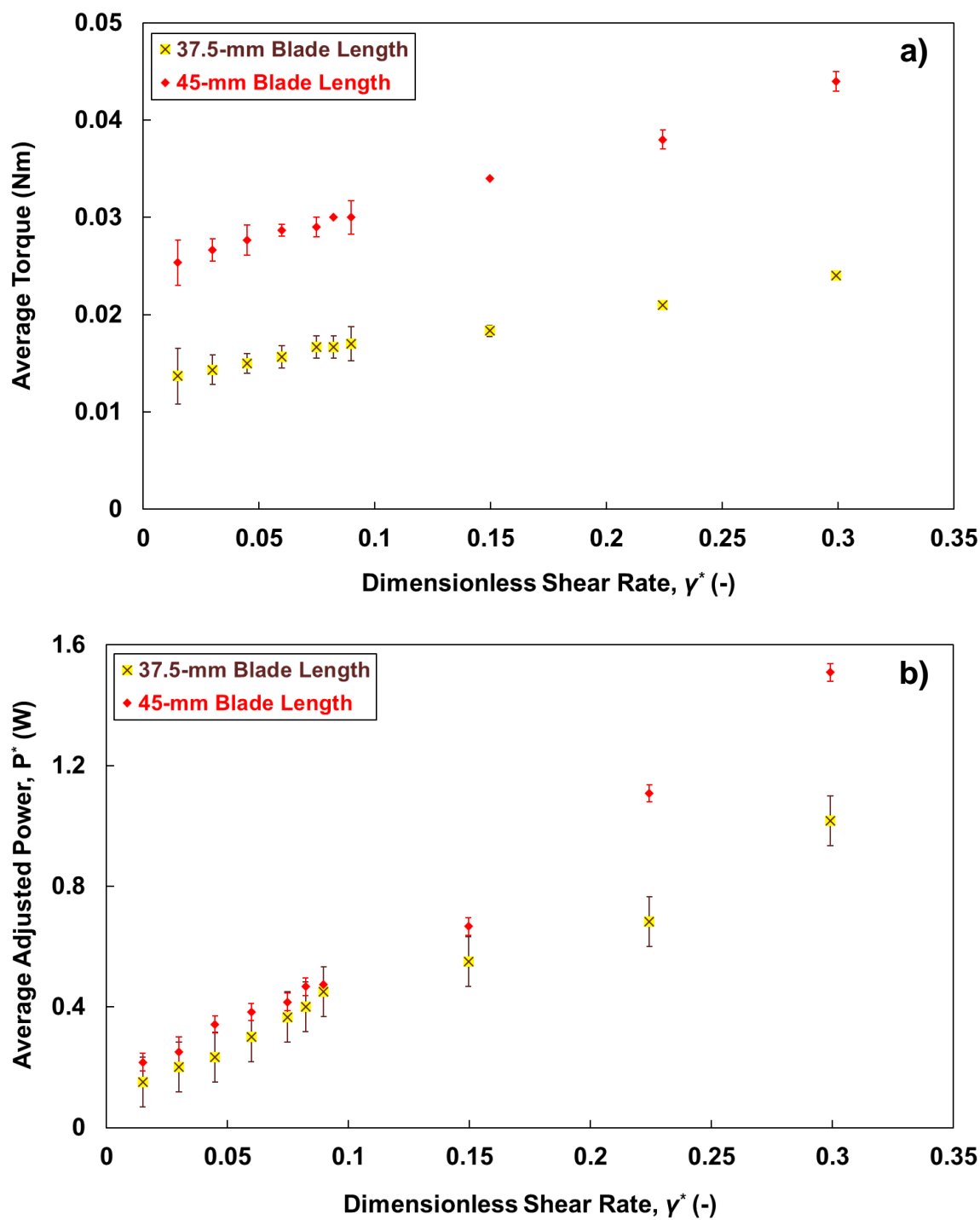


Fig. 4.7. Effect of the impeller blade length on: (a) the average torque and (b) the average adjusted power as a function of the dimensionless shear rate. Impeller blades used in these sets of experiments for both cases have 4 blades and 135° angle.

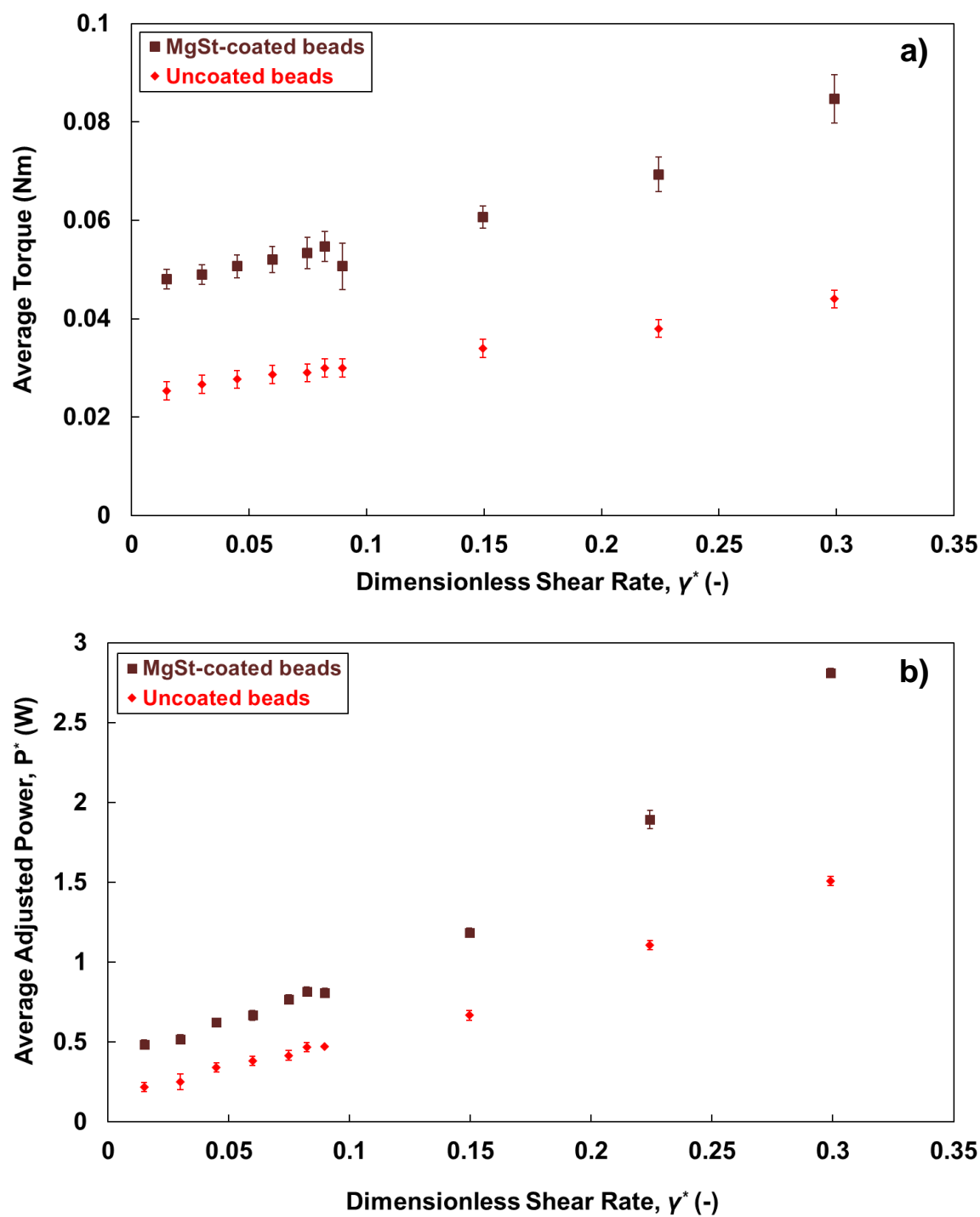


Fig. 4.8. Effect of the macroscopic friction coefficient (μ) of particles on: (a) the average torque and (b) the average adjusted power as a function of the dimensionless shear rate. Experiments were performed using the standard impeller blades and the glass beads with a diameter of 2 mm loaded to a 30-mm fill height ($H/D = 0.30$).

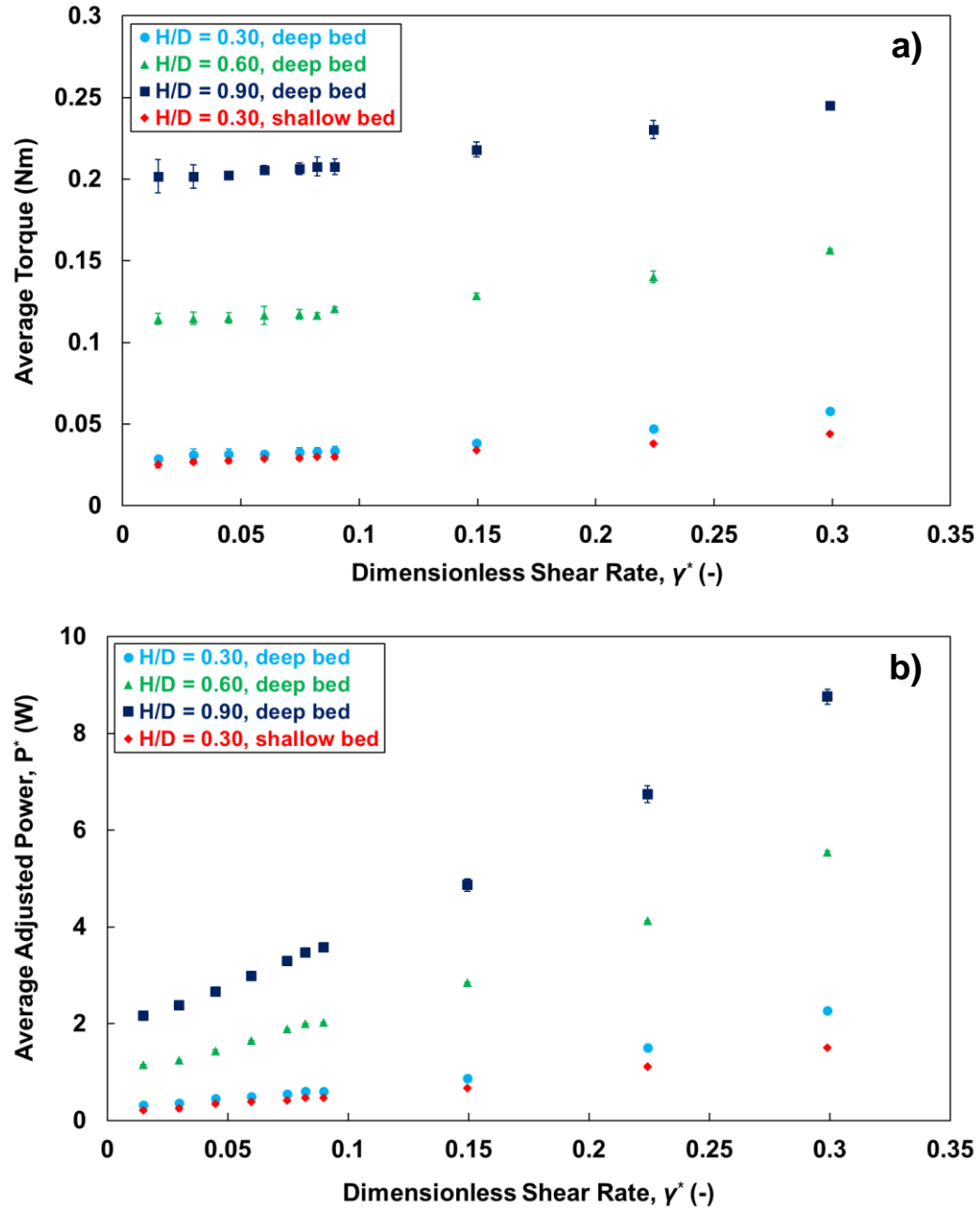


Fig. 4.9. Effect of the impeller blade position in a deep granular bed (90-mm fill height) on: (a) the time-averaged torque and (b) the average adjusted power as a function of the dimensionless shear rate, compared to those values in a shallow bed (30-mm fill height just covering the top tip of the blades). Blade position in a deep bed: top ($H/D = 0.30$), middle ($H/D = 0.60$), and bottom ($H/D = 0.90$). Experiments were performed using the standard impeller blades and the glass beads with a diameter of 2 mm.

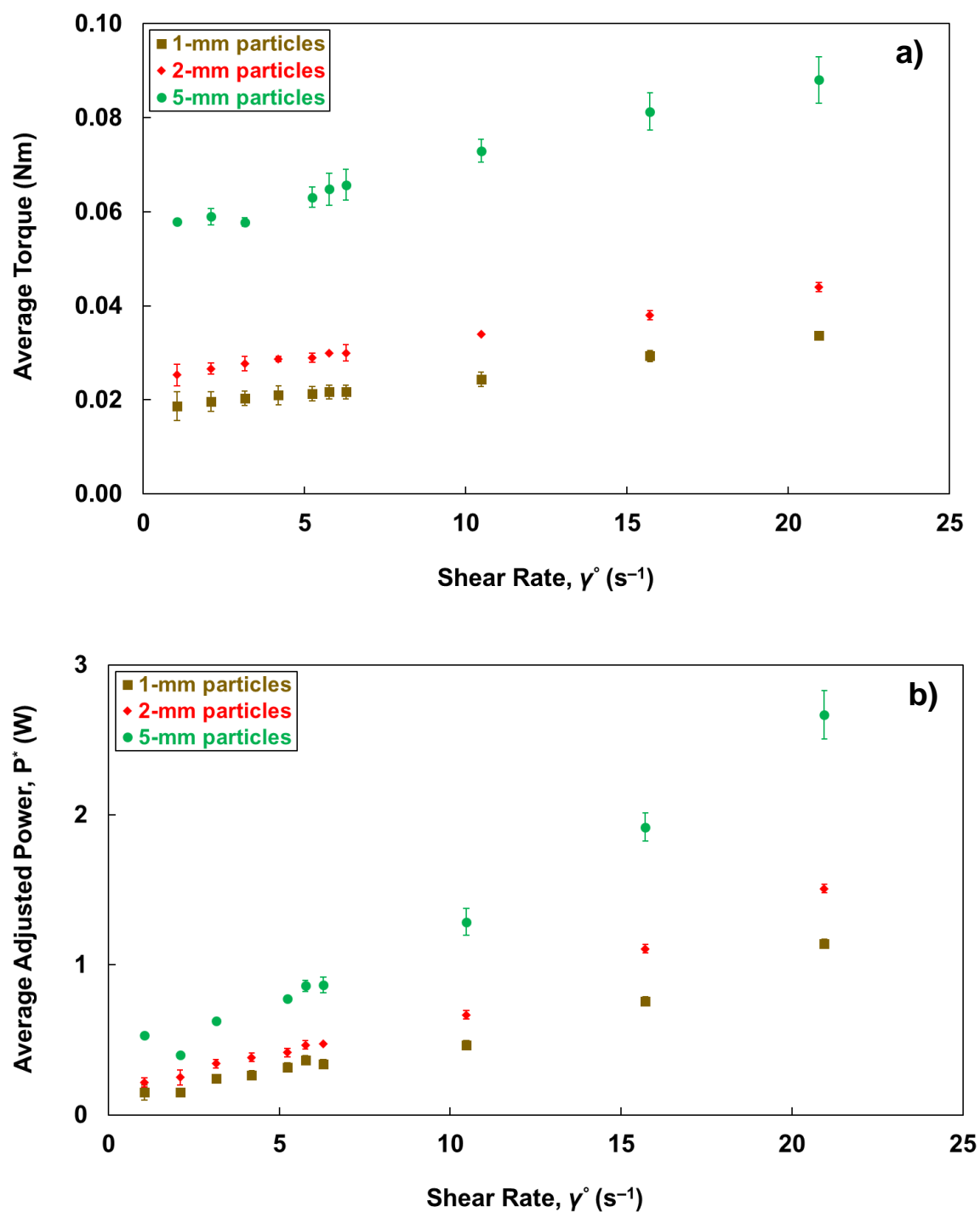


Fig. 4.10. Effect of the particle size on: (a) the average torque and (b) the average adjusted power drawn from experiments as a function of the shear rate γ° . Experiments were performed using the standard impeller blades, and the granular bed was filled up to a 30-mm height ($H/D = 0.30$) for all particle sizes.

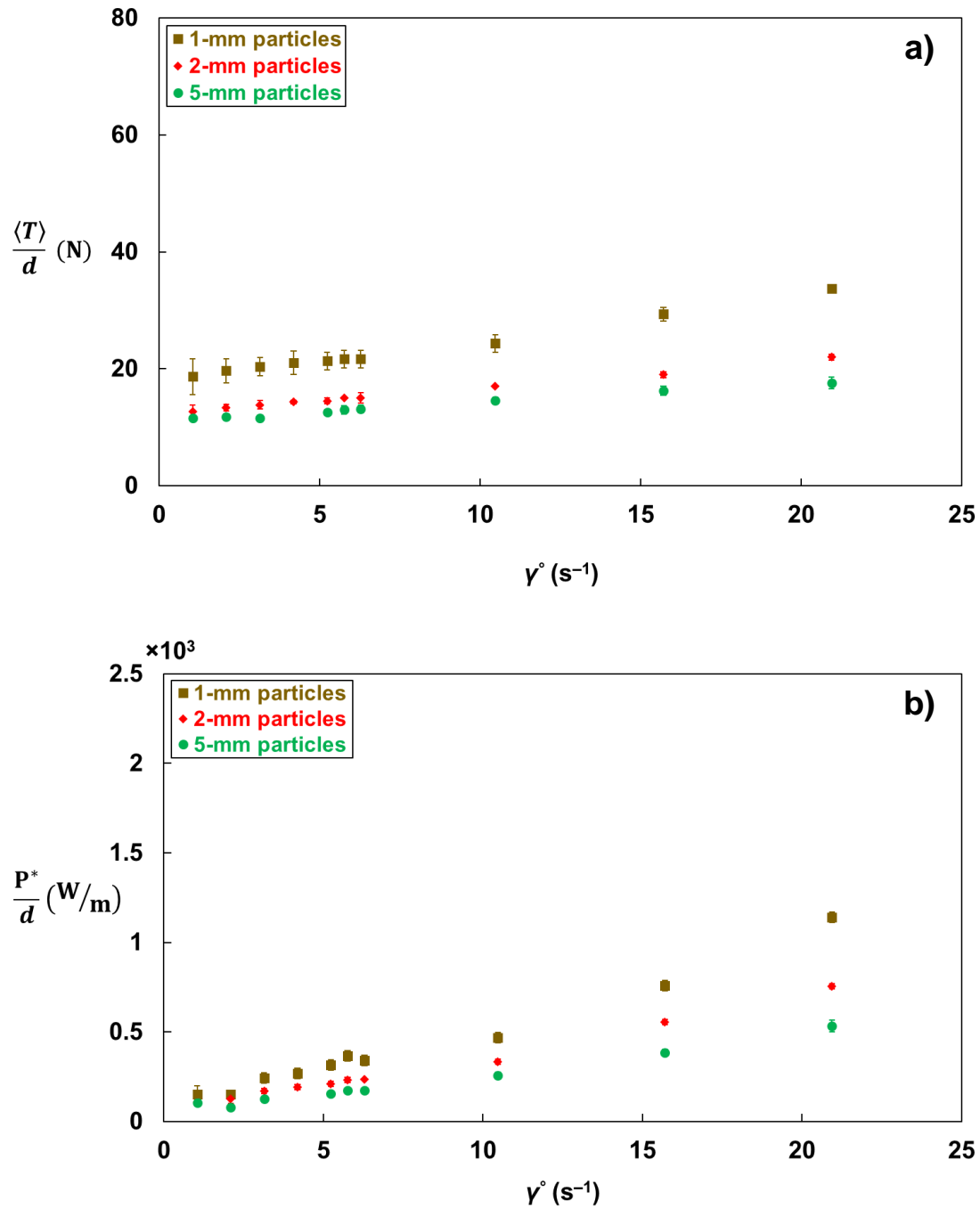


Fig. 4.11. (a) The time-averaged normalized torque, $\langle \vec{T} \rangle / d$, and (b) the average normalized adjusted power, P^* / d , plotted as a function of the shear rate γ° . Experiments were performed using the standard impeller blades, and the granular bed was filled up to a 30-mm height ($H/D = 0.30$) for all particle sizes. Note that the y-axis in Fig. 4.11b is multiplied by a factor of 10^3 .

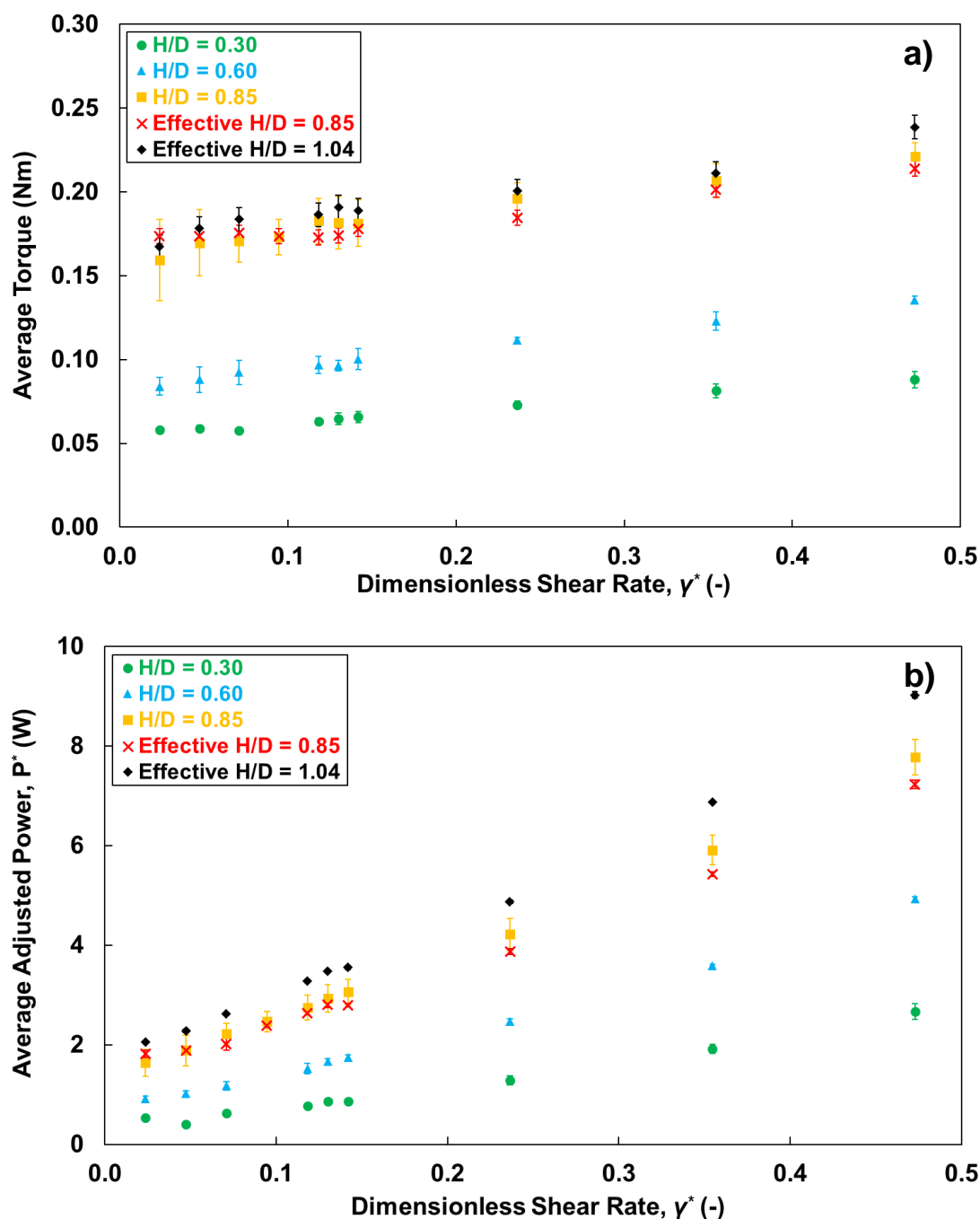


Fig. 4.12. Effect of the amount of materials in a bladed mixer, reported as the H/D ratio, on: (a) the time-averaged torque and (b) the average adjusted power as a function of the dimensionless shear rate. Experiments were performed using the standard impeller blades and the glass beads with a diameter of 5 mm. The effective H/D ratios indicate usage of a lead weight instead of using actual particle mass.

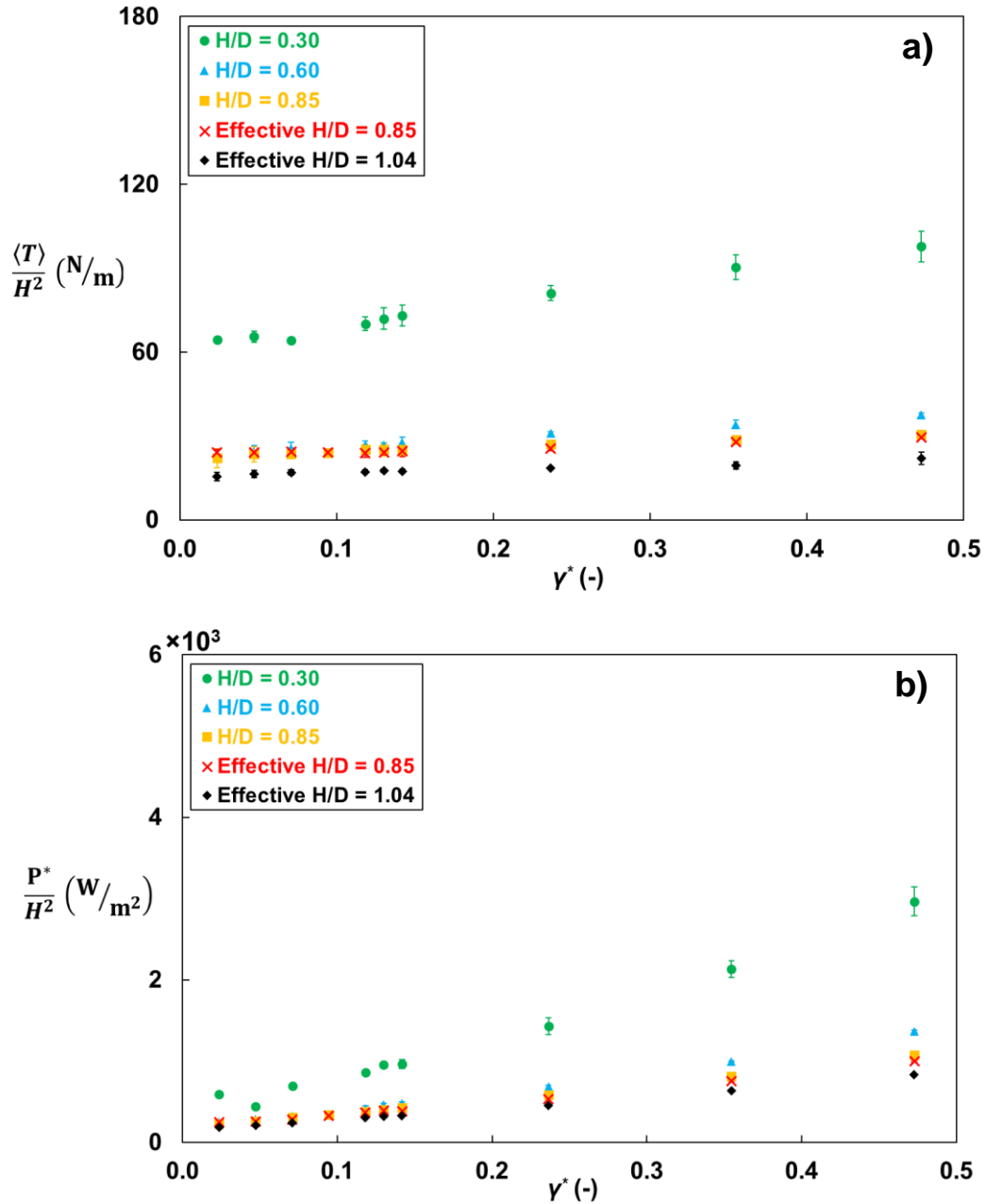


Fig. 4.13. (a) The time-averaged torque $\langle \vec{T} \rangle$ and (b) the average adjusted power P^* values in Fig. 4.12 were normalized by square of the height (H^2) of the granular material filled in a bladed mixer plotted as a function of the dimensionless shear rate. Experiments were performed using the standard impeller blades and the glass beads with a diameter of 5 mm. The effective H/D ratios indicate usage of a lead weight instead of using actual particle mass. Note that the y-axis in Fig. 4.13b is multiplied by a factor of 10^3 .

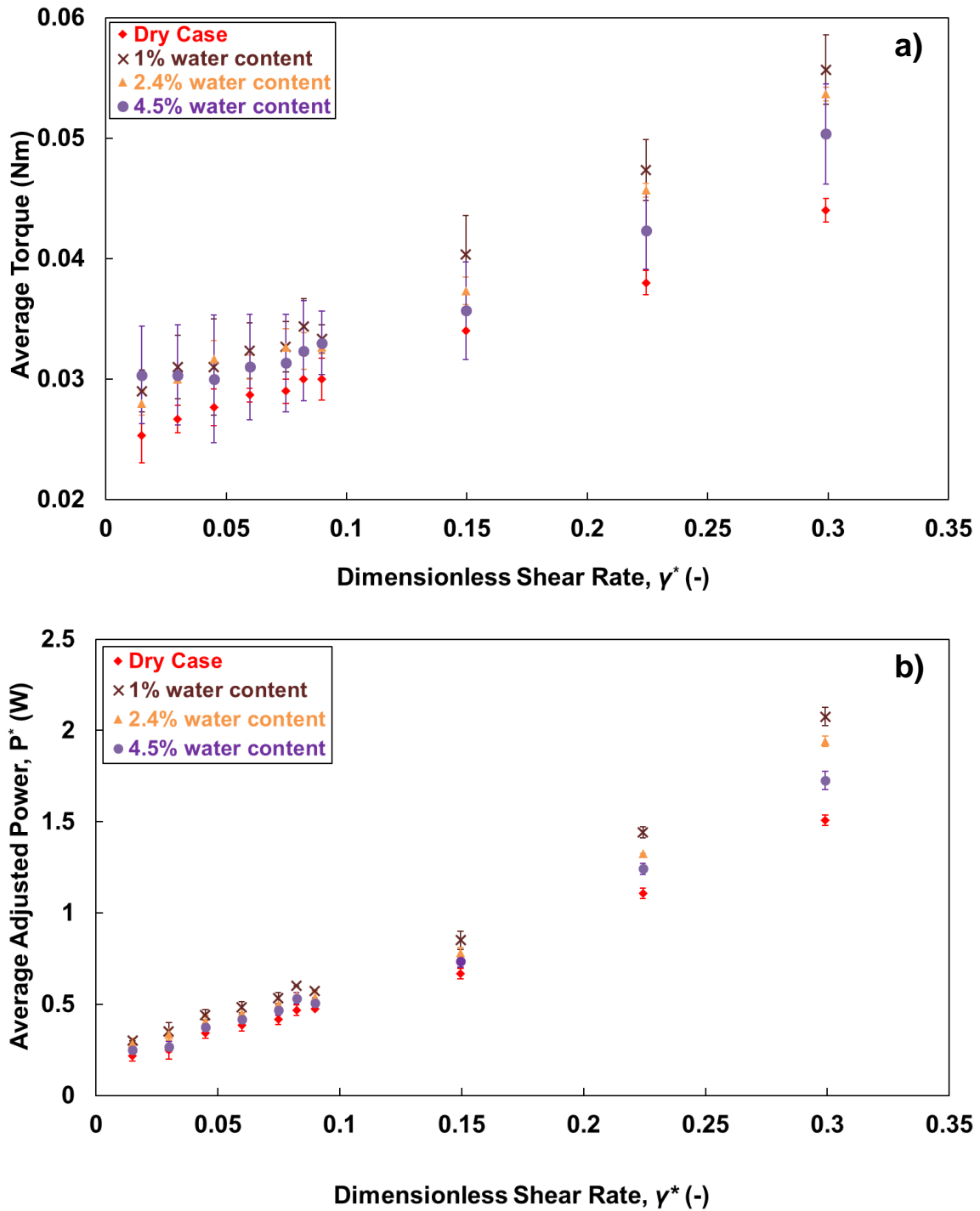


Fig. 4.14. Effect of the moisture content in granular systems on: (a) the average torque and (b) the average adjusted power as a function of the dimensionless shear rate. Experiments were performed using the standard impeller blades and the glass beads with a diameter of 2 mm loaded to a 30-mm fill height ($H/D = 0.30$).

Chapter 5. Scale-up of Cohesionless and Cohesive Granular Systems

5.1 Scale-up of Cohesionless Granular Systems: Effect of the Number of Blades

One might think that the effect of the number of impeller blades (see Chapter 3) on the properties of non-cohesive granular flows depends on the system size. We therefore studied how scaling up the system while simultaneously changing the number of blades has an influence on the cohesionless granular flow. The ratio of mixer diameter to particle diameter (D/d) has been shown to be an important parameter in other granular processes, and it is one of the parameters that changes during scale-up. For the results we have presented in Chapter 3, the ratio of D/d has been 63.0. We have carried out simulations for an increase in the D/d ratio from 63.0 to 90.0 in geometrically equivalent mixers. The numbers of blades used in the simulations in this section are two and four blades, and the rotational speed of the blades is set at 20 RPM for both D/d ratios. The fill level is set to $H/D = 0.17$ for both D/d cases studied, which is enough to just cover the blades.

5.1.1 Normalized Velocity Fields

In order to compare the results obtained from the different D/d ratios and to allow for plotting on the same axis, we normalized all particle velocities relative to the tip speed of the blades (V_{tip}). Fig. 5.1 depicts time-averaged radial (V_r) and vertical (V_y) velocity fields on a vertical plane for particles in front of the blade for different numbers of blades and D/d values. The magnitude of the tangential velocity (V_t) is represented by the color of the vectors. As can be seen from the figures, similar velocity fields for the 2-bladed

systems are observed for $D/d = 63$ (Fig. 5.1a) and $D/d = 90$ (Fig. 5.1b) and for the 4-bladed cases as well (Figs. 5.1c and d, respectively). The flow pattern obtained in front of the blade is independent of the D/d ratio for the cases we have studied, which confirms the results published by Remy et al. [24] investigating the effect of the D/d ratio for a 4-bladed mixer.

5.1.2 Mixing Kinetics

Fig. 5.2 shows the effects of the D/d ratio and the number of impeller blades on mixing performance. In this figure, the Lacey index (M) of the red particle concentration is plotted versus the number of revolutions of the blades. Little difference between the curves is observed between the D/d values of 63 and 90 for both two- and four-blade systems. The degree of mixing is very similar in all cases during the early stages of the mixing process, e.g. during 1 revolution. After 1 revolution the Lacey index curves for all cases increase and then reach a plateau. However, faster mixing kinetics and better mixing performance are observed for the simulations using a 2-bladed mixer compared to those for a 4-bladed system, as discussed previously. After 4 revolutions the Lacey index curves for the 2-bladed case approach the value of 1 while this is not the case for the 4-bladed system, regardless of scale.

5.1.3 Granular Temperature

We also studied the effect of the mixer diameter to particle diameter ratio for different numbers of impeller blades on the granular temperature. Fig. 5.3 depicts the time-averaged granular temperature as a function of position in the radial direction for

different D/d ratios using 2 and 4 impeller blades. In this figure, as previously discussed, the granular temperature curves obtained from the 2-bladed cases are in general higher than those from the 4-bladed systems, except for the fact that granular temperatures near the cylinder wall for the 4-bladed systems are slightly higher than those in the 2-bladed cases. All the granular temperature curves in this figure also follow the trend investigated by Remy et al. [23], i.e., lower granular temperature existed near the impeller shaft of a mixer, and maximum granular temperature was observed near the cylinder wall. In each case of number of blades used, the granular temperature values at various radial positions for $D/d = 63$ and $D/d = 90$ cases are reasonably comparable, which suggests that the D/d ratio has little effect on the granular temperature of the particle bed.

5.1.4 Particle Diffusivities

As mentioned before (see Section 2.1.5.2 in Chapter 2), particle diffusion has been previously shown to be dependent on system geometry and size in dense granular flows [89]. Table 5.1 presents the normalized diffusion coefficients (D_{ij}^*) in the tangential, radial, and vertical directions obtained from different D/d ratios for the 2- and 4-bladed cases. Particle diffusivities were normalized by the tip speed of the blades and the mixer diameter according to Eq. (2.21) in Chapter 2. For 2-bladed systems, very similar values of the normalized particle diffusion coefficients at the $D/d = 63$ and the $D/d = 90$ ratios are obtained in each direction. Similar results for the normalized particle diffusivities are also observed for the 4-bladed cases between both D/d values. Péclet numbers (see Eq. (2.22) in Chapter 2) for the different D/d ratios and different numbers of blades used are also shown in Table 5.1. For 2- and 4-bladed systems, almost equal values of the Péclet

numbers in each direction at the $D/d = 63$ and the $D/d = 90$ ratios are observed. These results suggest that changing the mixer diameter to particle diameter ratio for the cases we have examined has an insignificant effect on the diffusive contributions of the particle transport process.

5.1.5 Void Fraction

Bed dilation is also affected by the mixer diameter to particle diameter ratio [24]. Fig. 5.4 shows the time-averaged void fraction (ε) at two different D/d ratios for the 2- and 4-blade cases. In this figure, as discussed in Section 3.7 of Chapter 3, the values of the void fraction for the 2-bladed cases are higher than those obtained from the 4-bladed systems. In each of the two cases (2 or 4 blades), the void fraction curves for $D/d = 63$ and $D/d = 90$ lie on top of each other, which implies that the D/d ratio has insignificant impact on the void fraction of the granular bed for the cases we have examined.

5.2 Scale-up of Cohesive Granular Systems

The impact of scaling-up a bladed mixer in which cohesive granular materials are present is then further investigated. In the previous research conducted by Remy et al. [29], experiments and simulations of 2-mm diameter particle cohesive flows in a four-bladed mixer ($D/d = 50$) with the granular Bond number (Bo_g) of 5 were achieved, and the effect of moisture content (ϕ_{liq} ranging from 0.01 to 0.045) was thoroughly examined. When scaling-up a granular system (increasing the D/d ratio), the number of particles in a mixer also increases. The increased number of particles in simulations, combined with the complexity of the cohesive force – liquid bridge model in the DEM numerical algorithm,

requires significantly longer periods of time to complete a simulation. For some cases (e.g. at the largest D/d ratio that we selected), it took a couple of months to finish the runs which was highly time-consuming and computationally laborious, or in some cases it was almost impossible to accomplish even one simulation. From our previous work [28, 96], it has been shown that enlarging particle size (which results in an increase in the calculation grid cell size and the computational time-step) can speed up DEM simulations and shorten the time required to finish runs. Furthermore, it has been previously validated from parametric sensitivity studies that changing the particle diameter (d) within the range from 2 mm to 10 mm did not significantly affect flow properties and mixing performance of the granular systems [27]. Therefore, in this section only we will change the particle diameter to 10 mm to shorten the simulation time.

Simulations in this section were carried out employing the liquid bridge model in EDEM™ [29], and the cohesive contact force model was followed (see Section 2.1.3 in Chapter 2). The input parameters for the cohesive force model in DEM simulations were listed in Table 2.3 and described in Section 2.1.4 of Chapter 2. This table also showed the value of the granular Bond number (Bo_g) set in the simulations, which is the ratio of the cohesive force to the gravitational force and is defined by McCarthy [101] as

$$Bo_g = \frac{3\gamma}{2R^2\rho_p g} \quad (5.1)$$

where γ is liquid surface tension, R is particle radius, ρ_p is particle density, and g is the gravitational acceleration. In all wet simulations studied in the previous work by Remy et al. [29], the magnitude of the cohesive force is approximately 5 times that of the force due to gravity, and this value yielded interesting results for cohesive particle flows.

Therefore, in order to keep the Bo_g value constant at five in this work, since the particle radius (R) is increased five times from 1 mm in the previous work [29] to 5 mm in our simulations, the liquid surface tension (γ) is thus increased by 25 times from 0.073 N/m reported in the previous paper [29] to 1.825 N/m in our DEM simulation model (see Table 2.3 in Chapter 2).

In this section, we study the effect of increasing the mixer diameter (D) while keeping the particle diameter (d) constant at 10 mm and compare the cohesive granular flow behaviors observed in bladed mixers at D/d ratios of 50, 75 and 100. For the parameters used in this work, the range of D/d ratios studied includes mixer sizes ranging from 98 L to 785 L. The mixer dimensions for the $D/d = 50$ case are the ones listed in Table 2.6 of Chapter 2. The dimensions of the $D/d = 75$ system are a 1.5 times linear scale-up of the values shown in Table 2.6. The $D/d = 100$ dimensions are twice the Table 2.6 values. The only dimension that is kept constant for all mixer sizes is the gap between the bottom plate of the mixer and the bottom of the blades (H_2) and it is set to 10 mm for all system scales. For all of the D/d cases studied, the initial fill height of the spherical glass beads in the bladed mixers was set to $H/D = 0.3$ which was the amount of material just covering the top tip of the impeller blades. The rotational speed of the blades (RPM) for mixers at different D/d ratios was varied such that simulations in this section were accomplished using a constant tip speed (V_{tip}) of the impeller blades of 0.589 m/s for all mixer sizes. Because a constant tip speed of the blades was used for all system scales, the blade rotational speed decreased with an increase in the D/d ratios in our simulations. It has been observed in the previous scale-up research that setting the blade rotational speed

constant in simulations yielded similar results for particle dynamics and mixing kinetics to setting the blade tip speed constant as long as the cohesionless granular system was in the quasi-static regime [24]. However, this should be further investigated in cohesive granular flows.

For cohesive granular flows in this study, the moisture content was varied from 1 percent ($\phi_{\text{liq}} = 0.01$) to 4.5 percent ($\phi_{\text{liq}} = 0.045$) in the systems, and the particle dynamics behaviors as well as the mixing kinetics were compared to the cohesionless dry case ($\phi_{\text{liq}} = 0$). In order to compare the results obtained from the different system sizes (D/d ratios) and to allow for plotting in the same axis, we normalized all particle dynamic quantities relative to the tip speed of the blades (V_{tip}). Particle positions were normalized by the total bed height (H) in the vertical direction and by the mixer radius (R) in the radial direction. Flow behaviors and mixing kinetics of cohesive granular systems with different mixer scales along with varying moisture content were analyzed as follows.

5.2.1 Normalized Tangential Velocity Profiles

In this section, we compare velocity profiles of particles obtained from the DEM simulations of cohesive granular flows to those obtained from the cohesionless granular system simulations for different system scales. Fig. 5.5 depicts instantaneous tangential velocity profiles obtained for the DEM simulations at different system sizes (D/d ratio) and at different liquid contents (ϕ_{liq}). Here, the tangential velocities were normalized by the tip speed of the impeller blades, V_{tip} . In simulations, an approximate 40 mm \times 40 mm square control area was created at the top free surface of the granular bed and at $r/R =$

0.5, and only the velocities of the particles located 0.75 particle diameters away from the top surface were included in the calculation. The instantaneous velocity components were calculated by averaging over the control area at a particular time-step. Tangential velocity of particles in front of the blades at $r/R = 0.5$ for each D/d ratio was normalized by the tip speed of the blades for each system size.

In the dry systems ($\phi_{liq} = 0$), periodic fluctuations of normalized tangential velocities (V_t/V_{tip}) of particles with distinct peaks are observed for all of the D/d ratios (Fig. 5.5a – c). These fluctuations develop because the particles in front of the impeller blades possess greater tangential velocities than the particles behind the blades [23]. The normalized tangential velocity profiles for cohesionless granular flows examined in this work are similar to those obtained from simulations in previous research studies by Remy et al. [23, 24, 27, 29]. In these figures, the number of velocity oscillations per revolution correlates with the number of impeller blades used in an agitated mixer (which is four blades in our case for all system sizes). A fast Fourier transform (FFT) analysis of the tangential velocity profiles reveals that the main frequency of the fluctuations is equal to the rotation frequency of the impeller blades for each D/d ratio (not shown). The normalized instantaneous tangential velocity (V_t/V_{tip}) values in this figure show differences in the amplitude of the fluctuations. It is noticeable that at $\phi_{liq} = 0$ the amplitude of the normalized tangential velocity fluctuation peaks is the lowest for the $D/d = 50$ case (Fig. 5.5a) while significantly higher amplitudes are attained for the $D/d = 75$ (Fig. 5.5b) and $D/d = 100$ (Fig. 5.5c) cases. The higher fluctuation amplitudes suggest that particle movement in the tangential direction is less uniform in bladed mixers of D/d

> 50 , which is consistent with the result found in the previous paper by Remy et al. [24]. For $\phi_{\text{liq}} = 0$ the normalized tangential velocity curves for $D/d = 75$ (Fig. 5.5b) and $D/d = 100$ (Fig. 5.5c) are comparable, and little difference between these two graphs is identified suggesting that cohesionless granular flows in these two system scales converge into a single behavior.

For wet granular flows ($\phi_{\text{liq}} = 0.01$ and 0.045), due to addition of cohesion [29], the amplitudes of the normalized tangential velocity fluctuations are in general different from those in the dry cases for each D/d ratio (Fig. 5.5a – c). The periodicity of fluctuation displayed in the cohesive granular systems, especially for a $D/d = 50$ mixer (Fig. 5.5a at $\phi_{\text{liq}} = 0.01$ and 0.045), is less than what has been observed in the dry velocity profiles (at $\phi_{\text{liq}} = 0$) for all D/d ratios. Inspection of DEM simulations shows that the alteration in the normalized tangential velocity fluctuations is due to agglomeration of a large portion of particles in a granular bed in front of the impeller blades. These agglomerated particles move along with the rotation of the blades leading to a different tangential velocity profile inside the mixer [29]. It is also important to note that at each moisture content level ($\phi_{\text{liq}} = 0.01$ and 0.045) the normalized tangential velocity profiles for D/d ratios of 75 (Fig. 5.5b) and 100 (Fig. 5.5c) are shown to be qualitatively identical, suggesting that cohesive granular flows in these two larger scaled mixers ($D/d = 75$ and 100) converge into a similar behavior although cohesion is present in the systems.

5.2.2 Mixing Patterns

To visualize mixing processes of cohesionless and cohesive granular materials at different scales of bladed mixers, a vertical cylindrical blending vessel was virtually divided into two sections by a vertical YZ plane at the center of the mixer. Prior to the blade movement, particles on the left side of the vertical plane were colored as yellow, and particles on the right side were colored as blue. These two types of particles had identical properties except for their colors. We then observed the mixing pattern after the blade motion had begun. Fig. 5.6 – 5.8 display EDEM™ top-view snapshots of particles showing the mixing process at different D/d ratios ($D/d = 50, 75$, and 100) for the dry systems (Fig. 5.6) and for the wet systems at moisture content (ϕ_{liq}) of 0.01 (Fig. 5.7) and 0.045 (Fig. 5.8) taken at different numbers of revolutions (REV). In general, for both cohesionless and cohesive granular flows in all D/d ratio cases, well-mixed zones are first observed by the wall of the cylindrical vessel. The areas around the impeller shaft at the center of a mixer remain unmixed due to the fact that the speed of the blades at any point is ωr , and thus decreases as you get closer to the center. These unmixed areas close to the impeller shaft gradually decrease for prolonged periods of time. Additionally, enhanced mixing is obtained for the bladed mixers of $D/d = 75$ and 100 when compared to the $D/d = 50$ system at the same revolution of the blades in the initial mixing stages.

In the non-cohesive systems (Fig 5.6), mixing is down to the particle-particle level after the impeller blades pass 8 REV, and among the three blender sizes there is no significant difference of the mixing pattern observed at the final time step (15 REV in our case). For the wet granular flows, agglomerates of particles are formed and stick to mixer walls and

center shafts. The unmixed regions around the impeller shafts for both moisture content levels ($\phi_{\text{liq}} = 0.01$ in Fig. 5.7 and $\phi_{\text{liq}} = 0.045$ in Fig. 5.8) reduce in size over time. Moreover, we observe that mixing patterns of cohesive particulate systems do not significantly change after passing 8 REV to 15 REV; however, these unblended areas in the central parts of the mixers are still present even though the blades have undergone 15 revolutions. For the case of moisture content $\phi_{\text{liq}} = 0.01$, slight difference in the mixing pattern at the final time step can be viewed. It is important to point out that, for $\phi_{\text{liq}} = 0.045$, the $D/d = 50$ case exhibits a significantly larger unmixed central region at the final time step compared to the $D/d = 75$ and 100 cases. The mixing pattern of particles at 15 REV for the D/d ratio of 75 case is qualitatively similar to that for the D/d ratio of 100 case.

5.2.3 Mixing Kinetics

Statistical analysis of mixing kinetics for wet simulations varying the system size was also performed by calculating relative standard deviation (RSD) values of particle concentration of a particular type in the entire granular systems (see Section 2.1.5.5 in Chapter 2). The size of the control volume (V_C) used for the RSD computation in this section is $5d \times 5d \times 5d$, where d is the particle diameter, such that $V_C/V_p = 240$, where V_p is volume of one particle as most of the averaged macroscopic quantities are invariant of the sampling cell size at this V_C/V_p value [29]. Figs. 5.9 – 5.11 display the effect of system scale on the RSD curves of the blue particle concentrations as a function of the number of blade revolutions for the different D/d ratio cases at $\phi_{\text{liq}} = 0$ (Fig. 5.9), $\phi_{\text{liq}} = 0.01$ (Fig. 5.10), and $\phi_{\text{liq}} = 0.045$ (Fig. 5.11). There is little difference in the degree of

mixing during the early stages (< 2 REV) of the blending process in all cases. Moreover, the RSD curves in all cases generally begin to level off after approximately 5 revolutions of the impeller blades. For each D/d ratio, mixing performance for the $\phi_{\text{liq}} = 0.01$ cases (Fig. 5.10) is enhanced and better than the dry cases (Fig. 5.9) and the $\phi_{\text{liq}} = 0.045$ cases (Fig. 5.11), respectively. The effect of moisture content on the mixing RSD was explained in the previous research by Remy et al. [29]. In Figs. 5.9 – 5.11, faster mixing kinetics can be essentially observed for the $D/d > 50$ cases at all levels of cohesion. The differences in the degree of mixing are still present after 15 revolutions when comparing the small system ($D/d = 50$) to the larger scales ($D/d = 75$ and 100) at each cohesion level. Regardless of the liquid content in the systems, the RSD curves for the $D/d = 75$ and 100 cases start to converge into a single line especially after 10 revolutions although the RSD values are not perfectly identical. This result indicates that similar mixing kinetics are acquired for the cohesive granular systems of $D/d \geq 75$ for the cases we have examined.

In addition to the global mixing rate for the entire granular bed, we also examine the local degree of mixing of particles in simulations. Figs. 5.12 – 5.14 show the localized RSD values after 15 revolutions of the blades for different D/d ratio cases as a function of dimensionless radial positions (r/R) at $\phi_{\text{liq}} = 0$ (Fig. 5.12), $\phi_{\text{liq}} = 0.01$ (Fig. 5.13), and $\phi_{\text{liq}} = 0.045$ (Fig. 5.14). For the dry system (Fig. 5.12) and the $\phi_{\text{liq}} = 0.045$ case (Fig. 5.14), RSD values near the impeller shaft at the center of the mixer typically decrease with an increase in the radial position ($r/R = 0.2$ to 0.8) for all D/d ratios. In contrast, for the $\phi_{\text{liq}} = 0.01$ case (Fig. 5.13), the RSD values decline abruptly until $r/R \sim 0.4$ and start to plateau

out after $r/R = 0.6$ for all system scales. Close to the mixer walls ($r/R > 0.8$), the RSD values are the smallest with similar numbers obtained for all different cases. This is because of the shear effect between the cylindrical mixer walls and the impeller blades, resulting in rapid mixing rates in this area [29]. In general, the high moisture content cases, $\phi_{\text{liq}} = 0.045$ (Fig. 5.14), are described by higher RSD curves (poorer mixing performance) than the cohesionless systems, $\phi_{\text{liq}} = 0$ (Fig. 5.12), and the low moisture content cases, $\phi_{\text{liq}} = 0.01$ (Fig. 5.13), respectively. These results are consistent with a phenomenon studied by Remy et al. [29] investigating the effect of moisture content on mixing of wet granular systems. It can be seen that, regardless of the moisture content level, the RSD versus r/R curves in the systems of $D/d = 75$ and 100 almost lie on top of each other and are significantly lower than those in the $D/d = 50$ cases. This suggests that greater mixing performance can be locally achieved in the larger system scales, and that the local degree of mixing of cohesive granular systems begins to converge when $D/d \geq 75$ (for the cases we have examined).

5.2.4 Particle Diffusivities

As mentioned earlier, diffusivities of particles have been measured in previous work [89] and they depended upon the mixer geometry and size. In Table 5.2, we present the normalized diffusion coefficients (D_{ij}^*) in the tangential, radial, and vertical directions obtained from different D/d ratios for cohesionless ($\phi_{\text{liq}} = 0$) and cohesive ($\phi_{\text{liq}} = 0.01$ and 0.045) granular systems. Particle diffusivities were normalized by the tip speed of the impeller blades and the mixer diameter according to Eq. (2.21) in Chapter 2. In general, for each cohesion level normalized particle diffusivities in all directions decrease with an

increase in the mixer size; however, the normalized diffusion coefficient values change little for the $D/d \geq 75$, similar to the flow behaviors of cohesive granular matters observed for the convective particle motion. For $D/d = 50$, $D_{\theta\theta}^*$ are significantly higher than D_{rr}^* and D_{yy}^* for all moisture content levels while we notice the opposite trend for the D/d ratios of 75 and 100 cases.

Péclet numbers (see Eq. (2.22) in Chapter 2) for the different D/d ratios along with varying the cohesion from $\phi_{\text{liq}} = 0$ to 0.01 and 0.045 are also shown in Table 5.2. All computed Péclet numbers are greater than unity suggesting that convection, due to the impeller blade rotation, is the primary mechanism of particle movement regardless of the system scale and the moisture content level. For each D/d ratio, convection in the tangential direction dominates the transport process for both dry and wet systems since in all cases $Pe_{\theta\theta}$ is much larger than Pe_{yy} and Pe_{rr} , respectively. Adding cohesion into the systems significantly reduces the $Pe_{\theta\theta}$ values by three to four times in the $D/d = 50$ mixer, but lowers $Pe_{\theta\theta}$ approximately by half in the $D/d = 75$ system and slightly lessens $Pe_{\theta\theta}$ in the $D/d = 100$ system. The decline in the $Pe_{\theta\theta}$ values when cohesion is present in the systems may be due to formation of agglomerates in front of the impeller blades that might be able to hinder the tangential convective transport of the particles [29]. This data is consistent with an increase in the particles' normalized tangential diffusion coefficients ($D_{\theta\theta}^*$) in Table 5.2 when incorporating liquid into the systems. While little difference in the Pe_{rr} and Pe_{yy} values for all D/d ratios and all moisture content levels is recognized, the $Pe_{\theta\theta}$ values in the D/d ratio of 100 and 75 cases for each liquid content level are much larger than those in the $D/d = 50$ case, respectively. Moreover, the $Pe_{\theta\theta}$ values for $\phi_{\text{liq}} =$

0.01 and 0.045 in the $D/d = 75$ mixers slightly change when D/d ratio is increased to 100. This therefore indicates that, above a specific system size ($D/d \geq 75$ in our case), particle convection scales with the radius of the mixer and the tip speed of the impeller blades, and that cohesive granular flow behaviors begin to converge for bladed mixers of $D/d \geq 75$.

5.3 Conclusions for Chapter 5

In this chapter, the effect of scaling up a mixer was analyzed together with the effect of the number of impeller blades in cohesionless granular systems. The system scale was varied by changing the mixer diameter to the particle diameter (D/d) ratio. Cases utilizing 2 and 4 impeller blades at both D/d ratios equal to 63 and 90 exhibited similar characteristics in terms of velocity fields, degree of mixing, granular temperature, particle diffusivities, and void fraction of the particle bed. It was concluded that increasing the system size from $D/d = 63$ to 90 had an insignificant impact on the behavior of particulate flows in the mixing systems we examined. Scale-up of non-cohesive granular systems based on the number of impeller blades (2 and 4 blades) used in the agitated mixer could be scaled by the diameter of the mixer and the rotational speed of the impeller blades within the range from $D/d = 63$ to 90.

In this section, we also studied the effect of increasing the mixer diameter (D) while keeping the particle diameter (d) constant at 10 mm and compared the cohesive granular flow behaviors observed in bladed mixers at D/d ratios varying from 50 to 75 and 100. For cohesive granular flows in this study, the moisture content was varied from 1 percent

($\phi_{\text{liq}} = 0.01$) to 4.5 percent ($\phi_{\text{liq}} = 0.045$) in the systems, and the particle dynamics behaviors as well as the mixing kinetics were compared to the cohesionless dry case ($\phi_{\text{liq}} = 0$). It was observed that, above a specific system size ($D/d \geq 75$ in our case), normalized tangential velocity fluctuation, mixing rates, and normalized particle convection scaled with the diameter of the mixers and the tip speed of the impeller blades.

5.4 Figures for Chapter 5

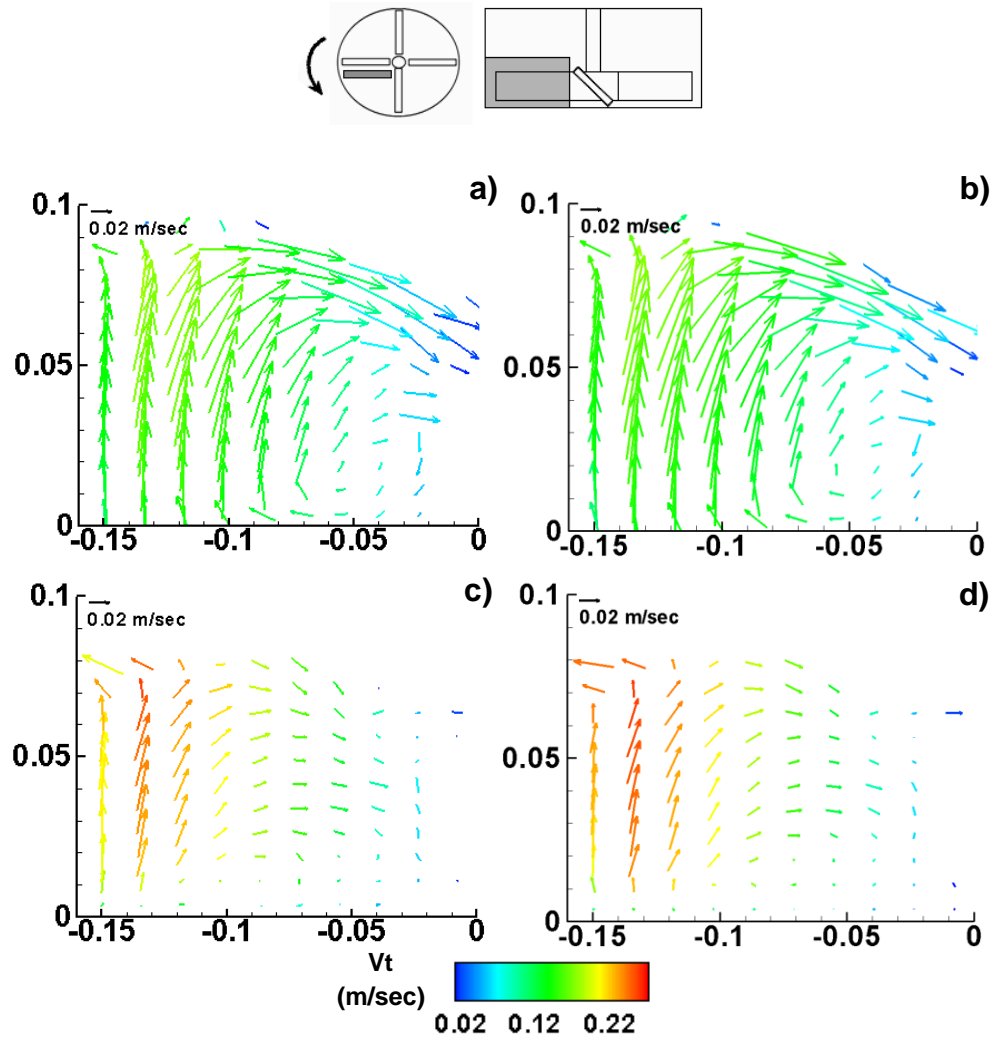


Fig. 5.1. Normalized time-averaged radial (V_r) and vertical (V_y) velocity fields in a vertical plane in front of the blade for different numbers of blades and D/d ratios: (a) 2 blades at $D/d = 63$, (b) 2 blades at $D/d = 90$, (c) 4 blades at $D/d = 63$, and (d) 4 blades at $D/d = 90$. The color bar indicates magnitude of the tangential velocity (V_t). Particle velocities are normalized relative to the tip speed of the blades (V_{tip}) for both D/d ratios. The schematic at the top of the figure shows the position of the vertical plane for the 4-blade configuration. An analogous vertical plane is used for the 2-bladed cases.

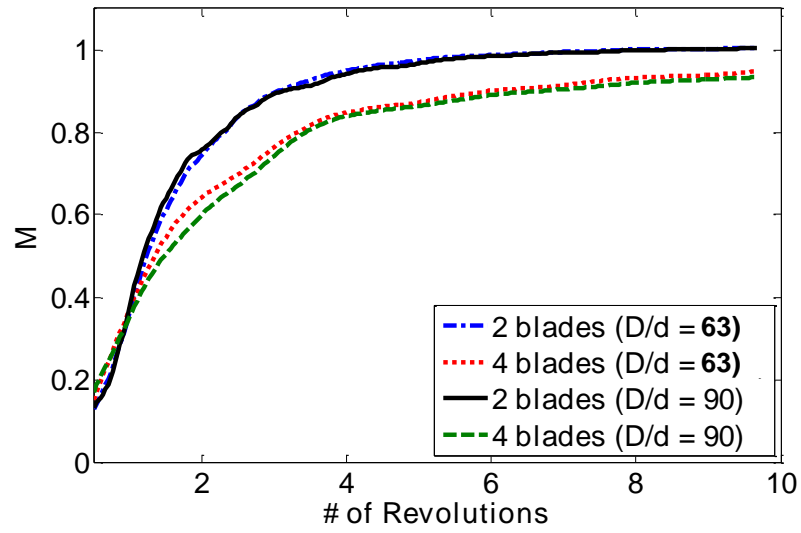


Fig. 5.2. Effect of different numbers of blades and D/d ratios on degree of mixing at 20 RPM. Lacey index (M) of the red particle concentrations vs. number of revolutions of the blades.

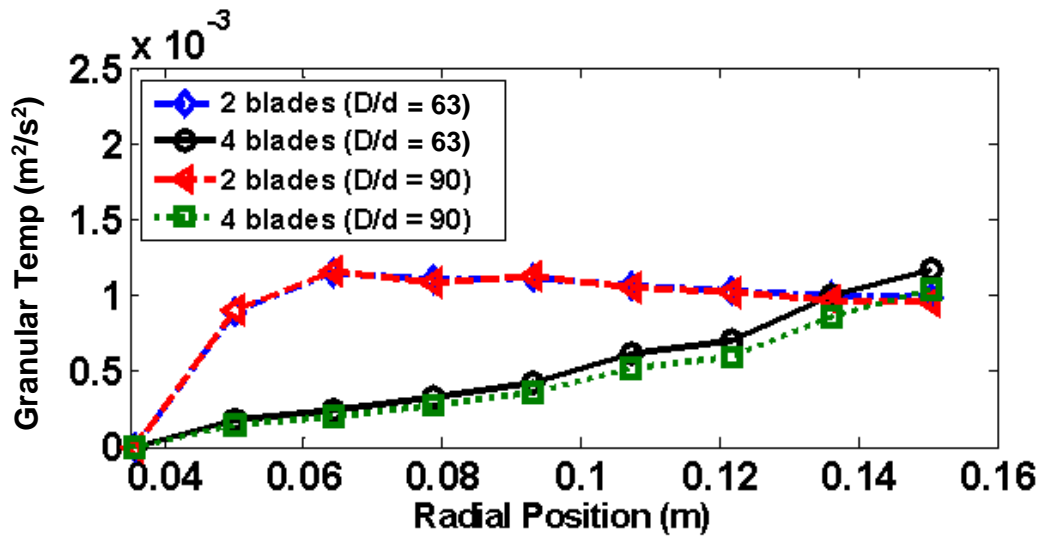


Fig. 5.3. Effect of different numbers of blades and D/d ratios on time-averaged granular temperature as a function of the radial position.

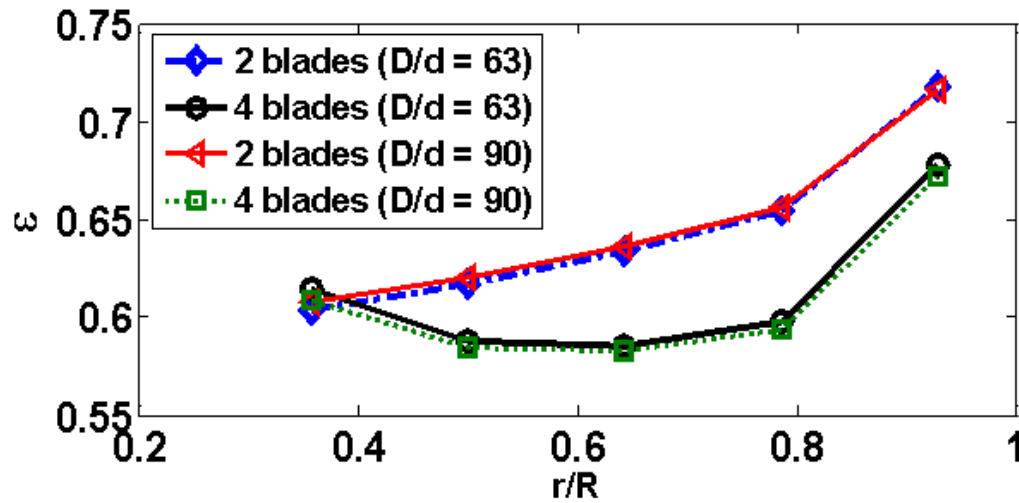


Fig. 5.4. Effect of different numbers of blades and D/d ratios on void fraction (ε) in front of the blade as a function of dimensionless radial position (r/R) in a mixer.

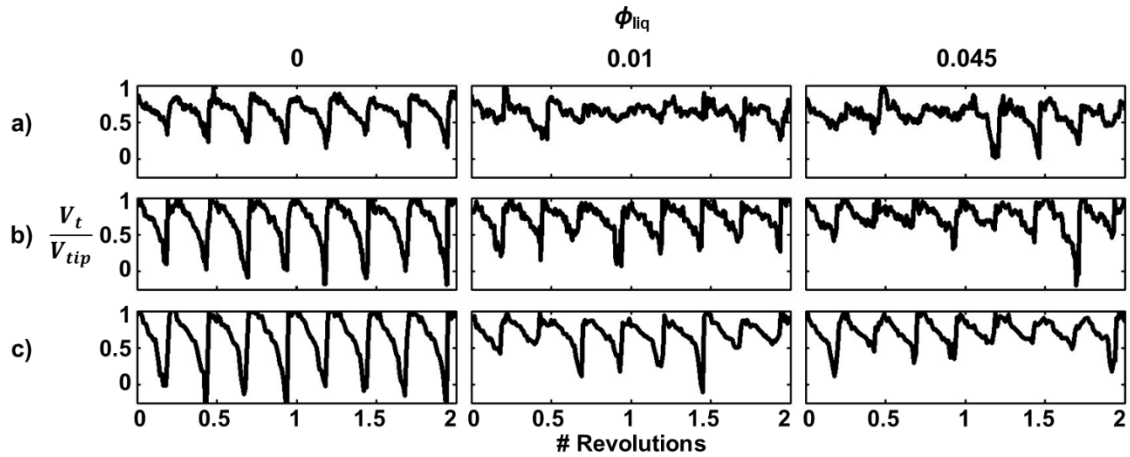


Fig. 5.5. Effect of D/d ratios and moisture content (ϕ_{liq}) on normalized tangential velocity (V_t/V_{tip}) profiles as a function of the number of revolutions of the impeller blade in cohesive granular systems: (a) $D/d = 50$, (b) $D/d = 75$, and (c) $D/d = 100$. Instantaneous tangential velocities (V_t) of particles at each time-step are normalized relative to the tip speed of the blades (V_{tip}) for all D/d ratios. Liquid volume fraction (ϕ_{liq}) in granular systems is examined at three levels: $\phi_{\text{liq}} = 0$ (dry), 0.01, and 0.045.

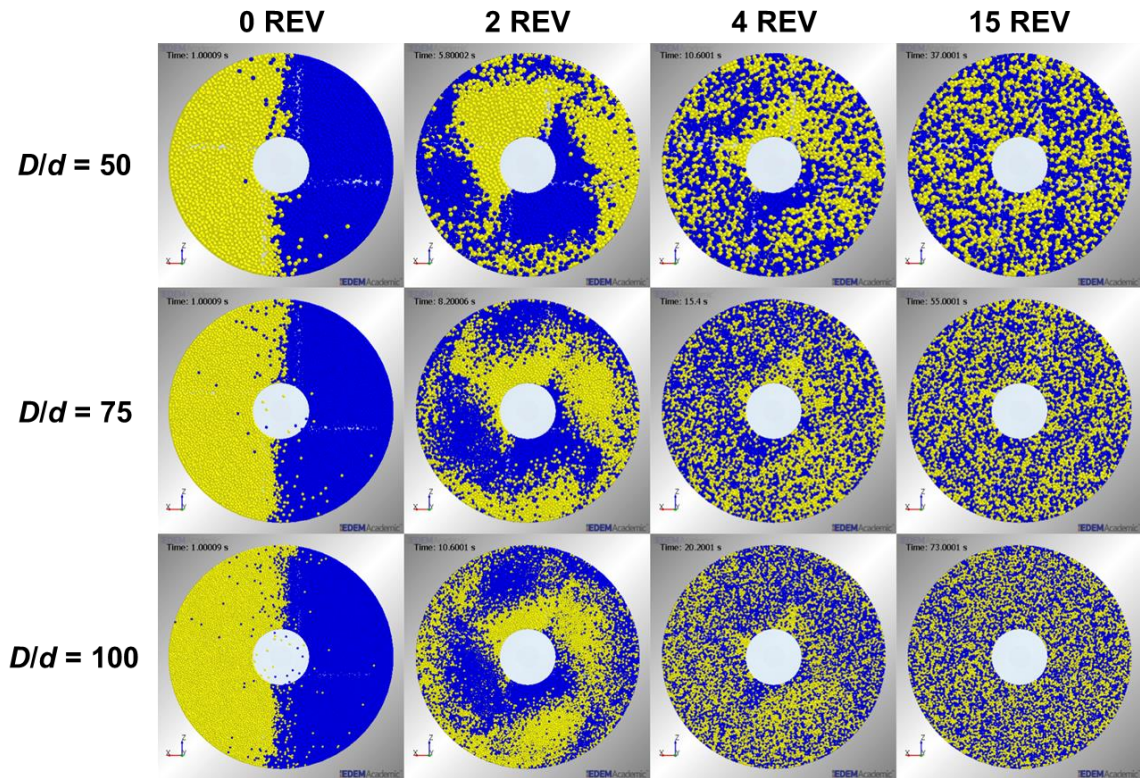


Fig. 5.6. Effect of D/d ratios on top-view snapshots of particles in cohesionless granular systems ($\phi_{liq} = 0$) showing mixing patterns as a function of the number of revolutions of the impeller blade at $V_{tip} = 0.589$ m/s.

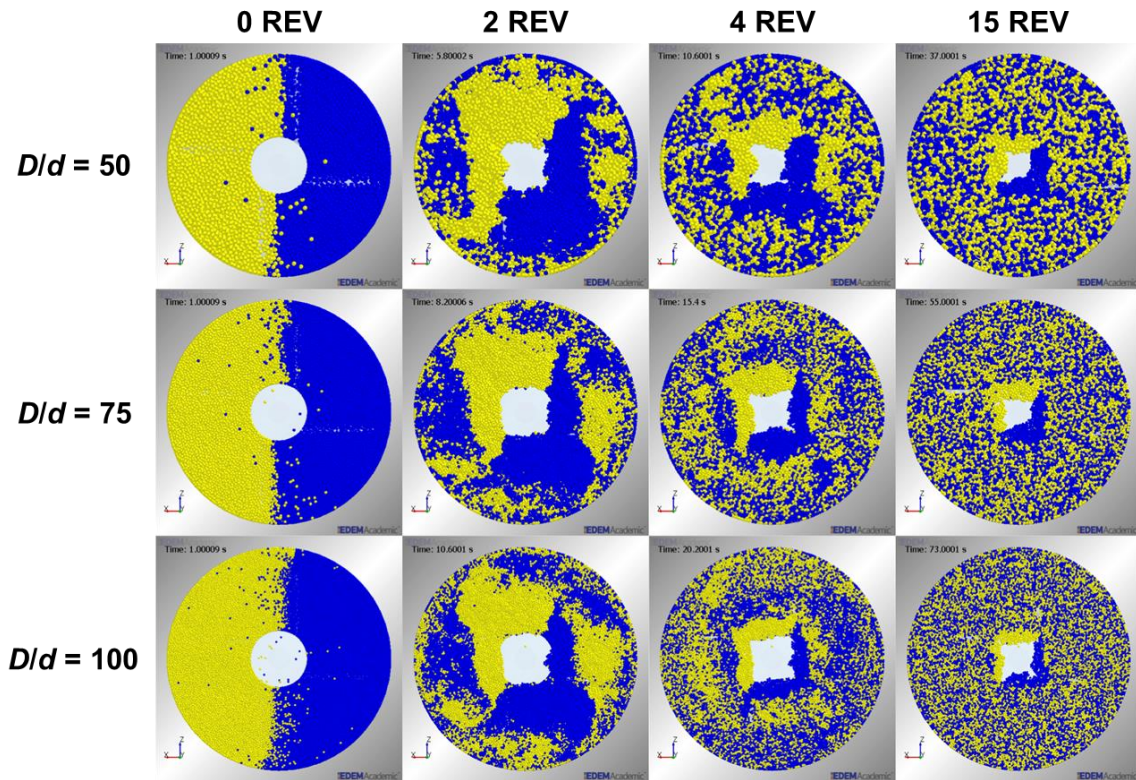


Fig. 5.7. Effect of D/d ratios on top-view snapshots of particles in cohesive granular systems (at $\phi_{\text{liq}} = 0.01$) showing mixing patterns as a function of the number of revolutions of the impeller blade at $V_{\text{tip}} = 0.589$ m/s.

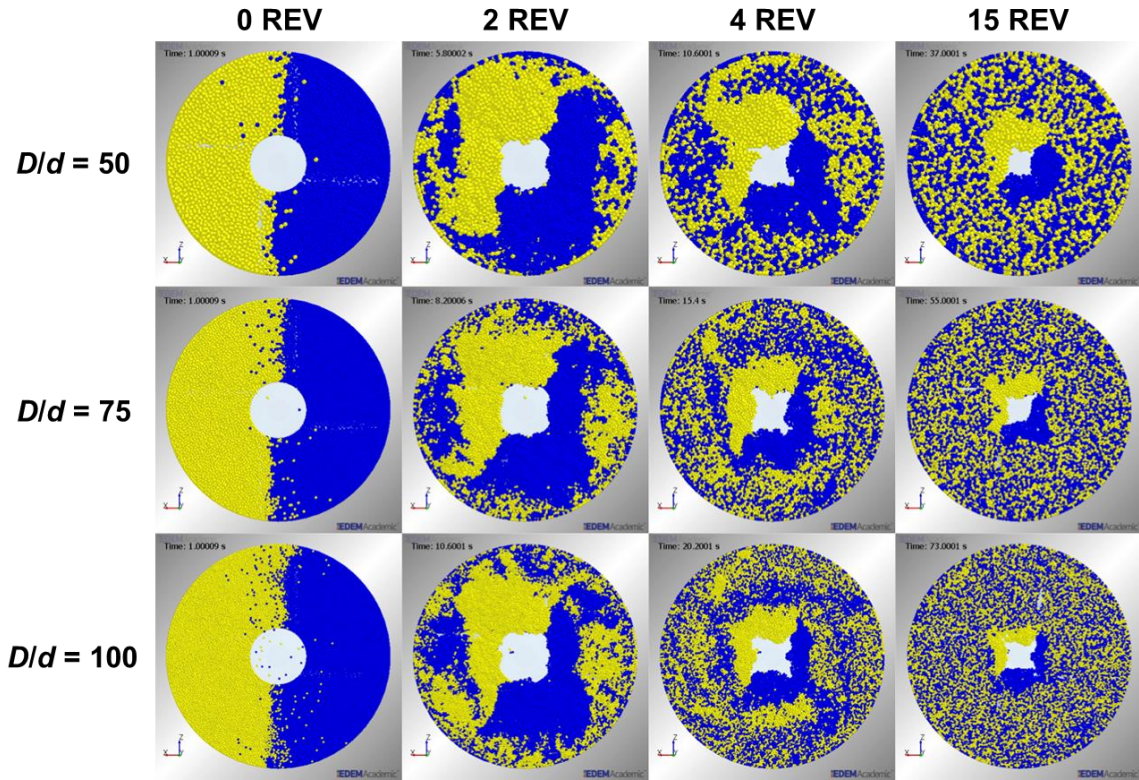


Fig. 5.8. Effect of D/d ratios on top-view snapshots of particles in cohesive granular systems (at $\phi_{\text{liq}} = 0.045$) showing mixing patterns as a function of the number of revolutions of the impeller blade at $V_{\text{tip}} = 0.589$ m/s.

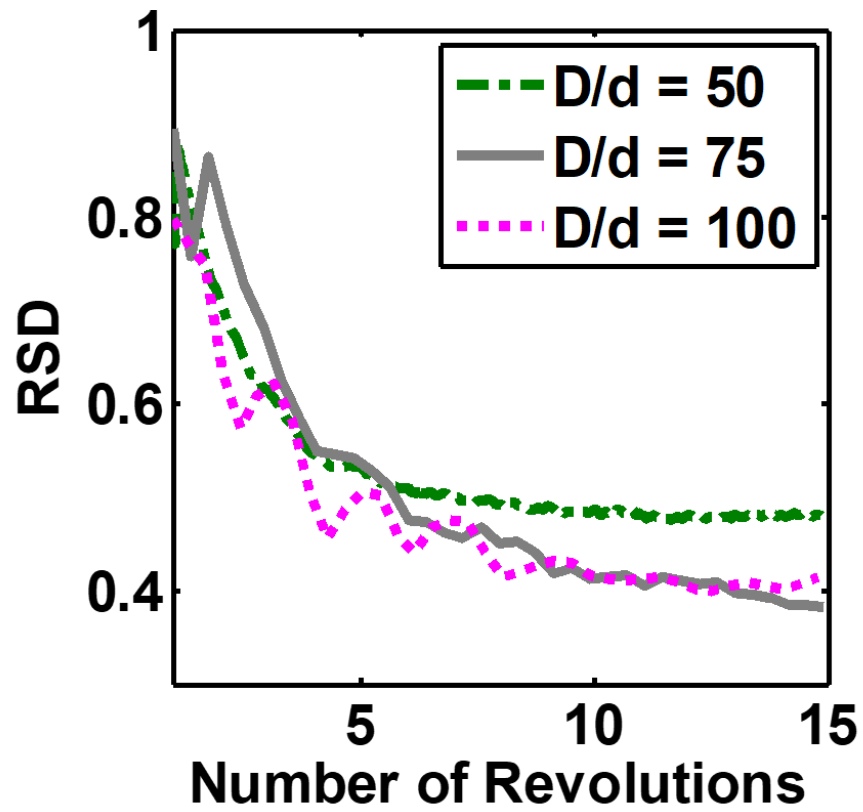


Fig. 5.9. Effect of D/d ratio on mixing kinetics in cohesionless granular systems ($\phi_{\text{liq}} = 0$) for $V_{\text{tip}} = 0.589$ m/s: relative standard deviation (RSD) of the blue particle concentration vs. the number of revolutions of the impeller blade.

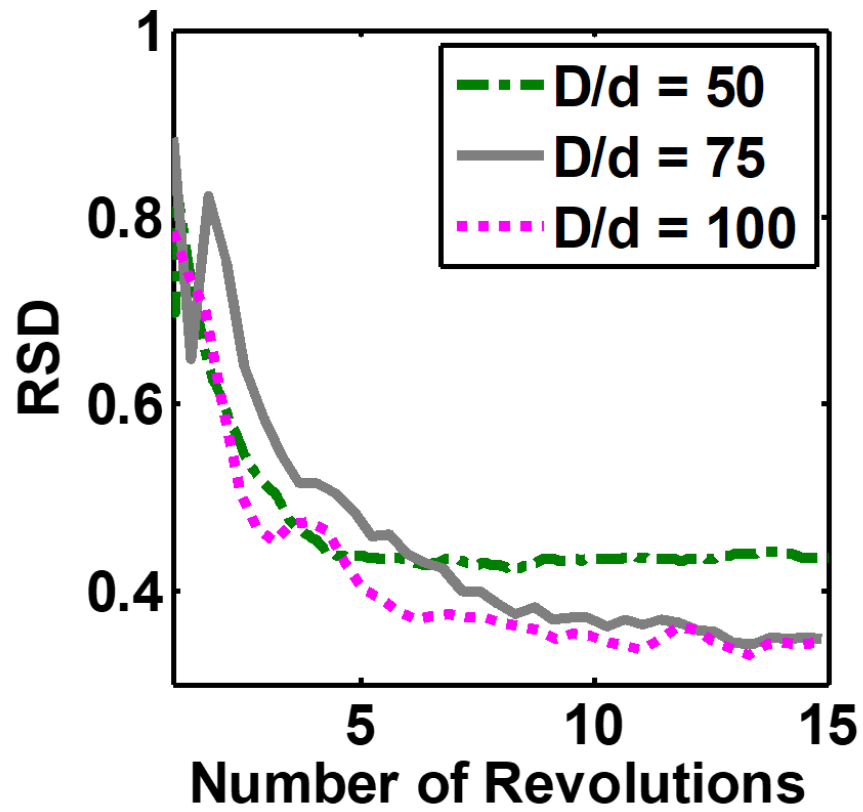


Fig. 5.10. Effect of D/d ratio on mixing kinetics in cohesive granular systems (at $\phi_{\text{liq}} = 0.01$) for $V_{\text{tip}} = 0.589$ m/s: relative standard deviation (RSD) of the blue particle concentration vs. the number of revolutions of the impeller blade.

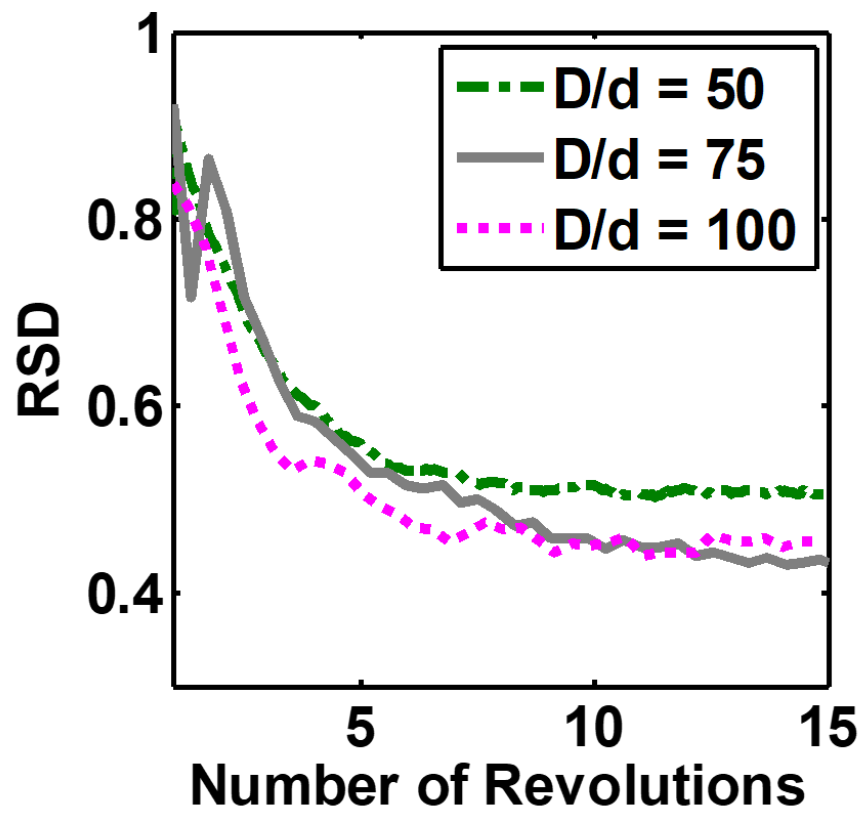


Fig. 5.11. Effect of D/d ratio on mixing kinetics in cohesive granular systems (at $\phi_{\text{liq}} = 0.045$) for $V_{\text{tip}} = 0.589$ m/s: relative standard deviation (RSD) of the blue particle concentration vs. the number of revolutions of the impeller blade.

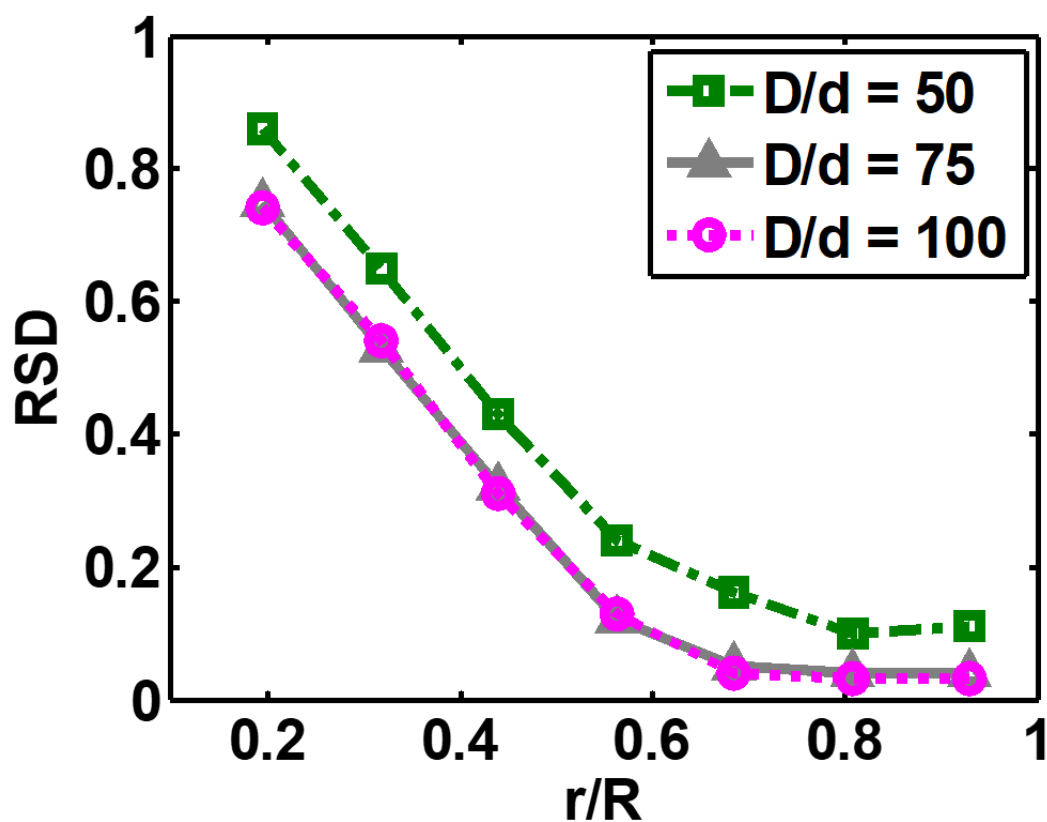


Fig. 5.12. Effect of D/d ratio on mixing performance in cohesionless granular systems ($\phi_{liq} = 0$) for $V_{tip} = 0.589$ m/s: relative standard deviation (RSD) of the blue particle concentration vs. dimensionless radial positions (r/R) after 15 revolutions of the impeller blade.

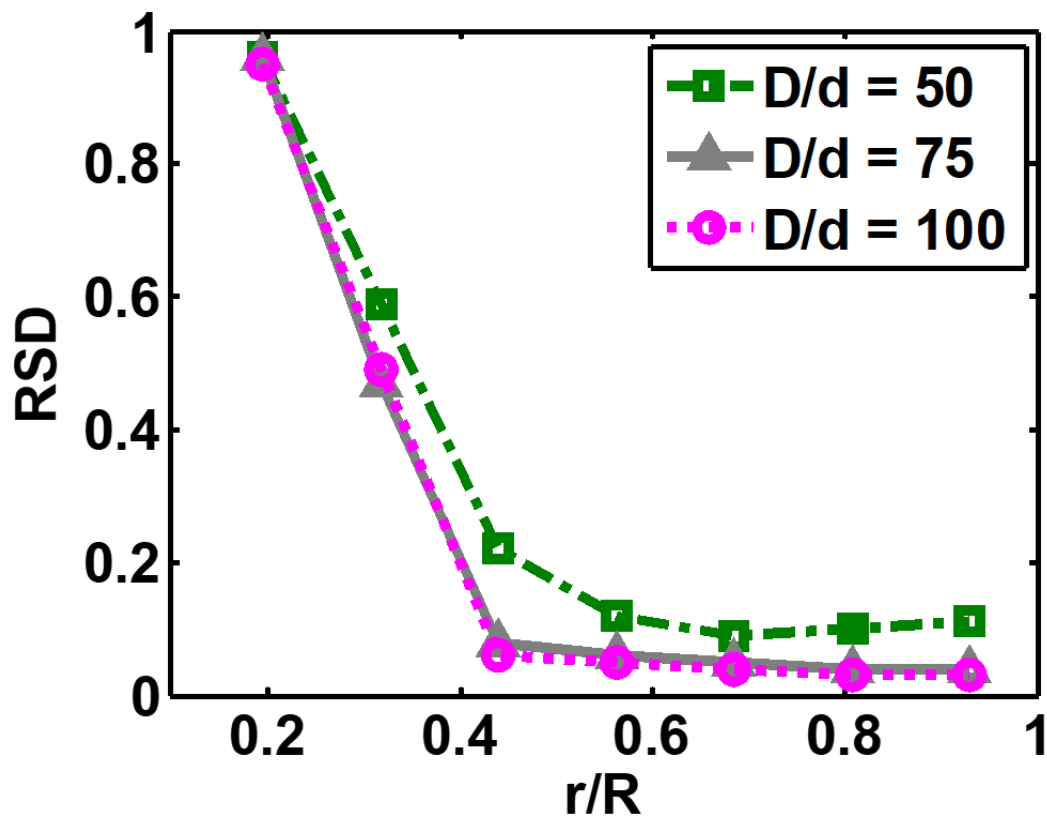


Fig. 5.13. Effect of D/d ratio on mixing performance in cohesive granular systems (at $\phi_{\text{liq}} = 0.01$) for $V_{\text{tip}} = 0.589$ m/s: relative standard deviation (RSD) of the blue particle concentration vs. dimensionless radial positions (r/R) after 15 revolutions of the impeller blade.

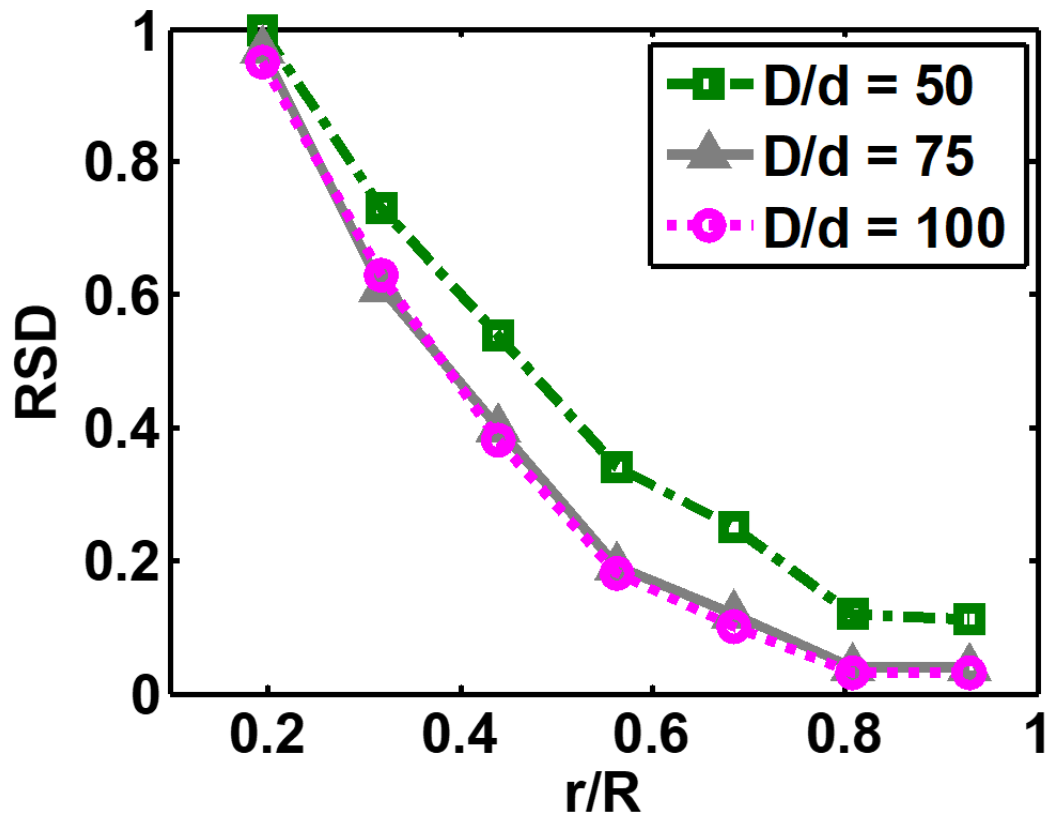


Fig. 5.14. Effect of D/d ratio on mixing performance in cohesive granular systems (at $\phi_{\text{liq}} = 0.045$) for $V_{\text{tip}} = 0.589$ m/s: relative standard deviation (RSD) of the blue particle concentration vs. dimensionless radial positions (r/R) after 15 revolutions of the impeller blade.

5.5 Tables for Chapter 5

Table 5.1. Effect of different numbers of blades and D/d ratio on normalized particle diffusivity (D_{ij}^*) and Péclet number (Pe_{ij}) in cohesionless granular systems. Particle diffusivities were computed with a Δt of $\frac{1}{4}$ of a revolution and were averaged over all the particles in the computational domain.

Blade # (D/d)	$D_{\theta\theta}^*$	D_{rr}^*	D_{yy}^*	$Pe_{\theta\theta}$	Pe_{rr}	Pe_{yy}
2 ($D/d = 63$)	1.2×10^{-2}	2.1×10^{-3}	2.5×10^{-3}	24	33	50
2 ($D/d = 90$)	1.3×10^{-2}	2.2×10^{-3}	2.5×10^{-3}	22	33	50
4 ($D/d = 63$)	1.0×10^{-2}	1.9×10^{-3}	1.7×10^{-3}	57	31	43
4 ($D/d = 90$)	0.9×10^{-2}	1.7×10^{-3}	1.7×10^{-3}	70	28	36

Table 5.2. Effect of D/d ratio and moisture content (ϕ_{liq}) on normalized particle diffusivities (D_{ij}^*) and Péclet number (Pe_{ij}) in cohesionless ($\phi_{\text{liq}} = 0$) and cohesive ($\phi_{\text{liq}} = 0.01$ and 0.045) granular systems. Particle diffusivities were computed with a Δt of $\frac{1}{4}$ of a revolution and were averaged over all the particles in the computational domain.

D/d	ϕ_{liq}	$D_{\theta\theta}^*$	D_{rr}^*	D_{yy}^*	$Pe_{\theta\theta}$	Pe_{rr}	Pe_{yy}
50	0.000	1.21×10^{-2}	5.63×10^{-3}	5.41×10^{-3}	23.95	4.80	6.63
	0.010	3.40×10^{-2}	9.56×10^{-3}	1.16×10^{-2}	7.02	2.45	3.55
	0.045	3.86×10^{-2}	1.06×10^{-2}	1.37×10^{-2}	6.39	2.13	2.69
75	0.000	4.02×10^{-3}	6.38×10^{-3}	5.92×10^{-3}	62.29	3.95	6.43
	0.010	5.20×10^{-3}	7.61×10^{-3}	1.13×10^{-2}	39.33	2.67	3.51
	0.045	5.08×10^{-3}	7.80×10^{-3}	1.20×10^{-2}	38.18	2.53	3.02
100	0.000	1.75×10^{-3}	4.04×10^{-3}	6.27×10^{-3}	119.93	6.31	7.13
	0.010	1.87×10^{-3}	4.06×10^{-3}	6.40×10^{-3}	91.58	5.31	7.22
	0.045	1.83×10^{-3}	4.05×10^{-3}	6.56×10^{-3}	87.93	5.00	5.78

Chapter 6. Conclusions and Future Work

Manufacture of commercial products including pharmaceutical solid dosage forms, powdered or granulated chemicals and foods, and other solid materials often involves significant particle processing. These solid particulate operations include storage and transfer of materials, mixing of ingredients, and processing from intermediates to finished products. Compared to fluid processing, our understanding of solids processing lags behind. Due to a lack of fundamental understanding of particulate systems, problems such as attrition, segregation, and agglomeration still occur during these processing steps. Furthermore, the roles of material properties, equipment configurations, and operational variables on the flow behaviors of the particulate systems remain unclear. In this dissertation, we have both computationally and experimentally studied cohesionless and cohesive granular flows in bladed mixers to obtain a better understanding of the particle dynamics and mixing kinetics of the systems.

Simulations of granular flow of monodisperse, cohesionless spherical glass beads in a cylindrical bladed mixer agitated by an impeller were performed using the discrete element method (DEM). The number of impeller blades was varied from 1 to 4 blades, and the impact of the number of blades on granular flow and mixing kinetics was investigated. It was found that particle velocities were influenced by the number of the blades used in the mixing system. Higher radial and vertical velocities of particles were observed in the 1- and 2-bladed mixers, which led to more pronounced three-dimensional recirculation patterns. However, the tangential velocity components of particles in the 3-

and 4-bladed cases were larger. Additionally, it was found that using two or three impeller blades provided better mixing performance than using one or four blades, as evaluated by calculation of the relative standard deviation (RSD) and the Lacey index of the systems. Granular temperature and particle diffusivities obtained for the 2- and 3-bladed cases were also higher than those for the 1- and 4-bladed mixers. Solids fraction analysis showed that dilation of the particle bed occurred to the greatest extent in the 2-bladed mixer. Contact force network data and blade-particle force calculations showed that using different numbers of impeller blades led to significant differences in the force distribution.

The torque and power needed to drive an impeller are important quantities that can indicate flow behavior and can be used to control processes, especially mixing and granulation in the pharmaceutical industry. In this study, experiments were conducted on monodisperse spherical glass beads flowing in a cylindrical bladed mixer agitated by an impeller. The impeller torque was measured using a rotating platform, and the power draw for the motor driving the impeller was measured using a power meter. The effect of various impeller blade designs and material properties on the torque and power were investigated as a function of the impeller blade rotation rate. It was found that the torque exerted on a granular bed and the power consumption were a strong function of the impeller blade configuration, the position of the blades in a deep granular bed, the fill height of the glass beads, and the size and friction coefficient of the particles. It was observed that the time-averaged torque and power consumption for different particle sizes qualitatively scaled with particle diameter. A scale-up relationship for a deep

granular bed was developed: the time-averaged torque and average adjusted power consumption scaled with the square of the material fill height.

The effect of scaling up cohesionless monodisperse spherical particulate systems based on the number of the impeller blades (2 and 4 blades) used in the blending process was evaluated by varying the mixer diameter to particle diameter (D/d) ratio. Cases utilizing 2 and 4 impeller blades at both D/d ratios equal to 63 and 90 exhibited similar characteristics in terms of velocity fields, degree of mixing, granular temperature, particle diffusivities, and void fraction of the particle bed. Increasing the D/d ratio of the systems from 63 to 90 was found to have little impact on dry particle flows and mixing behaviors for 2- and 4-bladed mixers. Scale-up of non-cohesive granular systems based on the number of impeller blades (2 and 4 blades) used in the agitated mixer could be scaled by the diameter of the mixer and the rotational speed of the impeller blades within the range from $D/d = 63$ to 90. In addition to the cohesionless particulate systems, we also performed scale-up of cohesive granular flows in four-bladed mixers with D/d ratios of 50, 75, and 100 at different moisture content levels ($\phi_{\text{liq}} = 0.01$ and 0.045) and then compared particle dynamics and mixing rates to the dry cases ($\phi_{\text{liq}} = 0$). It was observed that at each level of cohesion, normalized tangential velocity profiles, mixing performance, and normalized particle convection were comparable between the $D/d = 75$ and the $D/d = 100$ cases. It was observed that, above a specific system size ($D/d \geq 75$ in our case), particle dynamics and degree of mixing scaled with the diameter of the mixers and the tip speed of the impeller blades. Although there was an impact of cohesion that caused some differences between system sizes, wet granular flows in bladed mixers could

be scaled by the diameter of a mixer and the tip speed of the impeller blades within the range of D/d ratio from 75 to 100.

The results found in this dissertation provide insight into how the impeller blade configuration, particle properties, and process parameters affect cohesionless and cohesive granular flow behaviors and mixing performance in bladed mixers for small and larger scales. These findings complement our preceding knowledge and grant better understanding with regard to the processing of particulate systems. However, at the same time these results are for a limited number of parameters, and additional work is needed to confirm that the results of this study hold for other parameter values. Further computational and experimental investigations are thus needed to confirm the results of this work.

Further research is needed to study the effect of other process parameters (such as heat transfer for agitated drying), material properties (such as particle polydispersity, higher moisture content including intermediate (funicular) or high (capillary) moisture content regimes), or different equipment designs/types on flow behaviors and performance of mixing operations in bladed mixers. Further work is needed to investigate the effect of the impeller blade rotational rate (or shear rate) on wet granular flow behaviors and mixing kinetics in numerical simulations when particulate flow regime transition occurs, i.e., passing beyond the quasi-static to the intermediate regime. As an extension, scale-up of cohesive granular systems can be achieved by increasing the fill height of materials (H/D ratio) while keeping the mixer diameter constant. Importantly, numerical results

acquired from DEM computational simulations can be validated by additional experimental data.

For experiments, the effects of other parameters (e.g. other equipment designs/types, particle polydispersity, higher percentage of moisture content, etc.) on the agitation torque and power draw can be further investigated. The impeller torque and power consumed should be examined in scaled-up (larger D/d) bladed mixers to compare with smaller systems. Moreover, experimental measurements of torque and power in cohesive granular materials can be carried out in deeper beds (higher H/D ratio) to reduce variations of data. The experimental results on torque and power can be compared with DEM simulation results in similar mixer geometries. Our findings on how the experimentally measured impeller torque and the power consumption depended upon material properties, equipment configurations, and blade rotational speed can be incorporated with heat transfer and applied to study the agitated drying process of active pharmaceutical ingredients (API) in agitated filtered bed dryers.

Appendix

There are several methodologies that can be used to verify the accuracy of a DEM model. Two different experimental techniques have been extensively used to examine particle flows in agitated blenders and validate results from the discrete element method, namely particle image velocimetry (PIV) and positron emission particle tracking (PEPT). PIV records the positions of particles at a top free surface and near a transparent wall of a mixer allowing for the characterization of flow fields and the determination of particle trajectories. The PEPT technique enables the visualization of three-dimensional flow patterns of particles by following radioactive tracers inserted within a particle bed. Other methods such as sampling and imaging techniques have been used to quantify the degree of mixing of solid particles in blenders and confirm results obtained from numerical simulations [53].

To validate the DEM simulations in this study, we conducted experiments using the PIV technique to measure velocities of 2-mm glass beads in a 4-bladed mixer. We performed DEM simulations in a mixer of the same dimensions and with the same particle size. We previously showed that similar flow patterns and general trends were obtained for DEM simulations in a 4-bladed mixer with glass beads with diameters within the range of 2 – 10 mm [27]. In particular, the change in particle size did not have a significant effect on the velocity profiles and the flow patterns observed [27]. Instantaneous velocity profiles at the top free surface of the granular bed and through the transparent side walls were obtained at 50 RPM for the PIV experiments and the DEM simulations. The velocity

components were normalized by the tip speed of the blades, V_{tip} . For both experiments and simulations, a $1 \times 1 \text{ cm}^2$ control area was generated at the top free surface at $r/R = 0.5$ and at the cylinder wall at $y/H = 0.5$. The instantaneous velocity components were computed by averaging over the control area at a specific time. The DEM simulation results are compared to the PIV experimental data in Fig. A1. Generally, there is a good agreement between the experimental instantaneous velocities obtained from PIV and the simulation results obtained from DEM. In particular, the minimum and maximum velocities and magnitude of fluctuations are similar in all cases. The experimental data shown here serves to validate the DEM model used in this work.

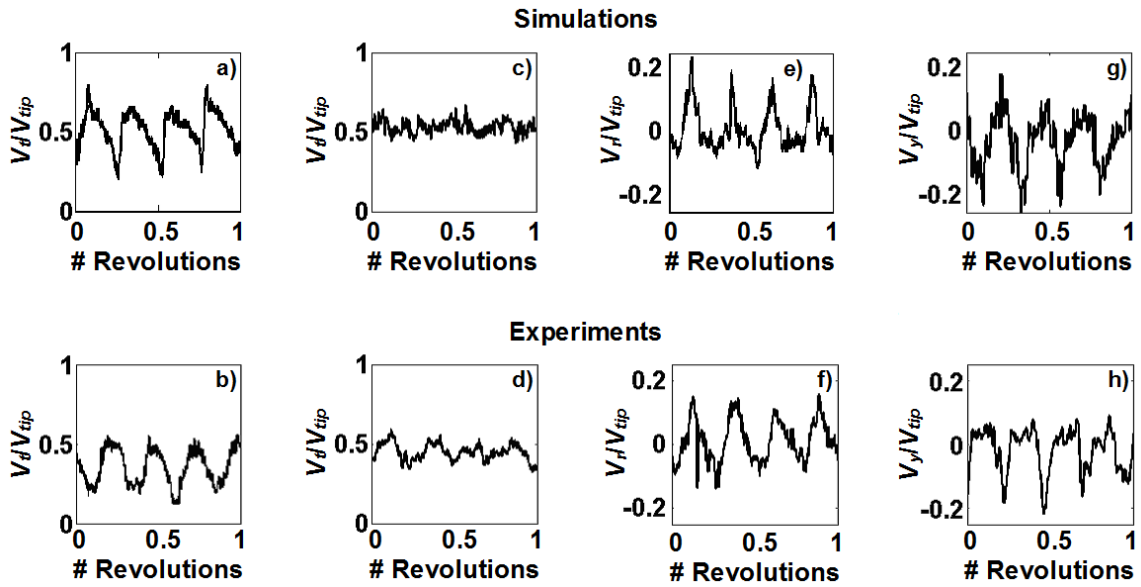


Fig. A1. Comparisons between DEM computational results and PIV experimental data for normalized velocity fluctuations near top free surface at $r/R = 0.5$ and by the cylinder walls at $y/H = 0.5$. All results shown are for a blade rotational speed of 50 RPM. (a) and (b): top free surface normalized tangential velocity (V_t/V_{tip}); (c) and (d): cylinder wall normalized tangential velocity (V_t/V_{tip}); (e) and (f): top free surface normalized radial velocity (V_r/V_{tip}); and (g) and (h): cylinder wall normalized vertical velocity (V_y/V_{tip}).

Notations

List of Variables:

Bo_g	granular Bond number (-)
Ca	capillary number (-)
d	diameter of particles (m)
D	diameter of a mixer (m)
D/d	mixer diameter to particle diameter ratio (-)
D_{ij}	diffusion coefficient in i direction due to a gradient in j direction (m ² /s)
D_{ij}^*	normalized diffusion coefficient (-)
e	coefficient of restitution (-)
E	Young's modulus (Pa)
f	frequency of torque signals (Hz)
\vec{F}	force that a lever arm exerts on a load cell (N)
F_r	radial component of the blade-particle contact force (N)
F_t	tangential component of the blade-particle contact force (N)
F_y	vertical component of the blade-particle contact force (N)
F^C	capillary force due to the liquid bridge formation (N)
F_{ij}^C	cohesive force experienced by particle i with particle j (N)
F_{ij}^N	normal force resulting from the contact of particle i with particle j (N)
F_{ij}^T	tangential force resulting from the contact of particle i with particle j (N)
\hat{F}^C	normalized capillary force (-)
g	gravitational acceleration (m/s ²)

G	shear modulus (Pa)
h	separation distance between two surfaces (m)
h_c	critical rupture or separation distance of the liquid bridge (m)
\hat{h}	dimensionless separation distance between two surfaces (-)
\hat{h}_c	dimensionless critical rupture distance (-)
H	fill height of particle bed (m)
H/D	material fill height to mixer diameter ratio (-)
I_i	moment of inertia of particle i ($\text{kg}\cdot\text{m}^2$)
\tilde{k}_n	normal stiffness coefficient (-)
\tilde{k}_t	tangential stiffness coefficient (-)
ℓ	length of a lever arm (m)
L	length of blades (m)
m	mass of particle bed (kg)
m_i	mass of particle i (kg)
m_s	number of samples (-)
M	Lacey index of particle concentration (-)
M_{conc}	mean particle concentration ($\text{particles}/\text{m}^3$ or kg/m^3)
N	number of particles in simulations or experiments (-)
p, q	proportions of two components in a binary mixture (-)
p_i	proportion of one component in the i th sample (-)
P	normal stress (Pa)
P	actual power (W)
P_{emp}	power measured from an empty mixer (W)

P^*	adjusted power (W)
ΔP	pressure difference across the air-fluid interface (Pa)
Pe_{ij}	Péclet number (-)
r	radial position in a mixer (m)
R or R_i	radius of particles or particle i (m)
R_{cyl}	radius of a mixer (m)
R^*	effective radius of the colliding particles (m)
RSD	relative standard deviation of particle concentration (-)
t	time (s)
Δt	particle diffusion time (s)
T	granular temperature (m^2/s^2)
\vec{T}	instantaneous torque at each time step ($N \cdot m$)
$\langle \vec{T} \rangle$	time-averaged torque ($N \cdot m$)
\vec{T}^*	normalized torque (-)
u'	fluctuation velocity (m/s)
U	characteristic velocity (m/s)
U_i	average particle speed in the i direction (m/s)
v_i	linear velocity of particle i (m/s)
v_{rel}^t	relative tangential velocity of the colliding particles (m/s)
V	volume of the liquid bridge (m^3)
V_C	size (volume) of the control volume (m^3)
V_p	volume of a particle (m^3)
V_r	radial velocity of particles (m/s)

V_t	tangential velocity of particles (m/s)
V_{tip}	tip speed of blades (m/s), where $V_{tip} = \omega L$
V_t^*	tangential velocity of particles normalized by the tip speed (-)
V_y	vertical velocity of particles (m/s)
\hat{V}	dimensionless liquid bridge volume (-)
W	work done by impeller blades (J)
Δx_i	particle displacement in i direction relative to particle's initial position (m)
$\overline{\Delta x_i}$	mean particle displacement in the i direction (m)

List of Subscripts:

0, 1, 2	subscripts for D and H in Tables 2.1, 2.4, and 2.6 which denote each part of the schematic in Fig. 2.2 of Chapter 2
---------	---

List of Greek Letters:

β	half filling angle of liquid on particles ($^\circ$)
γ	surface tension of liquid (N/m)
γ°	shear rate (s^{-1})
γ^*	dimensionless shear rate (-)
$\tilde{\gamma}_n$	normal damping coefficient (-)
$\tilde{\gamma}_t$	tangential damping coefficient (-)
δ_n	normal displacement (m)
δ_t	tangential displacement (m)
ε	void fraction (-)

η	dynamic viscosity of liquid (Pa·s)
θ	contact angle of liquid on particles (°)
μ	macroscopic/bulk friction coefficient (-)
μ_r	rolling friction coefficient (-)
μ_s	sliding friction coefficient (-)
ρ_{bulk}	bulk density of particle bed (kg/m ³)
ρ_{liq}	density of liquid or water (kg/m ³)
ρ_p	density of particles (kg/m ³)
σ	Poisson's ratio (-)
σ_{conc}	standard deviation of particle concentration (particles/m ³ or kg/m ³)
σ_0^2	variance of an initial completely segregated state
σ_r^2	variance of a fully random or perfectly mixed state
σ^2	actual variance obtained from mixing process
τ	shear stress (Pa)
τ_{rij}	stress resulting from the contact of particle i with particle j (Pa)
$\langle \tau_{\theta r} \rangle$	time-averaged shear stress (Pa)
ϕ	solids fraction (-)
ϕ_{liq}	volume fraction of liquid (-)
ω	angular velocity of impeller blades (rad/s)
ω_i	angular velocity of particle i (rad/s)

References

- [1] J. Bridgwater, The dynamics of granular materials – towards grasping the fundamentals, *Granular Matter*, 4 (2003) 175-181.
- [2] T. Shinbrot, K. LaMarche, B.J. Glasser, Triboelectrification and razorbacks: Geophysical patterns produced in dry grains, *Physical Review Letters*, 96 (2006) 178002-178004.
- [3] F.J. Muzzio, A. Alexander, C. Goodridge, E. Shen, T. Shinbrot, Solids Mixing Part A: Fundamentals of Solids Mixing, in: E.L. Paul, V.A. Atiemo-Obeng, S.M. Kresta (Eds.) *Handbook of Industrial Mixing: Science and Practice*, John Wiley & Sons, Inc., 2004, pp. 887-985.
- [4] D. Geldart, Powder Processing - The Overall View, in: M.J. Rhodes (Ed.) *Principles of Powder Technology*, Wiley, Chichester; New York, 1990, pp. 1-7.
- [5] J.D. Litster, K.P. Hapgood, J.N. Michaels, A. Sims, M. Roberts, S.K. Kameneni, Scale-up of mixer granulators for effective liquid distribution, *Powder Technology*, 124 (2002) 272-280.
- [6] D. Mateo-Ortiz, R. Méndez, Relationship between residence time distribution and forces applied by paddles on powder attrition during the die filling process, *Powder Technology*, 278 (2015) 111-117.
- [7] M.J. Metzger, B. Remy, B.J. Glasser, All the Brazil nuts are not on top: vibration induced granular size segregation of binary, ternary and multi-sized mixtures, *Powder Technology*, 205 (2011) 42-51.
- [8] C.L. Hare, M. Ghadiri, Influence of measurement cell size on predicted attrition by the distinct element method, *Powder Technology*, 236 (2013) 100-106.
- [9] C. Hare, M. Ghadiri, R. Dennehy, Prediction of attrition in agitated particle beds, *Chemical Engineering Science*, 66 (2011) 4757-4770.
- [10] T. Lee, J. Lee, Particle attrition by particle-surface friction in dryers, *Pharmaceutical Technology*, 27 (2003) 64-72.
- [11] M. Capece, R.N. Davé, E. Bilgili, On the origin of non-linear breakage kinetics in dry milling, *Powder Technology*, 272 (2015) 189-203.
- [12] Y. Guo, C. Wassgren, B. Hancock, W. Ketterhagen, J. Curtis, Predicting breakage of high aspect ratio particles in an agitated bed using the Discrete Element Method, *Chemical Engineering Science*, 158 (2017) 314-327.

- [13] A. Lekhal, K.P. Girard, M.A. Brown, S. Kiang, B.J. Glasser, J.G. Khinast, Impact of agitated drying on crystal morphology: KCl–water system, *Powder Technology*, 132 (2003) 119-130.
- [14] A. Lekhal, K.P. Girard, M.A. Brown, S. Kiang, J.G. Khinast, B.J. Glasser, The effect of agitated drying on the morphology of l-threonine (needle-like) crystals, *International Journal of Pharmaceutics*, 270 (2004) 263-277.
- [15] D.F. Bagster, J. Bridgwater, The measurement of the force needed to move blades through a bed of cohesionless granules, *Powder Technology*, 1 (1967) 189-198.
- [16] D.F. Bagster, J. Bridgwater, The flow of granular material over a moving blade, *Powder Technology*, 3 (1969) 323-338.
- [17] R.L. Stewart, J. Bridgwater, D.J. Parker, Granular flow over a flat-bladed stirrer, *Chemical Engineering Science*, 56 (2001) 4257-4271.
- [18] S.L. Conway, A. Lekhal, J.G. Khinast, B.J. Glasser, Granular flow and segregation in a four-bladed mixer, *Chemical Engineering Science*, 60 (2005) 7091-7107.
- [19] A. Lekhal, S.L. Conway, B.J. Glasser, J.G. Khinast, Characterization of granular flow of wet solids in a bladed mixer, *AIChE Journal*, 52 (2006) 2757-2766.
- [20] R.L. Stewart, J. Bridgwater, Y.C. Zhou, A.B. Yu, Simulated and measured flow of granules in a bladed mixer—a detailed comparison, *Chemical Engineering Science*, 56 (2001) 5457-5471.
- [21] Y.C. Zhou, A.B. Yu, J. Bridgwater, Segregation of binary mixture of particles in a bladed mixer, *Journal of Chemical Technology and Biotechnology*, 78 (2003) 187-193.
- [22] Y.C. Zhou, A.B. Yu, R.L. Stewart, J. Bridgwater, Microdynamic analysis of the particle flow in a cylindrical bladed mixer, *Chemical Engineering Science*, 59 (2004) 1343-1364.
- [23] B. Remy, J.G. Khinast, B.J. Glasser, Discrete element simulation of free flowing grains in a four-bladed mixer, *AIChE Journal*, 55 (2009) 2035-2048.
- [24] B. Remy, B.J. Glasser, J.G. Khinast, The effect of mixer properties and fill level on granular flow in a bladed mixer, *AIChE Journal*, 56 (2010) 336-353.
- [25] J. Havlica, K. Jirounkova, T. Travnickova, M. Kohout, The effect of rotational speed on granular flow in a vertical bladed mixer, *Powder Technology*, 280 (2015) 180-190.

- [26] B. Remy, W. Kightlinger, E.M. Saurer, N. Domagalski, B.J. Glasser, Scale-up of agitated drying: effect of shear stress and hydrostatic pressure on active pharmaceutical ingredient powder properties, *AIChE Journal*, 61 (2015) 407-418.
- [27] B. Remy, T.M. Canty, J.G. Khinast, B.J. Glasser, Experiments and simulations of cohesionless particles with varying roughness in a bladed mixer, *Chemical Engineering Science*, 65 (2010) 4557-4571.
- [28] B. Remy, J.G. Khinast, B.J. Glasser, Polydisperse granular flows in a bladed mixer: experiments and simulations of cohesionless spheres, *Chemical Engineering Science*, 66 (2011) 1811-1824.
- [29] B. Remy, J.G. Khinast, B.J. Glasser, Wet granular flows in a bladed mixer: experiments and simulations of monodisperse spheres, *AIChE Journal*, 58 (2012) 3354-3369.
- [30] C. Hare, U. Zafar, M. Ghadiri, T. Freeman, J. Clayton, M.J. Murtagh, Analysis of the dynamics of the FT4 powder rheometer, *Powder Technology*, (2015).
- [31] U. Zafar, C. Hare, A. Hassanpour, M. Ghadiri, Drop test: a new method to measure the particle adhesion force, *Powder Technology*, 264 (2014) 236-241.
- [32] R. Chandratilleke, A. Yu, J. Bridgwater, K. Shinohara, Flow and mixing of cohesive particles in a vertical bladed mixer, *Industrial & Engineering Chemistry Research*, 53 (2014) 4119-4130.
- [33] G.I. Tardos, S. McNamara, I. Talu, Slow and intermediate flow of a frictional bulk powder in the Couette geometry, *Powder Technology*, 131 (2003) 23-39.
- [34] C.S. Campbell, Granular shear flows at the elastic limit, *Journal of Fluid Mechanics*, 465 (2002) 261-291.
- [35] L. Srinivasa Mohan, K. Kesava Rao, P.R. Nott, A frictional Cosserat model for the slow shearing of granular materials, *Journal of Fluid Mechanics*, 457 (2002) 377-409.
- [36] C.S. Campbell, C.E. Brennen, Computer simulation of granular shear flows, *Journal of Fluid Mechanics*, 151 (1985) 167-188.
- [37] R. Jackson, Some features of the flow of granular materials and aerated granular materials, *Journal of Rheology*, 30 (1986) 907-930.
- [38] D.G. Schaeffer, Instability in the evolution equations describing incompressible granular flow, *Journal of Differential Equations*, 66 (1987) 19-50.
- [39] S.B. Savage, Analyses of slow high-concentration flows of granular materials, *Journal of Fluid Mechanics*, 377 (1998) 1-26.

- [40] S.R. Dahl, C.M. Hrenya, Size segregation in gas–solid fluidized beds with continuous size distributions, *Chemical Engineering Science*, 60 (2005) 6658-6673.
- [41] J. Havlica, K. Jirounkova, T. Travnickova, M. Kohout, The effect of rotational speed on granular flow in a vertical bladed mixer, *Powder Technology*, 280 (2015) 180-190.
- [42] S. Radl, E. Kalvoda, B.J. Glasser, J.G. Khinast, Mixing characteristics of wet granular matter in a bladed mixer, *Powder Technology*, 200 (2010) 171-189.
- [43] S. Oka, O. Kašpar, V. Tokárová, K. Sowrirajan, H. Wu, M. Khan, F. Muzzio, F. Štěpánek, R. Ramachandran, A quantitative study of the effect of process parameters on key granule characteristics in a high shear wet granulation process involving a two component pharmaceutical blend, *Advanced Powder Technology*, 26 (2015) 315-322.
- [44] E.W. Conder, A.S. Cosbie, J. Gaertner, W. Hicks, S. Huggins, C.S. MacLeod, B. Remy, B.-S. Yang, J.D. Engstrom, D.J. Lamberto, C.D. Papageorgiou, The pharmaceutical drying unit operation: An industry perspective on advancing the science and development approach for scale-up and technology transfer, *Organic Process Research and Development*, 21 (2017) 420-429.
- [45] M. Ebrahimi, E. Siegmund, D. Prieling, B.J. Glasser, J.G. Khinast, An investigation of the hydrodynamic similarity of single-spout fluidized beds using CFD-DEM simulations, *Advanced Powder Technology*, 28 (2017) 2465-2481.
- [46] A. Chaudhury, A. Niziolek, R. Ramachandran, Multi-dimensional mechanistic modeling of fluid bed granulation processes: An integrated approach, *Advanced Powder Technology*, 24 (2013) 113-131.
- [47] Y. Sato, H. Nakamura, S. Watano, Numerical analysis of agitation torque and particle motion in a high shear mixer, *Powder Technology*, 186 (2008) 130-136.
- [48] Y. Wang, T. Li, F.J. Muzzio, B.J. Glasser, Predicting feeder performance based on material flow properties, *Powder Technology*, 308 (2017) 135-148.
- [49] E. Alizadeh, F. Bertrand, J. Chaouki, Comparison of DEM results and Lagrangian experimental data for the flow and mixing of granules in a rotating drum, *AIChE Journal*, 60 (2014) 60-75.
- [50] P. Tahvildarian, F. Ein-Mozaffari, S.R. Upreti, Circulation intensity and axial dispersion of non-cohesive solid particles in a V-blender via DEM simulation, *Particuology*, 11 (2013) 619-626.
- [51] E. Alizadeh, F. Bertrand, J. Chaouki, Discrete element simulation of particle mixing and segregation in a tetrapodal blender, *Computers & Chemical Engineering*, 64 (2014) 1-12.

- [52] M. Alian, F. Ein-Mozaffari, S.R. Upreti, Analysis of the mixing of solid particles in a plowshare mixer via discrete element method (DEM), *Powder Technology*, 274 (2015) 77-87.
- [53] M. Alian, F. Ein-Mozaffari, S.R. Upreti, J. Wu, Using discrete element method to analyze the mixing of the solid particles in a slant cone mixer, *Chemical Engineering Research and Design*, 93 (2015) 318-329.
- [54] Y. Gao, A. Vanarase, F. Muzzio, M. Ierapetritou, Characterizing continuous powder mixing using residence time distribution, *Chemical Engineering Science*, 66 (2011) 417-425.
- [55] Y. Gao, F.J. Muzzio, M.G. Ierapetritou, Optimizing continuous powder mixing processes using periodic section modeling, *Chemical Engineering Science*, 80 (2012) 70-80.
- [56] M. Sen, R. Ramachandran, A multi-dimensional population balance model approach to continuous powder mixing processes, *Advanced Powder Technology*, 24 (2013) 51-59.
- [57] Y. Gao, F.J. Muzzio, M.G. Ierapetritou, Scale-up strategy for continuous powder blending process, *Powder Technology*, 235 (2013) 55-69.
- [58] J. Wu, Y. Zhu, L. Pullum, Impeller geometry effect on velocity and solids suspension, *Chemical Engineering Research and Design*, 79 (2001) 989-997.
- [59] T. Kumaresan, J.B. Joshi, Effect of impeller design on the flow pattern and mixing in stirred tanks, *Chemical Engineering Journal*, 115 (2006) 173-193.
- [60] T. Jirout, F. Rieger, Impeller design for mixing of suspensions, *Chemical Engineering Research and Design*, 89 (2011) 1144-1151.
- [61] S. Radl, D. Brandl, H. Heimburg, B.J. Glasser, J.G. Khinast, Flow and mixing of granular material over a single blade, *Powder Technology*, 226 (2012) 199-212.
- [62] G.R. Chandratilleke, A.B. Yu, J. Bridgwater, A DEM study of the mixing of particles induced by a flat blade, *Chemical Engineering Science*, 79 (2012) 54-74.
- [63] G.R. Chandratilleke, A.B. Yu, J. Bridgwater, K. Shinohara, A particle-scale index in the quantification of mixing of particles, *AIChE Journal*, 58 (2012) 1099-1118.
- [64] P.C. Knight, J.P.K. Seville, A.B. Wellm, T. Instone, Prediction of impeller torque in high shear powder mixers, *Chemical Engineering Science*, 56 (2001) 4457-4471.

- [65] S. Wu, S.S. Panikar, R. Singh, J. Zhang, B. Glasser, R. Ramachandran, A systematic framework to monitor mulling processes using Near Infrared spectroscopy, *Advanced Powder Technology*, 27 (2016) 1115-1127.
- [66] A. Chaudhury, A. Kapadia, A.V. Prakash, D. Barrasso, R. Ramachandran, An extended cell-average technique for a multi-dimensional population balance of granulation describing aggregation and breakage, *Advanced Powder Technology*, 24 (2013) 962-971.
- [67] M. Ritala, P. Holm, T. Schaefer, H.G. Kristensen, Influence of liquid bonding strength on power consumption during granulation in a high shear mixer, *Drug Development and Industrial Pharmacy*, 14 (1988) 1041-1060.
- [68] M. Ierapetritou, F. Muzzio, G. Reklaitis, Perspectives on the continuous manufacturing of powder-based pharmaceutical processes, *AIChE Journal*, 62 (2016) 1846-1862.
- [69] S.L. Lee, T.F. O'Connor, X. Yang, C.N. Cruz, S. Chatterjee, R.D. Madurawe, C.M.V. Moore, L.X. Yu, J. Woodcock, Modernizing pharmaceutical manufacturing: from batch to continuous production, *Journal of Pharmaceutical Innovation*, 10 (2015) 191-199.
- [70] A.U. Vanarase, F.J. Muzzio, Effect of operating conditions and design parameters in a continuous powder mixer, *Powder Technology*, 208 (2011) 26-36.
- [71] A.U. Vanarase, J.G. Osorio, F.J. Muzzio, Effects of powder flow properties and shear environment on the performance of continuous mixing of pharmaceutical powders, *Powder Technology*, 246 (2013) 63-72.
- [72] A.W. Alexander, B. Chaudhuri, A. Faqih, F.J. Muzzio, C. Davies, M.S. Tomassone, Avalanching flow of cohesive powders, *Powder Technology*, 164 (2006) 13-21.
- [73] D. am Ende, M. Birch, S.J. Brenek, M.T. Maloney, Development and application of laboratory tools to predict particle properties upon scale-up in agitated filter-dryers, *Organic Process Research & Development*, 17 (2013) 1345-1358.
- [74] H.P. Zhu, Z.Y. Zhou, R.Y. Yang, A.B. Yu, Discrete particle simulation of particulate systems: Theoretical developments, *Chemical Engineering Science*, 62 (2007) 3378-3396.
- [75] H.P. Zhu, Z.Y. Zhou, R.Y. Yang, A.B. Yu, Discrete particle simulation of particulate systems: A review of major applications and findings, *Chemical Engineering Science*, 63 (2008) 5728-5770.
- [76] Y. Tsuji, T. Tanaka, T. Ishida, Lagrangian numerical simulation of plug flow of cohesionless particles in a horizontal pipe, *Powder Technology*, 71 (1992) 239-250.

- [77] J. Gyenis, Z. Ulbert, J. Szépvölgyi, Y. Tsuji, Discrete particle simulation of flow regimes in bulk solids mixing and conveying, *Powder Technology*, 104 (1999) 248-257.
- [78] S. Limtrakul, A. Boonsrirat, T. Vatanatham, DEM modeling and simulation of a catalytic gas–solid fluidized bed reactor: a spouted bed as a case study, *Chemical Engineering Science*, 59 (2004) 5225-5231.
- [79] S. Limtrakul, A. Chalermwattanatai, K. Unggurawirote, Y. Tsuji, T. Kawaguchi, W. Tanthapanichakoon, Discrete particle simulation of solids motion in a gas–solid fluidized bed, *Chemical Engineering Science*, 58 (2003) 915-921.
- [80] H. Kruggel-Emden, E. Simsek, S. Rickelt, S. Wirtz, V. Scherer, Review and extension of normal force models for the discrete element method, *Powder Technology*, 171 (2007) 157-173.
- [81] H. Kruggel-Emden, S. Wirtz, V. Scherer, A study on tangential force laws applicable to the discrete element method (DEM) for materials with viscoelastic or plastic behavior, *Chemical Engineering Science*, 63 (2008) 1523-1541.
- [82] R.D. Mindlin, Compliance of elastic bodies in contact, *Journal of Applied Mechanics*, 16 (1949) 259-268.
- [83] G. Lian, C. Thornton, M.J. Adams, A Theoretical Study of the Liquid Bridge Forces between Two Rigid Spherical Bodies, *Journal of Colloid and Interface Science*, 161 (1993) 138-147.
- [84] T. Mikami, H. Kamiya, M. Horio, Numerical simulation of cohesive powder behavior in a fluidized bed, *Chemical Engineering Science*, 53 (1998) 1927-1940.
- [85] C.D. Willett, M.J. Adams, S.A. Johnson, J.P.K. Seville, Capillary bridges between two spherical bodies, *Langmuir*, 16 (2000) 9396-9405.
- [86] S. Herminghaus, Dynamics of wet granular matter, *Advances in Physics*, 54 (2005) 221-261.
- [87] D. Shi, J.J. McCarthy, Numerical simulation of liquid transfer between particles, *Powder Technology*, 184 (2008) 64-75.
- [88] C.S. Campbell, Self-diffusion in granular shear flows, *Journal of Fluid Mechanics*, 348 (1997) 85-101.
- [89] J. Choi, A. Kudrolli, R.R. Rosales, M.Z. Bazant, Diffusion and mixing in gravity-driven dense granular flows, *Physical Review Letters*, 92 (2004) 1743011-1743014.

- [90] B.J. Glasser, I. Goldhirsch, Scale dependence, correlations, and fluctuations of stresses in rapid granular flows, *Physics of Fluids*, 13 (2001) 407-420.
- [91] R.B. Bird, W.E. Stewart, E.N. Lightfoot, *Transport Phenomena*, Revised 2nd ed., John Wiley & Sons, Inc., New York, USA, 2007.
- [92] A. Darelus, E. Lennartsson, A. Rasmuson, I. Niklasson Björn, S. Folestad, Measurement of the velocity field and frictional properties of wet masses in a high shear mixer, *Chemical Engineering Science*, 62 (2007) 2366-2374.
- [93] B. Remy, Granular flow, segregation and agglomeration in bladed mixers, in: *Chemical and Biochemical Engineering*, Rutgers, The State University of New Jersey, New Brunswick, NJ, 2010, pp. 285.
- [94] M. Halidan, G.R. Chandratilleke, S.L.I. Chan, A.B. Yu, J. Bridgwater, Prediction of the mixing behaviour of binary mixtures of particles in a bladed mixer, *Chemical Engineering Science*, 120 (2014) 37-48.
- [95] M. Muthuswamy, A. Tordesillas, How do interparticle contact friction, packing density and degree of polydispersity affect force propagation in particulate assemblies?, *Journal of Statistical Mechanics: Theory and Experiment*, 09 (2006) 1-23.
- [96] V. Boonkanokwong, B. Remy, J.G. Khinast, B.J. Glasser, The effect of the number of impeller blades on granular flow in a bladed mixer, *Powder Technology*, 302 (2016) 333-349.
- [97] B.J.S. Benque, DEM simulation of dry and wet granular material in a four-bladed mixer, in: *Chemical and Process Engineering*, Institute for Process and Particle Engineering, Graz University of Technology, Graz, Austria, 2016, pp. 51.
- [98] P. Jop, Y. Forterre, O. Pouliquen, A constitutive law for dense granular flows, *Nature*, 441 (2006) 727-730.
- [99] B. Andreotti, O. Pouliquen, Y. Forterre, The granular liquid, in: B. Andreotti, O. Pouliquen, Y. Forterre (Eds.) *Granular Media: Between Fluid and Solid*, Cambridge University Press, Cambridge, 2013, pp. 215-284.
- [100] T. Barczy, T. Travnickova, J. Havlica, M. Kohout, Effect of bed depth on granular flow and homogenization in a vertical bladed mixer via discrete element method, *Chemical Engineering & Technology*, 38 (2015) 1195-1202.
- [101] J.J. McCarthy, Micro-modeling of cohesive mixing processes, *Powder Technology*, 138 (2003) 63-67.